Autonomous, Decentralised Green Ammonia Production

A techno-economic analysis

H.P.B. Hartman



Delft University of Technology

Autonomous, Decentralised Green Ammonia Production

A techno-economic analysis

by

Hidde Hartman

Student number: 5078008

to obtain the degree of Master of Science at the Delft University of Technology, to be defended publicly on Friday November 27, 2026 at 14:00.

Thesis Committee

Chair: Prof.dr.ir. O. Isabella
Supervisor: Dr. M. Rana
External Member: Dr.ir. A. Vasileiadis

Company Supervisors (Shell)

Dr. A. Higler
Dr. E. Unsal

Project Duration: April, 2026 – November, 2026
Faculty of Electrical Engineering, Mathematics and Computer Science (EEMCS)
Delft University of Technology

An electronic version of this thesis is available at `http://repository.tudelft.nl/`.

Style: TU Delft Report Style
Cover: Dawn Over Green Ammonia Fields (AI)

TU Delft

Preface

My graduation research at Shell marks the final step in my Master's degree in Sustainable Energy Technology at Delft University of Technology. It also marks the end of my academic journey in Delft, a period I look back on with many great memories, valuable experiences and friendships.

When I first started studying in Delft, I did not yet know exactly which direction I wanted to take. What attracted me to engineering was the opportunity to understand how things work and to use that knowledge to solve real-world problems. Throughout my studies, I became increasingly interested in energy systems and the technologies needed to make the energy transition possible. I was particularly drawn to the technical challenges of integrating renewable energy sources, developing efficient energy conversion processes and designing systems that can operate reliably under changing conditions. At the same time, I realised that technical performance alone is not enough. For sustainable technologies to make a meaningful contribution to the energy transition, they must also be economically viable. This combination of technical challenges and practical considerations ultimately led me to pursue a Master's degree in Sustainable Energy Technology.

Completing my studies with a graduation project at Shell's Energy Transition Campus in Amsterdam has been a particularly valuable experience. My research focused on the techno-economic feasibility of decentralised green ammonia production, combining renewable energy systems, chemical processes and economic analysis. The project gave me the opportunity to apply much of what I had learned during my studies while also exploring a field that was largely new to me. It has been especially interesting to see how technical choices, local conditions and economic considerations are closely connected, and how a technology that appears promising in theory can face substantial challenges in practice.

This thesis would not have been possible without the support of several people. First, I would like to thank Moumita Rana for her guidance, valuable feedback and encouragement throughout the research. Our monthly meetings helped me maintain a clear direction and critically reflect on my work, while also giving me the freedom to develop my own ideas. I would also like to express my gratitude to Arnoud Higler for his technical insights, critical questions and the many discussions that helped shape this thesis. I particularly appreciated your willingness to think along with me and challenge my assumptions throughout the project.

I would also like to thank Evren Unsal for creating such a welcoming and inspiring working environment at Shell. Being surrounded by students and professionals from different backgrounds and countries made the experience both interesting and enjoyable. Beyond the research itself, I really enjoyed the conversations, shared experiences, many laughs and the good atmosphere throughout these months. It made coming to the office something I genuinely looked forward to.

Finally, I would like to thank my friends and family for making my years in Delft so enjoyable. My time here would not have been the same without the friendships, memories and experiences we have shared. My time here would not have been the same without the friendships, memories and experiences we have shared.

I hope this thesis contributes to a better understanding of the technical and economic feasibility of decentralised green ammonia production and provides valuable insights into its potential role in the energy transition.

H.P.B. Hartman
Delft, November 2026

Abstract

Ammonia is essential for global food production and is increasingly considered as an energy carrier, but it is mostly made from fossil fuels in large, centralised plants. Small plants powered by local wind and solar electricity could offer an alternative in regions with strong renewable resources but limited access to the grid or existing supply chains. This thesis examines the techno-economic feasibility of a decentralised autonomous ammonia plant and tests whether electrochemical nitrogen reduction (NRR) could offer an alternative production route.

A multi-criteria technology selection and a plant-level energy and mass balance define an off-grid plant built from commercial components around a Haber–Bosch synthesis loop, contracted to deliver 25 t of ammonia every month. An hourly simulation of plant operation is combined with an optimisation of generation, storage and conversion capacities for the lowest levelised cost of ammonia (LCOA) at Geraldton, Neom and Lüderitz. Each design is sized on fifteen historical weather years, validated on ten further years and are benchmarked against reported ammonia price ranges across global markets. Monte Carlo simulations and alternative cost bases assess the cost uncertainty. Reduced-order models of aqueous, lithium-mediated and water-fed membrane NRR are compared with the resulting electrolyser–Haber–Bosch plant at their most energy-efficient operating points.

The least-cost design at Geraldton combines solar PV and wind with a small battery, a small hydrogen buffer and an 18 t ammonia tank, and reaches an LCOA of $864/t, compared with $2,775/t for a solar-only base case. The design meets the contract in 22 of 25 historical years, but its small production margin makes reliability sensitive to modest output losses. Under cost uncertainty, the median LCOA is $906/t, and shipping to likely markets adds at least $47–56/t, placing the delivered cost above the $750–900/t range of recent green-ammonia tenders. Alternative component prices shift the result between $588 and $1,127/t, so the plant competes with current green-ammonia prices only under favourable cost assumptions.

None of the NRR routes matches the reference. They require about 9 to 27 times more electricity per kilogram of ammonia, at productive current densities two to five orders of magnitude lower. Aqueous cells are limited by competing hydrogen evolution, and lithium-mediated routes by the approximately 3.4 V needed to plate lithium.

The findings demonstrate that an autonomous plant can supply ammonia reliably in most weather years, but that its economic viability is marginal and depends stronglt on cost assumptions. Its advantage is most likely where local production avoids transporting ammonia to remote users, which requires a site-specific comparison with delivered ammonia. NRR is not yet a viable alternative and needs major advances in selectivity, current density and cell voltage before it can compete.

Nomenclature

Abbreviations

Abbreviation	Definition
ASR	Area-specific resistance
AWE	Alkaline water electrolysis
AWH	Atmospheric water harvesting
BEP	Brønsted–Evans–Polanyi relation
CAPEX	Capital expenditure
CAGR	Compound annual growth rate
CF	Capacity factor
CRF	Capital recovery factor
FE	Faradaic efficiency
FESM	Future Energy System Modelling (Shell)
HB	Haber–Bosch
HER	Hydrogen evolution reaction
HHV	Higher heating value
HOR	Hydrogen oxidation reaction
LCOA	Levelised cost of ammonia
LCOE	Levelised cost of electricity
LFP	Lithium iron phosphate
LHV	Lower heating value
MCDA	Multi-criteria decision analysis
MPC	Model predictive control
MTBM	Mean time between maintenance
MUSD	Million US dollars
NRR	Nitrogen reduction reaction (electrochemical)
O&M	Operation and maintenance
OER	Oxygen evolution reaction
OPEX	Operating expenditure
PEM	Proton exchange membrane
PERT	Program evaluation and review technique (beta-PERT distribution)
PI	Proportional–integral (control)
PSA	Pressure swing adsorption
PV	Photovoltaic
RHE	Reversible hydrogen electrode
SAW	Simple additive weighting
SEC	Specific energy consumption
SEI	Solid electrolyte interphase
SHE	Standard hydrogen electrode
SMR	Steam methane reforming
SOEC	Solid oxide electrolysis cell
SWRO	Seawater reverse osmosis
TRL	Technology readiness level
WACC	Weighted average cost of capital
WSM	Weighted-sum model

Symbols

Subscripts distinguish components, reactions, and scenarios.

Symbol	Definition	Unit
Technology selection		
S_i	MCDA score or installed capacity (by context)	– / varies
s_{ij}	Score of technology i on criterion j	–
w_j	Weight assigned to criterion j	–
Plant modelling and energy		
A	PV field or electrode area	m^2
CF	Solar or wind capacity factor	–
$G_{\max}$	Reference solar irradiance	$\mathrm{W\,m^{-2}}$
P	Electrical power (generation or demand)	kW
$m_{\mathrm{NH_3}}$	Ammonia production or delivery quantity	kg or t
$\dot{m}$	Mass flow rate	$\mathrm{kg\,s^{-1}}$
SEC	Specific electricity consumption	$\mathrm{kWh\,kg_{NH_3}^{-1}}$
η	Energy or conversion efficiency	–
HHV, LHV	Higher and lower heating values	$\mathrm{MJ\,kg^{-1}}$
Costs and uncertainty		
CAPEX_i	Capital expenditure of component i	USD
c_i	Unit installed capital cost	USD / capacity unit
C	Annualised system cost	$\mathrm{USD\,yr^{-1}}$
CRF	Capital recovery factor	$\mathrm{yr^{-1}}$
f_{opex}	Annual fixed operating-cost fraction	$\mathrm{yr^{-1}}$
n_i	Technical lifetime of component i	yr
r	Discount rate	–
LCOA	Levelised cost of ammonia	$\mathrm{USD\,t_{NH_3}^{-1}}$
LCOE	Levelised electricity cost	$\mathrm{USD\,MWh^{-1}}$
$\alpha,\ \beta$	Beta-PERT distribution shape parameters	–
ρ	Assumed correlation between uncertain costs	–
Electrochemical NRR modelling		
ASR	Area-specific electrical resistance	$\mathrm{\Omega\,cm^2}$
b	Tafel slope of the relevant electrode reaction	$\mathrm{V\,dec^{-1}}$
$C_{\mathrm{N_2},b}$	Bulk dissolved nitrogen concentration	$\mathrm{mol\,cm^{-3}}$
$D_{\mathrm{N_2}}$	Nitrogen diffusion coefficient	$\mathrm{cm^2\,s^{-1}}$
E	Electrode potential	V vs RHE
F	Faraday constant	$\mathrm{C\,mol^{-1}}$
FE	Faradaic efficiency of the indicated product	–
I	Electric current	A
j	Applied, partial or productive current density	$\mathrm{A\,cm^{-2}}$
$M_{\mathrm{NH_3}}$	Molar mass of ammonia	$\mathrm{kg\,mol^{-1}}$
$\dot{n}$	Molar production rate	$\mathrm{mol\,s^{-1}}$
V_{cell}	Full electrochemical cell voltage	V
$\Delta V_{\mathrm{plate}}$	Lithium-plating voltage contribution	V
$\eta_a,\ \eta_{\mathrm{mem}}$	Anodic and membrane voltage losses	V
δ	Nitrogen diffusion boundary-layer thickness	cm
Thermodynamics and gas processing		
c_p	Molar heat capacity	$\mathrm{J\,mol^{-1}\,K^{-1}}$
$\Delta G^0_{\mathrm{rxn}}$	Standard Gibbs free energy change	$\mathrm{J\,mol^{-1}}$
ΔH^0_{r}	Standard reaction enthalpy change	$\mathrm{J\,mol^{-1}}$
p	Gas or operating pressure	bar
$\dot{Q}$	Heat flow or duty	kW
R	Universal gas constant	$\mathrm{J\,mol^{-1}\,K^{-1}}$
T	Temperature	K
γ	Gas heat-capacity ratio	–
η_{is}	Compressor isentropic efficiency	–

Contents

Preface i

Abstract ii

Nomenclature iii

1 Introduction 1
- 1.1 Ammonia and its relevance . . . 1
- 1.2 Development of ammonia production . . . 2
- 1.3 Green ammonia pathways . . . 2
  - 1.3.1 Haber–Bosch with electrolytic hydrogen . . . 2
  - 1.3.2 Absorption-enhanced Haber–Bosch . . . 3
  - 1.3.3 Electrochemical nitrogen reduction . . . 3
  - 1.3.4 Plasma-based nitrogen fixation . . . 5
  - 1.3.5 Nitrogen supply . . . 5
  - 1.3.6 Water supply . . . 5
- 1.4 Autonomy and process control . . . 6
  - 1.4.1 Defining autonomy . . . 6
  - 1.4.2 Control under variable renewable supply . . . 6
  - 1.4.3 Safety, fault management and maintenance . . . 7
  - 1.4.4 Benefits of autonomy . . . 7
- 1.5 Decentralisation . . . 7
  - 1.5.1 Feedstock self-sufficiency . . . 7
  - 1.5.2 Location and modular deployment . . . 7
  - 1.5.3 Remote-operation requirements . . . 8
- 1.6 Plant scale . . . 8
  - 1.6.1 Economies of scale in conventional ammonia production . . . 8
  - 1.6.2 Modularity in renewable-powered production . . . 8
  - 1.6.3 Relevance for this thesis . . . 9
- 1.7 Levelised cost of ammonia . . . 9
- 1.8 Research gap and research questions . . . 9
- 1.9 Thesis outline . . . 10

2 Methodology 11
- 2.1 Multi Criteria Decision Analysis . . . 11
  - 2.1.1 Criteria . . . 12
- 2.2 Plant-Level Energy and Mass Balance . . . 13
- 2.3 Future Energy System Modelling . . . 14
  - 2.3.1 FESM framework . . . 14
  - 2.3.2 Application in this thesis . . . 15
- 2.4 Modelling . . . 15
  - 2.4.1 Base-case model . . . 15
  - 2.4.2 Cost Modelling . . . 19
  - 2.4.3 Configuration optimisation . . . 20
  - 2.4.4 Probabilistic LCOA . . . 21
- 2.5 Autonomy analysis . . . 22
- 2.6 Reduced-order electrochemical NRR modelling . . . 22
  - 2.6.1 Aqueous NRR performance model . . . 22
  - 2.6.2 Li-mediated NRR: a current-driven model . . . 25
  - 2.6.3 Water-fed membrane Li-mediated NRR . . . 27
- 2.7 Comparison framework NRR with Electrolyzer + HB . . . 28

2.7.1 Cell-level comparison . . . 28
2.7.2 Analysis of the performance gap . . . 30
2.7.3 Selection of the cell route . . . 30
2.7.4 Configuration and assessment of the selected route . . . 31
2.8 Sensitivity and uncertainty analysis . . . 31

3 Results **33**
3.1 MCDA results . . . 33
3.1.1 Power supply . . . 33
3.1.2 Battery storage . . . 34
3.1.3 Nitrogen supply . . . 35
3.1.4 Water supply . . . 36
3.1.5 Electrolyser selection . . . 36
3.1.6 Resulting base-case plant . . . 37
3.2 Plant-level Energy and Mass Balance . . . 38
3.2.1 Overview system flow . . . 38
3.2.2 Mass balance . . . 38
3.2.3 Specific energy consumption . . . 39
3.2.4 Exergy . . . 39
3.2.5 Limitations . . . 40
3.3 FESM Simulation Results . . . 40
3.4 Base Case . . . 43
3.4.1 Energy accounting and sizing . . . 45
3.5 Optimised Plant Configurations . . . 46
3.5.1 Search . . . 46
3.5.2 Optimised configuration and performance . . . 47
3.5.3 Operating behaviour and energy flows . . . 48
3.5.4 Cost breakdown . . . 52
3.5.5 Value of wind and ammonia storage . . . 54
3.5.6 Cost sensitivity and probabilistic LCOA . . . 55
3.5.7 Sensitivity around the optimum . . . 57
3.5.8 Location sensitivity . . . 58
3.5.9 Competitiveness . . . 60
3.6 Autonomy of the optimised plant . . . 60
3.7 Electrochemical NRR results . . . 62
3.7.1 Cell performance . . . 62
3.7.2 Energy parity . . . 64
3.7.3 Productive current density and electrode area . . . 66
3.7.4 Potential for Performance Improvement . . . 67
3.7.5 Route selection and hybrid configuration . . . 70

4 Discussion **72**
4.1 Technical feasibility: plant sizing, location and robustness . . . 72
4.2 Economic feasibility: cost assumptions, scale and use case . . . 73
4.3 Implications for electrochemical NRR . . . 74
4.4 Model scope and limitations . . . 75

5 Conclusion **76**
5.1 Autonomous renewable ammonia plant . . . 76
5.2 Electrochemical nitrogen reduction . . . 77

6 Recommendations **79**
6.1 A remote-demand use case . . . 79
6.2 Validating subsystem operating assumptions . . . 80
6.3 Cost basis . . . 80
6.4 Weather Variability and Model Scope . . . 80
6.5 Nitrogen reduction and other synthesis routes . . . 81
6.6 Concluding recommendation . . . 81

7 Use of AI **82**

References **83**

A Extended results **89**
A.1 Mass Balance . . . 89
A.2 FESM benchmark . . . 90
A.2.1 Configuration . . . 90
A.2.2 Energy balance . . . 91
A.2.3 Cost . . . 91
A.3 Configuration optimisation . . . 92
A.3.1 Cost assumptions . . . 92
A.3.2 Search statistics . . . 92
A.3.3 Levelised and capital cost by component . . . 93
A.3.4 Location results in detail . . . 94
A.3.5 Weather-robust optimisation . . . 96
A.4 Final design . . . 97
A.5 Sensitivity analysis . . . 99
A.5.1 Cost assumptions . . . 99
A.5.2 Monte Carlo input ranges . . . 100
A.5.3 Design variables about the optimum . . . 101
A.6 Ammonia shipping cost . . . 102

B Supporting visual material **103**
B.1 Extended system balance . . . 104

C Model pseudocode **107**
C.1 Base-case plant simulation — Pseudo-code . . . 107
C.2 Robust configuration optimiser — Pseudo-code . . . 108
C.3 Aqueous NRR model — Pseudo-code . . . 109
C.4 Li-mediated NRR model — Pseudo-code . . . 109
C.5 Water-fed membrane NRR model — Pseudo-code . . . 110

1 Introduction

Ammonia is essential for global food production and is increasingly considered as an energy carrier, but it is still produced mostly from fossil fuels in large, centralised plants. Growing demand for renewable solutions, combined with rising gas prices and geopolitical uncertainty, has accelerated the search for alternative production pathways. In remote areas with abundant renewable resources but limited grid access, decentralised green ammonia production could reduce dependence on fossil-based supply chains. This thesis therefore investigates the feasibility of an autonomous green ammonia plant powered by renewable energy sources.

Such a plant departs from conventional ammonia production in several ways. Conventional plants are large, operate continuously and are supported by on-site personnel. The plant considered here must instead integrate renewable electricity generation, water and nitrogen supply, hydrogen production and ammonia synthesis into one autonomous system that operates under variable solar and wind conditions. Sections 1.1 to 1.7 therefore introduce the relevance of ammonia, the technologies underlying its production and the main constraints that define this system. Section 1.8 then identifies the research gap and presents the research questions and scope, and Section 1.9 outlines the approach and the structure of this thesis.

1.1. Ammonia and its relevance

Ammonia (NH_3) is one of the most important industrial chemicals globally. Around 70% of ammonia demand is linked to agriculture, where it is used as a key feedstock for nitrogen-based fertilisers such as urea, ammonium nitrate and ammonium sulfate [87]. Synthetic nitrogen fertilisers have played a central role in increasing global crop yields and are estimated to support food production for roughly half of the world's population [18]. Demand is expected to continue growing, with the global ammonia market projected to expand at a compound annual growth rate of approximately 5% between 2025 and 2035 [87].

Beyond agriculture, ammonia has attracted attention as an energy carrier. Its physical properties make it considerably more practical to store and transport than hydrogen: it liquefies at $-33\ ^\circ\mathrm{C}$ under atmospheric pressure rather than the $-253\ ^\circ\mathrm{C}$ required for liquid hydrogen, and carries a substantially higher volumetric energy density [42]. These properties position ammonia as a viable medium for transporting renewable energy over long distances, without the infrastructure constraints that limit direct hydrogen logistics. Ammonia is also being considered as a direct low-carbon fuel, particularly in the maritime sector, where it could supply roughly 44% of international shipping's final energy demand by 2050 [37]. More broadly, a potential global ammonia market of 688 million tonnes per year is projected for 2050 in a 1.5 $^\circ\mathrm{C}$-aligned scenario, compared with approximately 183 million tonnes in 2020 [42].

The urgency of decarbonising ammonia production is substantial. Conventional production relies overwhelmingly on fossil fuels, with around 72% of production based on natural gas and 22% on coal, and generates approximately 1.3% of global CO_2 emissions [42, 36]. Despite growing policy interest, renewable ammonia production remains limited. In 2025, operational renewable ammonia plants had a combined annual production capacity of approximately 0.625 Mt, equivalent to around 0.3% of global annual ammonia production [69]. This gap between the importance of ammonia and the limited

production of green ammonia shows the need for more sustainable production methods.

1.2. Development of ammonia production

The Haber–Bosch process, developed by Fritz Haber and industrialised by Carl Bosch in the early twentieth century, enabled the large-scale synthesis of ammonia from atmospheric nitrogen and hydrogen [79]. The process is based on the exothermic reaction:

$$\mathrm{N_2} + 3\mathrm{H_2} \rightleftharpoons 2\mathrm{NH_3} \qquad \Delta H^\circ = -92\ \mathrm{kJ\,mol^{-1}_{N_2}} \quad (-46\ \mathrm{kJ\,mol^{-1}_{NH_3}})$$

Ammonia synthesis is typically carried out over an iron catalyst at pressures of 150–300 bar and temperatures of 350–500 $^\circ\mathrm{C}$ [42]. High pressure favours ammonia formation, while elevated temperature is required to achieve a practical reaction rate. Because the single-pass conversion is limited, unreacted nitrogen and hydrogen are recycled and ammonia is continuously removed from the synthesis loop [4].

In conventional ammonia production, hydrogen is primarily obtained through steam methane reforming (SMR), in which natural gas and steam are converted into a hydrogen-rich synthesis gas. After water–gas shift and CO_2 removal, the purified hydrogen is fed into the Haber–Bosch loop. This conventional SMR–Haber–Bosch route remains dominant because of its maturity, reliability and economies of scale, with an energy consumption of approximately 28–33 GJ per tonne of ammonia [42]. As a result, ammonia production accounts for approximately 2% of global final energy consumption. SMR alone generates approximately 1.22 t CO_2 per tonne of ammonia, excluding additional emissions from fuel combustion, natural-gas extraction and upstream losses [43].

The main opportunity for decarbonisation is therefore the replacement of fossil-derived hydrogen with green hydrogen produced by renewable-powered water electrolysis. This retains the mature Haber–Bosch synthesis loop while substantially reducing process emissions, forming the basis of the green ammonia pathway discussed in Section 1.3.

1.3. Green ammonia pathways

Green ammonia can be produced through several different routes. Renewable-powered Haber–Bosch retains the conventional synthesis loop but replaces fossil-derived hydrogen with green hydrogen. Absorption-enhanced Haber–Bosch modifies the synthesis loop, while electrochemical nitrogen reduction and plasma fixation use alternative synthesis processes. These routes are discussed in that order below, followed by the nitrogen and water supply technologies relevant to their operation.

1.3.1. Haber--Bosch with electrolytic hydrogen

The green Haber–Bosch pathway retains the conventional ammonia synthesis loop but replaces fossil-derived hydrogen from steam methane reforming or coal gasification with hydrogen produced through water electrolysis using renewable electricity. The main technological distinction therefore lies in the production of hydrogen. Three principal electrolysis technologies are considered for renewable hydrogen production.

Alkaline water electrolysis (AWE) uses a liquid 20–30% KOH electrolyte circulating between nickel-based electrodes separated by a diaphragm [34]. It is the most mature electrolysis technology, with commercial lifetimes of around 60,000 h and system energy consumption of approximately 52 kWh $\mathrm{kg^{-1}_{H_2}}$ [71]. Its main disadvantages for off-grid operation are its limited low-load flexibility and the increased risk of gas crossover at low current densities, which can restrict operation under intermittent renewable power supply [30].

Proton exchange membrane (PEM) electrolysis uses a solid polymer electrolyte membrane instead of a circulating liquid electrolyte and typically relies on platinum-group metal catalysts. PEM systems are commercially mature and have system energy consumption values of approximately 53 kWh $\mathrm{kg^{-1}_{H_2}}$, which is comparable to alkaline electrolysis [71]. A key advantage for intermittent renewable operation is its high operational flexibility, including a wide dynamic operating range, fast start-up behaviour and strong part-load capability [11]. The main trade-off is higher CAPEX, mainly due to the use of platinum-group metal catalysts [8]. In addition, dynamic operation under intermittent power supply can increase degradation [17].

Solid oxide electrolysis (SOEC) operates at high temperature, typically around 600–850 $^{\circ}\mathrm{C}$, using a ceramic electrolyte that conducts oxide ions or protons. When part of the required energy is supplied as heat, SOEC can achieve a lower electrical energy demand than alkaline and PEM electrolysis [24]. However, the technology is less mature, with recent demonstration projects generally classified around TRL 7 depending on the application [24]. Its high operating temperature also creates challenges for autonomous off-grid operation, as dynamic loading and frequent start-stop cycles can cause thermal stress and accelerate degradation [33]. Consequently, SOEC requires careful thermal management when coupled to intermittent renewable generation.

1.3.2. Absorption-enhanced Haber--Bosch

Absorption-enhanced Haber–Bosch is a modified synthesis-loop configuration in which ammonia is continuously removed using a solid sorbent integrated with the catalyst bed. This shifts the equilibrium towards ammonia formation and enables higher single-pass conversion at lower pressure [65]. Reported conversions of approximately 80% at around 20 bar, compared with roughly 15% for conventional operation, may reduce compression requirements and improve the suitability of Haber–Bosch for small-scale plants [52]. Its main remaining limitation is the long-term stability of the sorbent over repeated adsorption–regeneration cycles.

1.3.3. Electrochemical nitrogen reduction

Electrochemical nitrogen reduction reaction (NRR) routes aim to produce ammonia directly from nitrogen using electrons and a proton source in an electrochemical cell, thereby bypassing the Haber–Bosch synthesis loop. When water acts as the proton source and oxygen evolution occurs at the anode, the ideal overall reaction can be written as $\mathrm{N_2 + 3H_2O \rightarrow 2NH_3 + 1.5O_2}$, with a thermodynamic minimum cell voltage of only about 1.17 V, comparable to water splitting (1.23 V). However, the proton source, electrolyte and anodic reaction depend on the specific NRR route. The concept is attractive because some NRR pathways may enable ammonia production under mild operating conditions without a separate hydrogen-production and Haber–Bosch synthesis step [95].

NRR performance is mainly characterised by cell voltage, Faradaic efficiency and current density. Cell voltage governs the electrical energy input, while Faradaic efficiency indicates the fraction of current used for ammonia formation rather than competing reactions such as hydrogen evolution. Current density determines the production rate per electrode area and therefore affects the required cell size. Together, these interdependent parameters determine the specific energy consumption and ammonia production capacity of an NRR system.

NRR route types

Several NRR routes are discussed in the literature, but this thesis focuses on the most relevant concepts: aqueous NRR, lithium-mediated NRR, and membrane-separated water-fed lithium-mediated NRR. They differ mainly in the proton source, electrolyte environment and anodic reaction.

Aqueous NRR: Nitrogen is reduced directly at the cathode in a water-based electrolyte, with protons or proton equivalents supplied by the aqueous electrolyte reacting with electrons to form ammonia, as illustrated in Figure 1.1. It is the simplest route in principle, requiring no mediator or organic solvent. However, hydrogen evolution occurs within a similar potential range and generally has more favourable kinetics than nitrogen reduction, as NRR requires activation of the stable N≡N bond. Consequently, a large fraction of the supplied current is often directed toward hydrogen formation rather than ammonia production. Some studies nevertheless report Faradaic efficiencies of around 10–20%, although these values should be treated with caution because reliable ammonia verification remains a major concern [3].

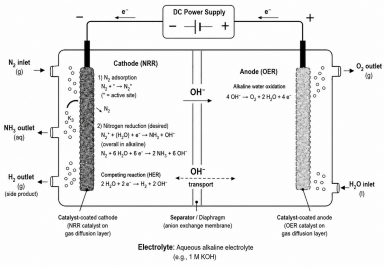

Figure 1.1: Aqueous NRR cell.

Lithium-mediated NRR: Lithium is first electrodeposited at the cathode and reacts with nitrogen to form lithium nitride or related lithium–nitrogen intermediates. These species are subsequently protonated to release ammonia, while the resulting lithium species are returned to the electrochemical cycle, as shown schematically in Figure 1.2. Unlike aqueous NRR, water cannot directly supply the protons because it reacts with and deactivates plated lithium, so a separate proton donor is required, which must itself be supplied upstream and therefore adds an additional material and energy requirement. This indirect route avoids part of the selectivity problem of aqueous NRR and is currently the most experimentally established pathway, with Faradaic efficiencies over 50% reported under optimised conditions. However, these results are achieved at relatively high cell voltages and low production rates [16]. As a result, energy efficiency, scale-up and long-term operation remain the key challenges.

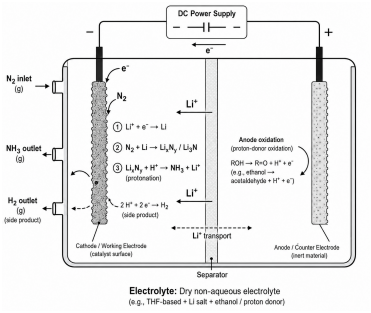

Figure 1.2: Li-mediated NRR cell.

Membrane-separated water-fed NRR: The newest variant adapts lithium-mediated NRR so that water can serve as the proton source. A membrane physically separates the aqueous anode, where water is oxidised, from the dry non-aqueous catholyte, where lithium plating and nitrogen reduction occur, as illustrated in Figure 1.3. This shields lithium from direct water contact, which would otherwise deactivate it. The approach removes the need for a sacrificial proton donor and reduces the feedstock to nitrogen, water and electricity. A Faradaic efficiency of approximately 48% has been demonstrated, but only at high cell voltage, low current density and limited operating duration, leaving energy efficiency, scale-up, durability and sustained production rates still to be proven [97].

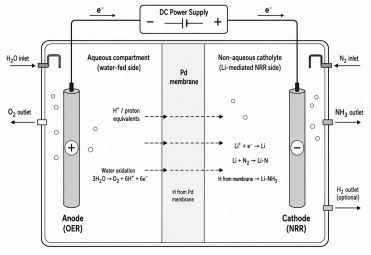

Figure 1.3: Membrane-separated water-fed Li-mediated NRR cell.

Limitations of NRR

Although NRR is attractive because it could produce ammonia directly under mild conditions, none of the discussed routes is currently mature enough to compete directly with electrified Haber–Bosch. Aqueous NRR remains limited by competing hydrogen evolution, low ammonia production rates and uncertainty around reliable ammonia verification. Increasing the cathodic overpotential does not necessarily increase the ammonia production rate continuously. At more negative potentials, hydrogen adsorption can become increasingly favourable and occupy catalytic sites that would otherwise adsorb nitrogen. This reduces both nitrogen surface coverage and ammonia production, creating a relatively narrow operating-potential window for aqueous NRR [14]. Catalyst screening is therefore unlikely to resolve the selectivity problem. Through the Brønsted–Evans–Polanyi (BEP) relation and scaling relations between adsorbates, activity depends on a single binding-energy descriptor, producing a volcano-shaped trend with an optimum binding strength. For NRR, the binding energies of nitrogen intermediates scale with one another, and on most transition metals hydrogen binds more strongly than nitrogen [78]. Together with the fast competing hydrogen evolution reaction and the low solubility of nitrogen in water, these limitations make it difficult to develop catalysts that achieve high selectivity towards ammonia in aqueous NRR [58]. Li-mediated NRR avoids this competition because N_2 is activated by plated lithium rather than at a surface site accessible to hydrogen. However, lithium plating requires highly negative potentials, resulting in a substantial voltage penalty and reduced energy efficiency. The membrane-separated water-fed variant improves the feedstock concept by using water as proton donor, but remains early-stage and still faces high cell voltage, low current density and membrane durability challenges.

Table 1.1 summarises the main bottlenecks of each route, their plant-level impact, and possible mitigation strategies for improving future NRR performance.

Route	Main bottleneck	Impact	Mitigation
Aqueous NRR	• Competing HER • Low N_2 solubility in water • HER-induced active-site blocking (BEP/scaling-limited) • Unreliable NH_3 verification	• Low Faradaic efficiency • Low production rate • Weak basis for plant-scale design	• HER-suppressing catalysts • Gas-diffusion electrodes for N_2 supply • Active sites that break N/H scaling • Feedstock purification
Li-mediated NRR	• Li plating • Dry, O_2-free electrolyte needed • Sacrificial proton donor required	• High cell voltage • Lithium/current inefficiency • Upstream feedstock dependency	• Low-potential mediator • SEI and electrolyte engineering • Gas-diffusion electrodes
Water-fed Li-mediated NRR	• Li plating • Separating water from plated Li • Membrane instability	• High voltage • Low current density • Limited durability and practical operation	• Lower-potential mediator • Thin, stable and N_2-permeable SEI • Water-selective membrane

Table 1.1: Summary of NRR route limitations and possible mitigation strategies.

The implications of these limitations for energy consumption and competitiveness are evaluated in Section 3.7, where the required NRR performance is compared with the green Haber–Bosch benchmark.

1.3.4. Plasma-based nitrogen fixation

Plasma-based nitrogen fixation uses electrical discharges to activate nitrogen and can respond rapidly to variable renewable power. Two main routes were considered: direct plasma synthesis of ammonia from nitrogen and hydrogen, and plasma-assisted formation of $\mathrm{NO_x}$ followed by further conversion to fertiliser products [70, 13]. However, both routes still face several limitations, including low energy efficiency, limited reactor durability and the formation of unwanted by-products. Direct ammonia synthesis is further limited by ammonia decomposition within the plasma zone. As their reported performance remains well below electrified Haber–Bosch and the NRR pathways considered in this thesis, plasma-based synthesis is not investigated further.

1.3.5. Nitrogen supply

Regardless of the synthesis route, all green ammonia production requires nitrogen and water as primary feedstocks. Both can be sourced entirely on-site, which is a key enabler of fully off-grid operation. Nitrogen is separated from air via three main approaches:

- **Cryogenic distillation:** Air is compressed, liquefied and separated by fractional distillation based on the different boiling points of nitrogen, oxygen and argon. It provides high-purity nitrogen at large flow rates but is generally only economical at large scale due to its high capital cost [32].
- **Pressure swing adsorption (PSA):** Compressed air is passed through molecular sieves that selectively adsorb oxygen. The adsorbent is regenerated by depressurisation, allowing continuous nitrogen production. PSA is commonly applied at smaller production scales due to its relatively low capital cost, rapid start-up and operational flexibility [32].
- **Membrane separation:** Compressed air is fed to hollow-fibre polymeric membranes across which oxygen and water vapour permeate faster than nitrogen, leaving an enriched nitrogen retentate. The technology is compact, has no moving parts and follows load changes almost instantaneously, but purity is typically limited to 95–$99.5\,\%$ and the specific energy rises steeply as purity increases [32].

1.3.6. Water supply

Water provides the hydrogen for electrolysis, requiring approximately 9 kg per kg of H_2, equivalent to about 1.6 t per tonne of NH_3. Practical demand is slightly higher due to purification and auxiliary requirements [42]. The feedwater must be treated to electrolyser specifications, typically including deionisation and, where required, reverse osmosis. Three supply routes are considered:

- **Piped supply:** Freshwater from an existing network or local source. This has the lowest energy and infrastructure requirements, but introduces dependence on external infrastructure and water availability.

- **Seawater reverse osmosis (SWRO):** A mature option for coastal sites, with modern systems typically consuming around $3\,\mathrm{kW\,h/m^3}$–$4\,\mathrm{kW\,h/m^3}$. Its energy demand is small relative to ammonia production, although seawater access and brine management are required [93].
- **Atmospheric water harvesting (AWH):** Water is recovered directly from ambient air by condensation or sorption. AWH is modular and independent of liquid-water sources, but generally has a substantially higher energy demand and is dependent on ambient humidity [89].

The suitability of these routes for the autonomous plant is assessed further in Chapter 3.

1.4. Autonomy and process control

Autonomy combines three requirements: a control structure that keeps the plant at a useful operating point, fault handling that keeps it safe with no operator present, and a maintenance interval long enough that absence is the normal condition. Decentralisation and physical self-sufficiency are related but separate, and are addressed in Section 1.5.

1.4.1. Defining autonomy

There is no universally adopted standard for classifying autonomy in the process industries, although several frameworks have been proposed. In this context, autonomy is generally understood as the ability of a system to monitor its condition, make operational decisions and adapt its behaviour with limited human intervention [27]. This goes beyond conventional automation, in which controllers follow predefined setpoints and operating sequences. An autonomous plant must also respond to changing disturbances, operating objectives and equipment conditions while remaining within specified operational and safety constraints [9].

Full autonomy does not necessarily imply the complete removal of human involvement. Remote supervision, periodic maintenance and human intervention during exceptional situations may still be required. For this thesis, autonomy is therefore defined as the ability of the plant to perform routine operation with minimal on-site intervention. This includes monitoring plant states, allocating available energy, adjusting production rates, managing operating-state transitions and initiating a controlled shutdown when operating limits are exceeded.

Conventional regulatory control maintains variables such as temperature, pressure and flow rate around specified setpoints. However, keeping a process stable does not necessarily keep it close to its economically optimal operating point. Self-optimising control addresses this distinction by selecting controlled variables whose regulation keeps economic losses small despite changes in operating conditions and external disturbances [45]. This concept is relevant to an off-grid ammonia plant because the economically preferred operating point can change continuously with renewable electricity availability, storage inventories and feedstock supply.

1.4.2. Control under variable renewable supply

An autonomous off-grid plant requires a layered control structure. Local controllers regulate individual process variables, while a supervisory controller coordinates production, energy allocation and storage over longer time scales. Model predictive control (MPC) is one approach particularly suited to supervisory control, as it uses a dynamic process model to predict future system behaviour and optimises control actions over a finite horizon while accounting for operational constraints [66].

For islanded green ammonia production, MPC has been applied to determine plant production setpoints and the allocation of available renewable power under imperfect weather forecasts, showing that stable plant-level scheduling is possible without assuming perfect knowledge of future renewable generation [74]. At the synthesis-loop level, dynamic studies indicate that reactor inlet temperature and the hydrogen-to-nitrogen feed ratio are particularly influential during changes in production rate [91]. Variable-load operation of a Haber–Bosch process has also been demonstrated under predictive control while maintaining reactor temperatures, separation pressure and liquid inventory within their operating ranges [47].

Together, these studies indicate that autonomous operation requires coordination between plant-wide energy management and detailed process control. Forecast-based control can reduce the buffer needed to avoid shutdowns, but it cannot replace energy that is not generated; the trade-off between storage capacity and control sophistication is therefore part of the design problem. This thesis focuses

on the techno-economic feasibility of autonomous operation rather than the design of a specific control architecture, but the insights on energy allocation, storage sizing and production scheduling developed through the model provide the foundation for such a framework.

1.4.3. Safety, fault management and maintenance

Autonomy is not only a production-control challenge but also a safety requirement. An unattended plant must detect abnormal conditions, identify faults and take corrective action or transition to a safe state when recovery is not possible [54]. For ammonia plants, this requires reliable gas detection, process monitoring, isolation and emergency shutdown systems because accidental releases can create serious toxic exposure risks [21]. Redundant sensors and communication systems may also be required to prevent a single failure from disabling these safety functions.

Artificial intelligence and data-driven methods can support fault detection, predictive maintenance and operational decision-making. However, they should not fully replace human judgement during unfamiliar or safety-critical situations. Routine operation can therefore be automated while exceptional conditions are escalated to a remote operator [7].

In this thesis, the model focuses on operational autonomy under variable renewable supply, including energy allocation, production adjustment, storage management and operating-state transitions. Detailed safety-system design, fault diagnosis, predictive maintenance and component redundancy are outside the dynamic model scope.

1.4.4. Benefits of autonomy

The main potential benefits of autonomous operation are:

- **Reduced staffing requirements:** Autonomous routine operation reduces the need for continuous on-site staffing. This is particularly valuable for small, remote plants, where transport, accommodation and shift coverage can add significantly to operating costs.
- **Reduced human exposure to hazards:** Automated monitoring and control reduce the need for operators to perform routine tasks near process equipment. This is especially relevant for ammonia plants because accidental releases can create serious toxic exposure risks [21].
- **Improved operational performance:** Self-optimising control frameworks allow the plant to track its economically optimal operating point as renewable input fluctuates, rather than relying on manual adjustment [45].

1.5. Decentralisation

In this research, decentralised production refers to stand-alone ammonia plants located in remote regions and operating independently from the electricity grid. Such plants are particularly relevant in areas with strong renewable resources, low population density and sufficient land availability. The following subsections discuss feedstock self-sufficiency, the potential for modular deployment in suitable locations, and the additional technical requirements associated with remote operation.

1.5.1. Feedstock self-sufficiency

As discussed in Section 1.3, green ammonia can be produced using locally sourced nitrogen and water together with renewable electricity. This is particularly advantageous for decentralised production, as it reduces dependence on externally supplied feedstocks, provided that sufficient water is available locally.

1.5.2. Location and modular deployment

Remote regions with strong renewable resources and low population density can support off-grid ammonia production with limited land-use conflict. Multiple modular plants could be deployed within the same region, reaching a significant combined production scale while sharing infrastructure for transport, maintenance and storage. When located near agricultural markets or distribution hubs, this could further reduce transport costs and emissions [64]. Figure 1.4 illustrates that several regions combine low population density with high photovoltaic electricity potential, indicating favourable conditions for modular deployment. These considerations guided the selection of the three case-study locations presented in Section 1.8.

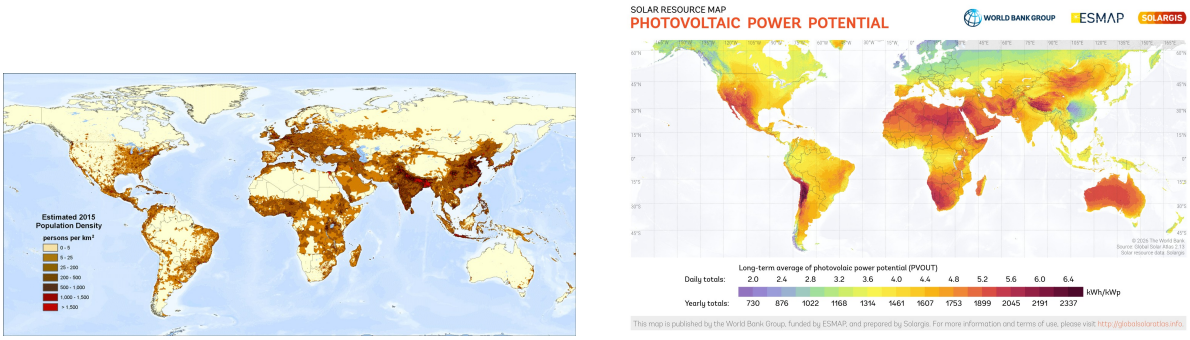

(a) Global population density [76].

(b) Global photovoltaic electricity potential [82].

Figure 1.4: Comparison of global population density and photovoltaic electricity potential, highlighting regions with low population density, available land and strong solar resources.

1.5.3. Remote-operation requirements

Off-grid production avoids dependence on electricity-grid infrastructure, but increases the need for energy storage, water treatment, redundancy, communication systems and maintenance access. These requirements can increase capital and operating costs, particularly in remote locations, and should therefore be considered when assessing the economic feasibility of autonomous ammonia production.

1.6. Plant scale

Closely related to plant location is the question of scale. This section examines the economics of scale in conventional ammonia production, how these change when ammonia synthesis is coupled to modular renewable electrolysis, and where the $\sim$1 t/day scale considered in this thesis fits within this broader context.

1.6.1. Economies of scale in conventional ammonia production

Conventional Haber–Bosch plants are generally constructed at large capacities because the capital cost per unit of production decreases as plant size increases. This effect is often approximated using the “six-tenth rule”, which assumes that total capital cost scales with capacity to an exponent of approximately 0.6 when process-specific data are unavailable [1]. Total capital cost therefore increases less than proportionally with production capacity, causing the specific capital cost to decrease as plant size increases.

Economies of scale have historically favoured large, centralised ammonia plants. Major equipment and balance-of-plant infrastructure contain substantial fixed-cost elements that do not decrease proportionally when capacity is reduced. At smaller scales, minimum equipment sizes, engineering, control and safety requirements therefore represent a larger cost per tonne of ammonia. Moreover, the six-tenth rule is a general rule of thumb developed for large plants and becomes increasingly uncertain when extrapolated to decentralised production.

Modular construction and reduced transport requirements may partly offset this scale disadvantage, but small-scale production generally remains subject to higher specific plant costs [52].

1.6.2. Modularity in renewable-powered production

Renewable-powered ammonia production can partly change the conventional scaling logic by allowing the plant to be built from standardised, repeatable modules rather than as one fully custom-designed facility. Cost reductions can therefore arise through repeated manufacturing and technological learning, often described as economies of numbers, instead of only through increasing the size of individual equipment [6]. Modularity can also make plant capacity easier to expand in steps [64].

Modular plants may therefore become attractive when manufacturing benefits, local renewable resources and reduced distribution requirements are considered together [64]. However, shared infrastructure, compression, separation, storage and other balance-of-plant components still benefit from larger scale.

1.6.3. Relevance for this thesis

This thesis evaluates whether a decentralised, autonomous green-ammonia plant at the $\sim$1 t day^{-1} scale can operate self-sufficiently, robustly and economically within its intended remote and off-grid context, while using large-scale centralised Haber–Bosch production as an economic benchmark. Although this scale sacrifices conventional economies of scale, it enables modular equipment, a smaller plant footprint, off-grid siting and production matched to local or regional demand. The thesis therefore assesses whether these benefits can offset the scaling penalty, with the selected range defining the equipment, cost basis and operational assumptions.

1.7. Levelised cost of ammonia

The economic performance of the plant is assessed using the levelised cost of ammonia (LCOA), defined as the total annualised cost of the production system divided by the annual ammonia output [73]. It enables comparison between production routes, locations and plant configurations while accounting for capital expenditure, operating costs, financing assumptions and plant utilisation.

For an autonomous off-grid plant, the system boundary includes renewable electricity generation, energy and feedstock storage, ammonia production equipment, nitrogen and water supply, product separation and storage, and the balance of plant. Since electricity is generated on-site, its cost is represented through the annualised capital and operating costs of the renewable generation and storage systems rather than through an external electricity tariff.

The use of modelled annual production is particularly important because renewable intermittency, curtailment, part-load operation and downtime can reduce plant utilisation. Smaller plants may also experience higher specific capital costs because equipment and balance-of-plant costs do not scale proportionally with production capacity [52]. The equations, financial assumptions and component-level parameterisation used to calculate the LCOA are presented in the Methodology.

1.8. Research gap and research questions

Relevant academic research has already explored key topics such as decentralised production, renewable energy integration and flexible plant operation under intermittent power supply. The techno-economic work by Nayak-Luke et al. (2018) [60] and Nayak-Luke and Bañares-Alcántara (2020) [61] established a reference levelised cost of ammonia framework for islanded green ammonia and demonstrated how renewable intermittency affects plant sizing and cost. Fahr et al. (2025) [22] extended research in this field with a detailed dynamic simulation of a flexible Haber–Bosch plant using PI controllers and feedforward control strategies.

Most existing techno-economic studies remain centred on Haber–Bosch-based production, including conventional, electrified and small-scale configurations. Lin et al. (2020) [52] add a relevant perspective by analysing small-scale Haber–Bosch production with absorption-enhanced ammonia removal, while Rouwenhorst and Lefferts (2020) [70] assess direct plasma-catalytic ammonia synthesis. The study most directly relevant to this thesis is Izelaar et al. (2024) [43], which provides a detailed techno-economic assessment of several small-scale electrochemical ammonia production pathways and benchmarks them against electrified Haber–Bosch. They modelled fully integrated plants for several electrochemical pathways and identified the performance levels required for cost competitiveness. Their analysis uses assumed electrochemical performance parameters, supported by simplified models of electrochemical losses, which are subsequently varied to assess their influence on cost. Their work therefore offers a valuable foundation for evaluating emerging technologies. This thesis builds on it by examining route-specific thermodynamic and kinetic limitations through reduced-order models, assessing realistic combinations of electrochemical performance parameters, and considering these technologies in the context of intermittent renewable, off-grid operation.

Consequently, two related gaps remain: the techno-economic feasibility of autonomous, decentralised green Haber–Bosch under intermittent renewable supply, and the extent to which emerging electrochemical synthesis routes can realistically approach competitiveness when their underlying electrochemical performance and limitations are considered. This thesis addresses these gaps through an integrated techno-economic assessment of decentralised, autonomous green ammonia production powered by renewable energy, combining technology selection, intermittent operation, small-scale economics and autonomous plant design within a single framework. This leads to the two main research questions of this thesis:

1. *What is the techno-economic feasibility of a decentralised autonomous green Haber–Bosch plant powered by renewable energy sources?*
2. *To what extent can emerging electrochemical nitrogen reduction routes provide a competitive alternative to conventional green Haber–Bosch ammonia production?*

The first question is addressed through technology selection, energy and mass balance modelling, and location-specific techno-economic optimisation, accounting for renewable intermittency, system sizing and operational reliability. The resulting configuration serves as the benchmark for the second question, which evaluates emerging electrochemical synthesis routes using reduced-order models based on reported electrochemical performance.

The scope of the study is limited to autonomous, off-grid operation relying solely on locally available renewable energy and feedstock, with minimal human or external intervention. The concept is evaluated at three locations: Geraldton, Australia; Lüderitz, Namibia; and Neom, Saudi Arabia, as shown in Figure 1.5. These locations are selected for their favourable renewable energy profiles, abundant land availability and relevance for remote or off-grid ammonia production (Section 1.5). Wind resources are also considered in the optimisation, given their potential to complement solar generation, and the choice of locations was further constrained by the availability of renewable energy data within the simulation software. The plant configuration depends on the synthesis route. The Haber–Bosch configuration includes solar PV, wind generation, battery storage, nitrogen supply, water electrolysis, ammonia separation and storage. Alternative synthesis routes, such as electrochemical NRR, require different route-specific components.



Figure 1.5: Selected locations for the autonomous ammonia plant case studies.

1.9. Thesis outline

The thesis is structured as follows. Chapter 2 describes the methods used to answer both research questions. For the autonomous plant, these include a technology selection using multi-criteria decision analysis (MCDA), a plant-level energy and mass balance, an hourly simulation of plant operation and a cost optimisation across the three locations, followed by an uncertainty analysis of the levelised cost. For the second research question, it introduces reduced-order models of the three NRR routes and the framework used to compare them with the electrolyser–Haber–Bosch plant. Chapter 3 presents the results for both research questions, from the selected technologies and the optimised plant configurations to the performance gap of the NRR routes. Chapter 4 discusses the robustness of these results and their implications for decentralised ammonia production. Chapter 5 answers the research questions, and Chapter 6 outlines directions for future work.

2

Methodology

Potential technologies for the individual plant subprocesses are first evaluated using a Multi-Criteria Decision Analysis (MCDA). The selected configuration is then modelled on an hourly basis and optimised for cost under renewable intermittency and operational constraints. In parallel, reduced-order models are developed for the electrochemical NRR routes to relate cell-level performance to energy consumption and production rate. The resulting pathways are finally compared on a common technical and economic basis.

The chapter is organised as follows. Section 2.1 presents the MCDA framework, including the criteria, weighting and scoring procedure used to select the subprocess technologies. Section 2.2 defines the plant-level energy and mass balance, while Section 2.3 describes the FESM tool used for system-level optimisation and as a benchmark for component sizing and cost. Section 2.5 defines how plant autonomy is assessed. Section 2.4 develops the autonomous Haber–Bosch base-case model, together with its cost model and configuration optimisation. Section 2.6 then develops the reduced-order electrochemical models for the three NRR routes, and Section 2.7 establishes the framework used to compare their energy consumption and production performance with the Haber–Bosch benchmark. Finally, Section 2.8 describes the sensitivity analysis used to assess the principal technical and economic assumptions.

2.1. Multi Criteria Decision Analysis

Multi-Criteria Decision Analysis (MCDA) is a structured decision-support method used to compare alternatives across multiple predefined criteria. It is particularly suitable for complex decisions in which technical, economic and operational considerations cannot be represented by a single performance indicator. In this thesis, MCDA is applied at several decision points to evaluate alternative technologies for the individual subprocesses of the autonomous ammonia plant. Each option is assessed using a common set of weighted criteria and assigned a corresponding score, providing a transparent and systematic basis for technology selection. The plant is therefore decomposed into distinct functional subsystems, with each subsystem representing a specific process or component required for autonomous ammonia production.

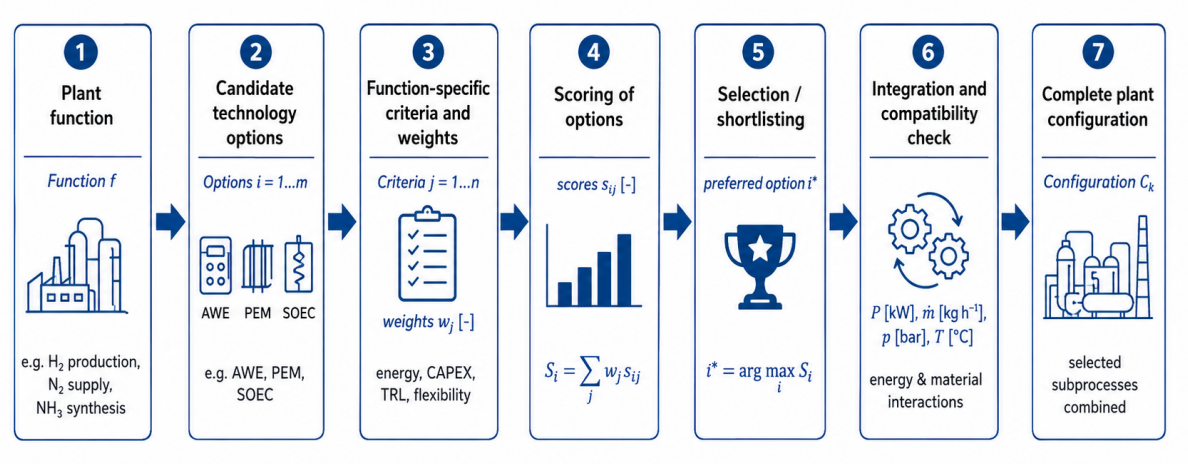

Figure 2.1: MCDA workflow for plant configuration selection.

The candidate technologies are ranked using the weighted-sum model (WSM), also referred to as Simple Additive Weighting (SAW) [88]. Each technology option i is assigned a dimensionless score s_{ij} for each criterion j, while each criterion is assigned a weight w_j representing its relative importance. The overall weighted score of option i is calculated as:

$$S_i = \sum_{j=1}^{n} w_j s_{ij}, \tag{2.1}$$

where S_i is the total score of technology option i, n is the number of criteria, w_j is the weight of criterion j, and s_{ij} is the score assigned to option i for criterion j. The option with the highest overall score is selected or shortlisted for the subsequent integration and compatibility assessment.

2.1.1. Criteria

The evaluation criteria are defined to provide a comprehensive assessment of the suitability of each technology option for autonomous ammonia production. The criteria and their associated indicators or potential units are defined as follows:

- **Autonomy:** Ability of the subprocess to operate with minimal human intervention, assessed through self-regulation capability, maintenance requirements and mean time between maintenance (MTBM).
- **Costs:** Total costs associated with implementing and operating the subprocess, including capital expenditure (CAPEX) and operational expenditure (OPEX). Where applicable, costs are expressed through their contribution to the levelised cost of ammonia in \$/kg$_{\mathrm{NH_3}}$.
- **Energy:** Specific net energy consumption of the subprocess, derived from thermodynamic analysis or operating data and expressed using a suitable metric, such as kWh/kg$_{\mathrm{NH_3}}$.
- **Intermittent compatibility:** Ability of the subprocess to adjust to variable renewable-power input, considering ramping rates, start-up time, minimum-load requirements and part-load operation.
- **Modularity:** Suitability of the subprocess for deployment as smaller, repeatable units that can be combined, replaced or expanded without substantial redesign.
- **Operational conditions:** Severity of the operating conditions required by the subprocess, including temperature, pressure and sensitivity to variations in feedstock or power input.
- **Robustness:** Ability of the subprocess to withstand operational and environmental disturbances while maintaining stable performance and limiting component failure or degradation.
- **Scalability:** Ability to increase production capacity while maintaining comparable performance, efficiency, reliability and product quality.
- **Technology readiness level (TRL):** Maturity of the technology, indicating whether it remains at laboratory scale, has been demonstrated in pilot or industrial environments, or is commercially available.

Both technology performance and criterion importance are assessed using three-point ordinal scales, as summarised in Table 2.1. The limited scale reflects the predominantly qualitative nature of several criteria and avoids implying unsupported numerical precision.

Table 2.1: MCDA scoring and weighting scales.

Value	Technology performance	Criterion importance
3	Favourable	High
2	Intermediate	Medium
1	Unfavourable	Low

The criterion weights reflect their relative importance to the design of a decentralised, autonomous and off-grid ammonia plant.

High weight (3). Autonomy is weighted highly because the plant is intended to operate with limited human intervention and long maintenance intervals. Cost and energy directly affect economic competitiveness and the required renewable-generation and storage capacity, while robustness is essential for reliable off-grid operation with limited degradation and failures.

Medium weight (2). Intermittent compatibility and operational conditions influence how well a technology can operate under variable renewable supply and how demanding its temperature, pressure and control requirements are. Technology readiness is also weighted at this level, as greater maturity reduces technical and deployment risk without excluding less mature technologies with long-term potential.

Low weight (1). Modularity supports decentralised deployment, maintenance and expansion, while scalability determines how readily capacity can be increased. Both are relevant, but less decisive for this study than autonomy, cost, energy use and robustness, particularly because the focus is on small-scale rather than world-scale production.

The resulting criterion weights are summarised in Table 2.2.

Table 2.2: MCDA criterion weights.

Criterion	Weight
Autonomy	3
Costs	3
Energy	3
Intermittent compatibility	2
Modularity	1
Operational conditions	2
Robustness	3
Scalability	1
Technology readiness level	2

In this study, the MCDA framework is used as a structured decision-making tool to compare the technology options and support the selection of the preferred configuration. Since several technologies are still emerging and some criteria require qualitative judgement, the resulting scores are subject to uncertainty and should be interpreted as indicative rather than absolute. Options with similar scores are therefore assessed further using engineering judgement, data quality and their alignment with the objectives of the autonomous plant.

2.2. Plant-Level Energy and Mass Balance

The energy and mass balance provides the common basis on which all synthesis routes are compared. It covers the process chain from ambient air and water to the synthesis-loop outlet at steady-state design-point operation. Within this boundary, the plant is represented as a set of connected subsystems, each characterised by its inlet and outlet streams and its electricity demand, as shown in the extended

block diagram (Figure B.1). Renewable generation and energy storage are treated at system level (Section 3.4). Because every route is evaluated within the same boundary and per kilogram of ammonia, differences in the results reflect differences in process performance rather than in accounting.
Material flows follow from conservation and reaction stoichiometry. For each subsystem k,

$$\frac{\mathrm{d}M_k}{\mathrm{d}t} = \sum_{\text{in}} \dot{m}_k - \sum_{\text{out}} \dot{m}_k, \tag{2.2}$$

where the accumulation term is zero for process units at steady state and retained for storage inventories. With $2\,\mathrm{H_2O} \rightarrow 2\,\mathrm{H_2} + \mathrm{O_2}$ and $\mathrm{N_2} + 3\,\mathrm{H_2} \rightarrow 2\,\mathrm{NH_3}$, the ammonia production rate fixes the hydrogen, nitrogen and water demand and the oxygen by-product. The air intake additionally depends on the nitrogen recovery of the separation unit. Assuming negligible purge losses, unreacted nitrogen and hydrogen are fully recycled within the synthesis loop, resulting in complete overall conversion [80].

The electricity demand of each subsystem is calculated using literature-based parameters and thermodynamic relations. For water harvesting and pressure swing adsorption, specific energy consumption values are taken from literature. Electrolysis consumption is calculated from an assumed cell voltage and Faraday's law, while compression work is determined using ideal-gas relations and isentropic efficiencies. Reversible energy requirements are calculated separately to quantify the difference between theoretical and practical energy consumption. Heat released by the exothermic Haber–Bosch reaction is assumed to supply the required feed preheating and is therefore excluded from external electricity demand. The underlying equations and input parameters are provided in Appendix A.1.

The design-point specific electricity consumption is the external electricity demand per unit of product, $SEC_{\text{design}} = \sum_k P_k / \dot{m}_{\mathrm{NH_3}}$. In operation, part load, standby demand and storage losses add to this. The annual plant value is therefore

$$SEC_{\text{plant}} = \frac{\displaystyle\int_0^{t_{\text{year}}} \sum_k P_k(t)\,\mathrm{d}t}{m_{\mathrm{NH_3,annual}}}, \tag{2.3}$$

which includes periods without production. This is distinct from the cell-level consumption of the electrochemical models (Section 2.6.1), which enters as one subsystem input.

An exergy balance is used as a plant-level consistency check. It compares the external electricity input with the chemical exergy of the product, the vented oxygen and the recoverable heat, and treats the remainder as loss without attributing it to individual units.
The first-law efficiency is defined as:

$$\eta_{\mathrm{I}} = \frac{\dot{m}_{\mathrm{NH_3}}\,\mathrm{HHV}_{\mathrm{NH_3}}}{\sum_k P_k}, \tag{2.4}$$

using the higher heating value of ammonia, $\mathrm{HHV}_{\mathrm{NH_3}} = 22.5\ \mathrm{MJ\,kg^{-1}}$ ($6.25\ \mathrm{kWh\,kg^{-1}}$) [53]. Because most Haber–Bosch benchmarks are reported on a lower-heating-value basis ($18.6\ \mathrm{MJ\,kg^{-1}}$, $5.17\ \mathrm{kWh\,kg^{-1}}$) [80], the LHV-based efficiency is reported alongside.

2.3. Future Energy System Modelling

The Future Energy System Modelling tool (FESM) is used to establish the location-specific assumptions, renewable-energy profiles, and preliminary component sizes that serve as inputs to the detailed time-resolved plant simulation.

2.3.1. FESM framework

FESM is a Shell in-house linear-programming framework for designing integrated energy systems. For this study, FESM models green ammonia production using alkaline water electrolysis, air separation for nitrogen production, and Haber–Bosch ammonia synthesis. A scenario is further defined by its location, annual production target, available renewable-energy and storage technologies, and technical and economic constraints. Hourly renewable-energy profiles are combined with the process energy demands, after which FESM determines the component capacities that minimise total system cost while satisfying the specified production and energy-balance constraints.

The main outputs include the required capacities of solar PV, wind generation, battery storage, electrolysis, nitrogen production, and Haber-Bosch synthesis. FESM provides hourly energy flows, storage operation, component utilisation, renewable-energy curtailment, CAPEX, and levelised energy costs. It does not directly calculate the plant-specific energy consumption, SEC_{plant}, which is therefore determined separately from the simulated energy use and ammonia production.

The linear formulation limits the operational behaviour that FESM can represent. As a continuous linear program without integer variables, it cannot explicitly model discrete on–off decisions, minimum stable operating loads, start-up and shut-down times, standby operation, or ramping energy. FESM also determines the system configuration for an annual ammonia-production target using complete knowledge of the yearly renewable-energy profile. In contrast, the custom model evaluates autonomous operation against monthly production targets based on the available system conditions. FESM is therefore used as a system-level benchmark rather than as a direct representation of real-time plant operation.

2.3.2. Application in this thesis

FESM is applied to green-ammonia production in Neom, Saudi Arabia; Lüderitz, Namibia; and Geraldton, Australia. For each location, the annual production target is fixed at $300\ \mathrm{t_{NH_3}\,yr^{-1}}$, allowing the influence of the local renewable resource to be compared on a consistent basis. Hourly solar and wind profiles are obtained from the VORTEX weather-data environment and used both in the FESM optimisation and as renewable-energy inputs to the subsequent time-resolved plant model.

For each location, FESM provides an initial estimate of the required renewable-generation, battery, electrolyser and ammonia-synthesis capacities. FESM uses its own internal energy and cost assumptions, which differ from those of the custom model. Its results are therefore used as a preliminary sizing basis, an order-of-magnitude check and a benchmark for cost comparisons. However, the FESM configuration is not adopted directly as the base plant design, as the custom model incorporates route-specific operating states, ramping constraints, storage control and dispatch logic to evaluate autonomous operation and annual ammonia production.

2.4. Modelling

The plant is simulated in Python at hourly resolution against a production target of 25 t NH_3 per month. The base case evaluates a predefined solar-only configuration informed by preliminary FESM sizing and engineering judgement. It consists of a PV field, battery, alkaline electrolyser, hydrogen buffer, PSA nitrogen unit, atmospheric water harvester and Haber–Bosch loop over one meteorological year, and reports its production under variable renewable supply. The configuration optimisation (Section 2.4.3) then adds onshore wind and ammonia product storage. Each design is simulated over 15 meteorological years and must meet the monthly delivery target in at least 90% of the years, subject to the shortfall criterion defined in Section 2.4.3.

2.4.1. Base-case model

The base-case model evaluates the technical and economic performance of a fully renewable ammonia-production plant comprising a PV field, battery, alkaline electrolyser, hydrogen buffer, PSA nitrogen generator, atmospheric water harvesting and Haber–Bosch synthesis loop. The technologies are selected through the multi-criteria decision analysis presented in Section 2.1. The pseudocode and Python implementation are provided in Appendix C.1. The base case is evaluated against a monthly production target of 25 t NH_3. This target represents the minimum required delivered output and corresponds approximately to one ammonia truckload [10], linking the modelled production scale to a practical distribution unit for decentralised supply. It is used as the reference for assessing whether the predefined plant configuration is technically feasible under intermittent renewable supply. The model does not force exact production; instead, hourly operation determines the actual monthly and annual ammonia output.

The plant is simulated at an hourly resolution over one meteorological year. Site-specific capacity-factor profiles derived from Vortex solar data describe the hourly variation in solar availability. The electrical output of the PV field is calculated as

$$P_{\mathrm{PV}}(h) = CF(h)\, G_{\max}\, \eta_{\mathrm{PV}}\, A_{\mathrm{field}}, \tag{2.5}$$

where $CF(h)$ is the dimensionless hourly solar-resource capacity factor, $G_{\max} = 1000\ \mathrm{W\,m^{-2}}$ is the

reference irradiance, η_{PV} is the assumed PV-module conversion efficiency (22.5% [57]) and A_{field} is the installed PV-field area.

Subsystem-specific electricity consumptions translate process mass flows into hourly power demand, using the specific energies of Section 2.2 and Table A.1. Hydrogen production and ammonia synthesis are represented using stoichiometric mass balances, while the hydrogen buffer is modelled as a bounded hourly inventory. Nitrogen is supplied on demand by the PSA unit and is not stored separately. The overall plant SEC (Equation 2.3) is calculated from the total electricity consumed and ammonia produced and therefore includes battery, standby and ramping losses.

Electricity is allocated using a fixed dispatch hierarchy. The Haber–Bosch loop and PSA unit are supplied first because maintaining synthesis-loop operation reduces repeated start-up and shutdown. Remaining electricity is directed to the electrolyser, subject to its available capacity and the remaining hydrogen-buffer space. The battery supplies power deficits where possible and stores excess generation, while electricity that cannot be used or stored is curtailed.

The overall simulation structure is shown in Figure 2.2. The model first loads the meteorological data and design parameters, calculates the hourly PV generation and initialises the variables used to record production, storage levels, power flows and component states. After completing the hourly simulation, the results are aggregated into monthly and annual technical and economic indicators.

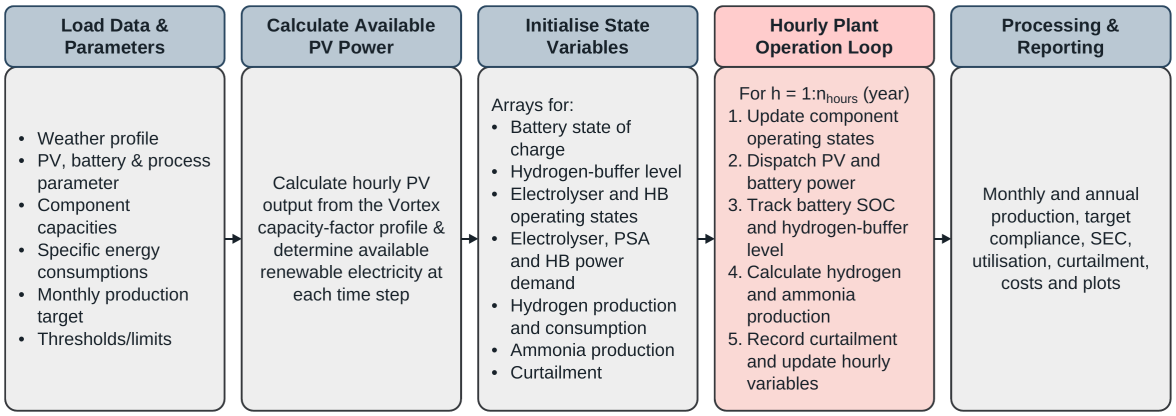

Figure 2.2: Modelling flowchart of the base-case model.

The hourly plant operation contains two coupled finite-state machines because the electrolyser and Haber–Bosch loop have different operating constraints. Both draw electricity from the PV array and battery, but electrolyser operation is mainly determined by the available power and hydrogen-buffer headroom, whereas the Haber–Bosch loop also depends on the hydrogen inventory and its more restrictive operating dynamics.

Both components can be in the states producing, ramping up, ramping down, standby and off. In the standby state, both components consume power to maintain operating conditions close to those required for production, allowing a faster return to normal operation without producing hydrogen or ammonia. The specific transition criteria, power requirements and durations associated with these states are described in the following subsections.

The two state machines are evaluated sequentially during each hour, as shown in Figure 2.3. The Haber–Bosch state is evaluated first because its electricity demand has dispatch priority and determines the power remaining for hydrogen production. The electrolyser state is evaluated second, after which hydrogen production and consumption are applied to the buffer inventory.

The hydrogen buffer links the two operating logics. Its inventory determines whether the Haber–Bosch loop can start or continue producing, while its remaining capacity limits electrolyser operation. The buffer therefore decouples intermittent hydrogen production from ammonia synthesis, while the battery buffers short-term variations in the electrical supply to both subsystems.

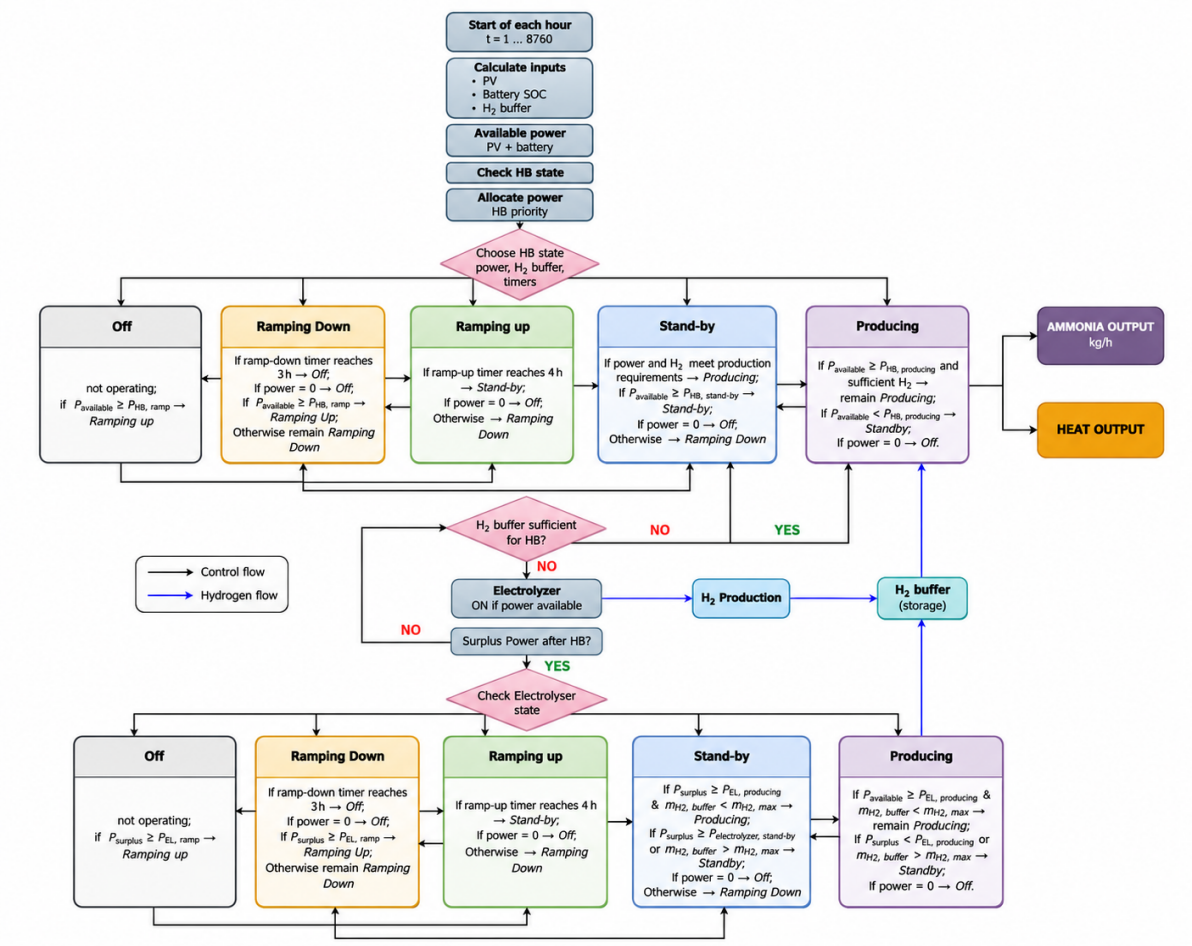

Figure 2.3: Hourly plant-operation loop and coupling between the component state machines

Haber--Bosch loop operating states

The Haber–Bosch loop operates in five states: producing, hot standby, ramping up, ramping down, and off as shown in figure 2.4. A cold start begins when PV and battery power can sustain the minimum production load, set at 30% of the maximum hydrogen feed rate, which is conservative [69]. Heating and pressurising the loop is assumed to take six hours at minimum-load power without ammonia production; as no start-up duration for this scale was found. If the hydrogen buffer cannot supply the minimum feed once ramp-up is complete, the loop enters hot standby.

Continuous circulation is particularly important for the HB process because the single-pass conversion is only about 15% [80]. Most unreacted hydrogen and nitrogen must therefore be recycled through the synthesis loop. During production, hydrogen consumption is limited by the installed HB capacity, the buffer inventory, and the rate supported by the available electricity. If the hydrogen feed falls below 30% of the maximum feed rate, the loop enters hot standby. During hot standby, the loop consumes 15% of its rated electrical power to maintain temperature, pressure and internal circulation, without producing ammonia. This allows rapid return to production once sufficient hydrogen is available.

If the available PV and battery power can no longer sustain ramp-up or hot standby, the loop begins a controlled three-hour ramp-down at 10% of the full electrical load before entering the off state. Because restarting the pressurised recycle loop is slower and more energy intensive than maintaining hot standby [68], hydrogen-buffer availability and dispatch priority strongly influence the annual operating performance.

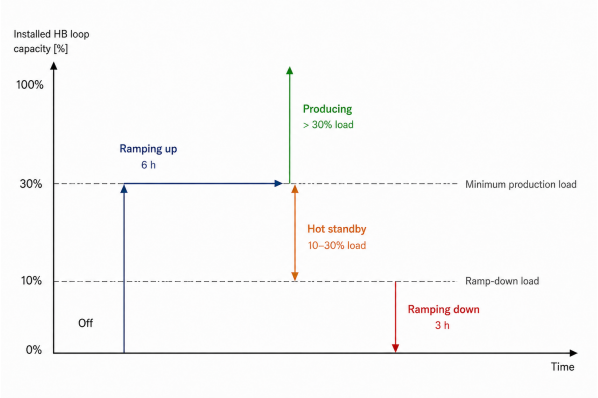

Figure 2.4: Overview of the Haber–Bosch synthesis-loop state logic

Electrolyser operating states

The electrolyser operates in five states: producing, standby, ramping up, ramping down, and off as shown in figure 2.5. Its state depends on the surplus power remaining after the HB loop and PSA demand and on the available headroom in the hydrogen buffer. Ramp-up starts when sufficient power is available to sustain the minimum production load of 15% of installed capacity. A cold-start duration of four hours is assumed, during which no usable hydrogen production is credited [67]. This accounts for the time required to heat and pressurise the alkaline electrolyser before normal operation can resume, with thermal dynamics being the main limiting factor [56].

Below 7%, a controlled three-hour ramp-down begins. Transition progress is retained when the direction changes, so recovered power during ramp-down first reverses the completed shutdown progress. If power falls to zero and cannot be supported by the battery, hydrogen production stops immediately and the electrolyser enters the off state. Such abrupt shutdowns are recorded because shutdown-induced reverse currents can accelerate electrode degradation [46].

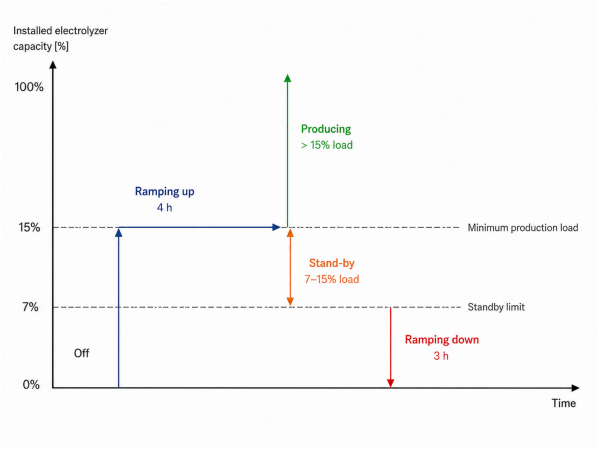

Figure 2.5: Overview of the electrolyser state logic

Hydrogen Buffer

The hydrogen buffer is a fixed-capacity mass inventory, filled by the electrolyser and drained by the HB loop, tracked hourly. The electrolyser load is capped by the remaining buffer headroom, so overflow is structurally prevented; surplus power that cannot be absorbed is recorded as curtailment. By decoupling intermittent hydrogen production from the synthesis loop, the buffer provides additional operational flexibility.

2.4.2. Cost Modelling

Capital expenditure is evaluated for each subsystem by multiplying its installed capacity by the corresponding unit capital cost,

$$\mathrm{CAPEX}_i = c_i S_i, \qquad i \in \mathcal{D}, \tag{2.6}$$

where $\mathcal{D}$ is the set of explicitly sized subsystems, comprising the PV field, battery, wind capacity, electrolyser, synthesis loop, hydrogen buffer, ammonia storage and nitrogen unit, and S_i is the installed capacity of component i obtained from the simulation. The unit cost c_i (Table A.6) is based on literature estimates adjusted to the scale, scope and system boundaries of the plant. Component-level installation and balance-of-system costs are included where covered by the underlying sources.

No additional site-wide balance-of-plant allowance is applied in the baseline model to avoid potential double counting of costs already included in the component estimates. The effect of additional infrastructure costs is examined through a 5% cost uplift in the sensitivity analysis. Uncertainty in the component cost assumptions is further assessed through the Monte Carlo analysis described in Section 2.4.4.

The water-supply unit is excluded from $\mathcal{D}$. At 1.6 kg of water per kilogram of ammonia the plant needs about 1.3 m^3 per day to meet the production target. Its capital cost is expected to be small relative to the other plant components, but reliable estimates are difficult to establish, particularly for atmospheric water harvesting. Water-supply CAPEX is therefore neglected, while its electricity consumption is included.

Each component is subsequently annualised over its technical lifetime using the capital recovery factor,

$$\mathrm{CRF}(r, n_i) = \frac{r(1+r)^{n_i}}{(1+r)^{n_i} - 1}, \tag{2.7}$$

where r is the discount rate and n_i is the lifetime of component i, both given in Table A.6. Component-specific lifetimes are applied to account for differences in replacement frequency. Annual operating expenditure is represented by a fixed fraction $f_{\mathrm{opex},i}$ of the capital cost of each component (Table A.6). Before the cost of ammonia is evaluated, the cost of the electricity supply is reported separately. The levelised cost of electricity is commonly used to compare power-supply options. In this study it is calculated as a delivered electricity cost for the autonomous plant:

$$\mathrm{LCOE}_{\mathrm{delivered}} = \frac{\sum_{i \in \{\mathrm{PV,wind,battery}\}} \mathrm{CAPEX}_i \left[\mathrm{CRF}(r, n_i) + f_{\mathrm{opex},i}\right]}{E_{\mathrm{delivered}}}, \tag{2.8}$$

where the numerator includes the annualised cost of the PV field, onshore wind turbines and battery. The denominator, $E_{\mathrm{delivered}}$, is the electricity delivered to the ammonia-production process over the year.

Because the denominator is based on electricity taken up by the process rather than total renewable generation, curtailment and battery round-trip losses are carried as system costs without appearing as useful output. The resulting $\mathrm{LCOE}_{\mathrm{delivered}}$ is therefore not directly equivalent to published grid-connected LCOE values for standalone solar or wind farms. However, it remains useful as an indicative benchmark, since comparison with published values shows whether the autonomous electricity supply is within the same order of magnitude as established renewable-generation costs.

The levelised cost of ammonia follows from the total annualised expenditure divided by the ammonia produced over the year,

$$\mathrm{LCOA}_{\mathrm{annual}} = \frac{\displaystyle\sum_{i \in \mathcal{D}} \mathrm{CAPEX}_i \left[\mathrm{CRF}(r, n_i) + f_{\mathrm{opex},i}\right]}{m_{\mathrm{NH_3,annual}}}. \tag{2.9}$$

where $m_{\mathrm{NH_3,annual}}$ is the annual ammonia production obtained from the simulation. This is the conventional definition and is used as the objective in the configuration optimisation, as it distributes the annualised plant cost over all ammonia produced and therefore assumes that all production can be sold. Since the offtake agreement considered here specifies a fixed monthly volume, a second value is reported in which the denominator is limited to the contracted annual volume,

$$m_{\mathrm{NH_3,contracted}} = 12\, m_{\mathrm{NH_3,target}}, \tag{2.10}$$

where $m_{\mathrm{NH_3,target}}$ is the monthly production target. Any production above this contracted volume therefore still contributes to the plant cost but is not credited as saleable output. The difference between the two LCOA values consequently represents the cost penalty associated with oversizing the plant relative to the contracted offtake.

2.4.3. Configuration optimisation

The cost model assigns a levelised cost to a given configuration, but does not identify the least-cost plant that satisfies the production target. In the base case, component sizes are specified inputs selected to represent a plausible design. A configuration optimisation is therefore applied to determine a more cost-effective combination of subsystem capacities. The pseudocode for the configuration optimisation is provided in Appendix C.2.

The optimisation varies the PV field area, onshore wind capacity, battery capacity, electrolyser rating, hydrogen-buffer capacity, synthesis-loop capacity and ammonia storage capacity within prescribed ranges. Wind generation is calculated analogously to Equation (2.5), as $P_{\mathrm{wind}}(h) = CF_{\mathrm{wind}}(h)\,P_{\mathrm{wind,rated}}$, using hourly capacity factors. A coarse-to-fine grid search is first used to identify a promising region of the design space. For the contracted-cost objective, a subsequent full-grid search evaluates candidates from cheapest to most expensive, allowing more expensive designs to be excluded without simulation.

Each configuration is evaluated over 15 consecutive historical meteorological years and evaluated against the monthly production target of 25 t NH_3 defined in Section 2.4.1. A configuration is considered feasible if the monthly target is met in at least 90% of simulated years, while the average shortfall in the remaining years must stay below 2% of annual contracted production. This allows for occasional shortfalls during unfavourable weather conditions without oversizing the system to meet the target in every year.

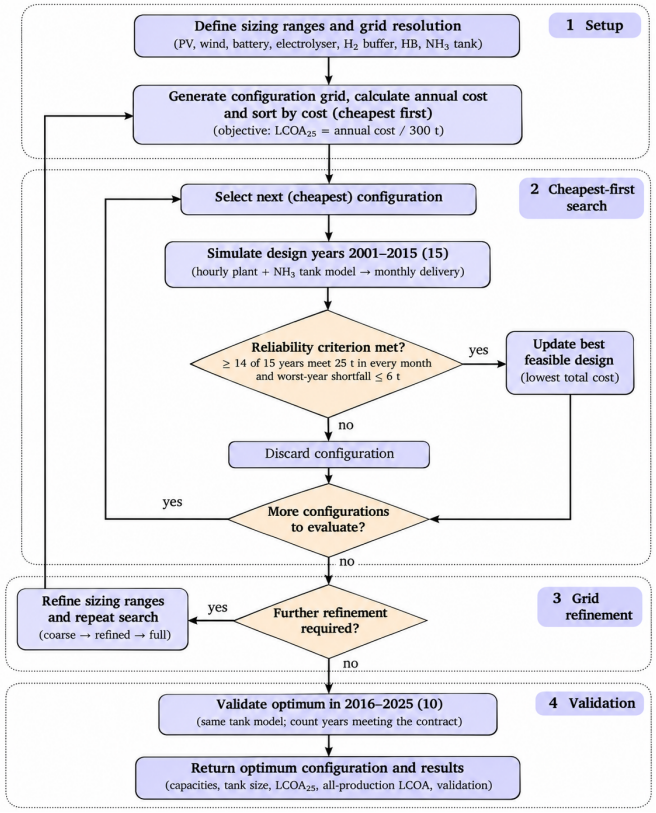

Figure 2.6: Coarse-to-fine configuration optimisation procedure

Configurations that do not satisfy these requirements are excluded. The cost model is used to rank the candidates, and the lowest-cost feasible configuration is selected. The optimisation considers both contracted LCOA, based on 300 t/year, and LCOA based on total production. An additional 10 historical meteorological years are excluded from the optimisation procedure and reserved exclusively for out-of-sample validation of the resulting design, for which the same feasibility criteria are assessed.

By varying all seven capacities together, the optimisation accounts for interactions that a single design point cannot reveal. Enlarging one subsystem often reduces the capacity required elsewhere: additional battery storage and a larger PV field both raise the hydrogen supply during low-irradiance periods, and either can relieve the buffer. The resulting design therefore reflects a system-level balance rather than a component-by-component optimum. Since feasible configurations are assessed using the same simulation, feasibility criterion and cost model, the optimised plant is directly comparable with the base case and with the FESM benchmark of Section 3.3.

The full-grid search identifies the least-cost feasible configuration within the specified discrete grid for the contracted-cost objective. However, it does not guarantee a global optimum across continuous capacity values. The all-production objective is evaluated using the coarse-to-fine search and therefore

remains heuristic. The resulting configurations should thus be interpreted as low-cost feasible designs within the investigated design space.

2.4.4. Probabilistic LCOA

The deterministic LCOA depends strongly on assumed component costs, which vary considerably across published estimates for small-scale renewable ammonia plants. It is therefore important to assess how uncertainty in these assumptions affects the estimated production cost. A one-at-a-time sensitivity analysis identifies the influence of individual parameters [83]. To assess their combined effect, a Monte Carlo analysis samples uncertain inputs simultaneously and propagates them through the full cost model, including non-linear terms such as the capital recovery factor. This produces a distribution of possible LCOA values. The capacities of the optimised plant are held fixed in every draw, so the resulting distribution captures cost and operating uncertainty for the fixed plant configuration. Each case uses $N = 10\,000$ draws with a fixed random seed; implementation details are provided in Appendix A.5.2.

For each costed component, a minimum a, most-likely m and maximum b capital cost are specified. The most-likely value corresponds to the deterministic model, while the minimum and maximum are based on the lowest and highest values found in the literature. The ranges for all sampled inputs are listed in Table A.23 (Appendix A.5.2).

The beta-PERT distribution is selected because it can be parameterised using minimum, most-likely and maximum estimates, remains bounded by the specified range, and accommodates asymmetric uncertainty around the most-likely value [92]. It is particularly suitable here because the most-likely values have been investigated more thoroughly, especially regarding their consistency with the system boundaries, than the literature-derived minimum and maximum estimates. Capital costs are sampled from beta-PERT distributions on $[a, b]$.

$$\alpha = 1 + \lambda \frac{m-a}{b-a}, \qquad \beta = 1 + \lambda \frac{b-m}{b-a}, \qquad \lambda = 4. \tag{2.11}$$

Each value is obtained by inverse transform sampling: a uniform random number $U \in (0, 1)$ is mapped to a cost through the inverse cumulative distribution function of the component's distribution. A triangular distribution with the same bounds is used as a distributional sensitivity.

Draws are independent in the baseline. Dependence between component costs is tested with a one-factor Gaussian copula,

$$Z_i = \sqrt{\rho}\, Z_0 + \sqrt{1-\rho}\, \varepsilon_i, \qquad X_i = F_i^{-1}(\Phi(Z_i))\,, \tag{2.12}$$

where Z_0 and ε_i are independent standard normal variables, Φ is the standard normal distribution function and F_i^{-1} is the inverse distribution function of component i. All components share an equal pairwise latent correlation of $\rho = 0.5$ or, as an upper bound, $\rho = 1$. The marginal distributions are unchanged, and the correlations are scenario assumptions rather than estimates from observed price data.

Using these sampling methods, component capital costs, the discount rate, a shared O&M multiplier, and battery and electrolyser lifetimes are drawn from their respective probability distributions. The annualised cost C_k is calculated using the capital recovery factor (Equation (2.7)) and fixed O&M costs. The sampled discount rate and component lifetimes determine the CRF, while the O&M multiplier adjusts annual operating costs. No separate replacement cost is added, as component lifetimes are accounted for through the CRF.

The contracted LCOA is then calculated for each Monte Carlo draw as

$$\mathrm{LCOA}_{\mathrm{con},k} = \frac{C_k}{m_{\mathrm{NH_3,con}}}, \tag{2.13}$$

where $m_{\mathrm{NH_3,con}} = 300$ t/yr is the fixed annual contractual volume. The resulting distribution quantifies uncertainty in the cost of the optimised configuration, assuming the monthly production requirement is satisfied.

The influence of individual cost assumptions is assessed using Spearman rank correlations between sampled inputs and the resulting contracted LCOA. The Monte Carlo results are summarised by the 10th, 50th and 90th percentiles of the LCOA distribution. These percentiles depend on the assumed

uncertainty ranges, probability distributions and correlations, and should not be interpreted as statistical confidence intervals.

2.5. Autonomy analysis

The autonomy analysis evaluates whether the optimised plant can maintain reliable operation under variable renewable electricity supply, without a grid connection or continuous human intervention, as defined in Section 1.4. Renewable shortages must be managed through the installed storage and the plant's operating strategy. The objective is therefore to assess the operational limitations of the least-cost configuration and the flexibility available to maintain production during periods of low renewable generation.

Groot et al.[29] investigates autonomy in a comparable off-grid methanol plant using four control strategies applied to a fixed plant configuration. Two are reactive: a five-state controller and a night-survival heuristic that adjusts operation based on the energy available until sunrise. The other two use model predictive control (MPC) with a six-hour forecast horizon, considering both perfect and uncertain weather forecasts. These strategies illustrate how improved control can reduce production interruptions without changing the installed capacities.

This study takes a different approach. Rather than comparing controllers for a fixed plant, the operating strategy described in Section 2.4 is kept constant while seven plant capacities are optimised in Section 2.4.3. Groot's night-survival strategy is less directly applicable because the plant combines solar and wind generation, and shortages can extend over several days rather than individual nights. Predictive control could improve operation, but assessing its benefits would require additional forecasting and controller modelling. The analysis therefore focuses on the autonomy of the optimised configuration under the existing control strategy.

Autonomy is evaluated using five indicators derived from the hourly simulations: (i) the share of time the electrolyser and Haber–Bosch loop spend in off or standby states; (ii) the number of ramp-up attempts and aborted starts; (iii) hydrogen-buffer autonomy, expressed as hours of Haber–Bosch operation at minimum load; (iv) battery throughput in equivalent full cycles; and (v) the production margin in the weakest month relative to the 25 t monthly target. Together, these indicators describe production interruptions, storage utilisation and the ability to meet contractual delivery requirements.

No additional controller is implemented. The analysis is limited to the operating behaviour captured by the hourly dispatch model and does not assess shorter-timescale control or maintenance requirements. Section 3.6 evaluates these indicators and examines the trade-off between additional installed capacity and improved operational reliability.

2.6. Reduced-order electrochemical NRR modelling

Comprehensive kinetic and thermodynamic are not available for all three routes, so aqueous NRR, Li-mediated NRR and water-fed membrane Li-mediated NRR are each represented by a reduced-order model combining thermodynamic limits, experimentally anchored operating data, and simplified kinetic and transport relations. All three are evaluated on the same four metrics: ammonia production rate, Faradaic efficiency, full-cell voltage and specific electricity consumption. The performance gaps against the Haber–Bosch benchmark are therefore directly comparable.

2.6.1. Aqueous NRR performance model

The aqueous NRR model uses a reduced-order, literature-informed approach because validated polarization data for the ammonia partial current are unavailable. The logic is: sweep the cathode potential E, compute the HER and NRR partial currents independently, determine the catalyst-site coverage, cap the NRR current by nitrogen transport, and obtain the Faradaic efficiency as their ratio.

Two design choices follow from the lack of validated kinetics. First, the absolute current scale is fixed by calibrating to a single experimental operating point. That point is selected from a study meeting the isotope-labelling and contamination controls of the Andersen protocol [3]. This provides a reliable calibration point supported by experimental verification.

Second, The hydrogen-coverage mechanism described by Choi [14] determines the modelled decline in NRR activity at negative potentials. The model is built for performance-gap analysis: each parameter is an explicit, physically identifiable lever. Parameters are labelled measured (M), derived (D) and assumed (A).

Step 0: Boundary conditions
The base case is $T = 298$ K, $p_{\mathrm{N_2}} = 1$ bar, near-neutral aqueous electrolyte. The independent variable is the cathode potential E, expressed versus RHE via:

$$E_{\mathrm{RHE}} = E_{\mathrm{meas}} + E_{\mathrm{ref}}^{\mathrm{SHE}} + (2.303RT/F)\,\mathrm{pH} \tag{2.14}$$

The RHE scale is used because it removes the formal pH shift of the hydrogen equilibrium, letting HER and NRR share one potential axis (Step 1).

Step 1: Thermodynamic potentials (D)
From $\mathrm{N_2} + 6\mathrm{H^+} + 6e^- \rightarrow 2\mathrm{NH_3}$,

$$E^0_{\mathrm{NRR}} = -\frac{\Delta G^0_{\mathrm{rxn}}}{6F} \approx +0.057\ \mathrm{V\ vs\ RHE}, \qquad E^0_{\mathrm{HER}} = 0\ \mathrm{V\ vs\ RHE}. \tag{2.15}$$

E^0_{NRR} is derived for gaseous ammonia from $\Delta G^0_f = -16.4\ \mathrm{kJ\,mol^{-1}}$ [12].
The small 57 mV separation shows that thermodynamics alone cannot explain selectivity between NRR and HER. Their competition must therefore be described through kinetic, surface-coverage and mass-transport effects [77].

Step 2: HER partial current (D/A)
All cathodic currents are expressed as positive magnitudes. The HER partial current is represented by the Tafel relation

$$j_{\mathrm{HER}}(E) = j_{\mathrm{HER,ref}} 10^{(E_{\mathrm{ref}} - E)/b_{\mathrm{HER}}}, \tag{2.16}$$

where E_{ref} is the common calibration potential and $j_{\mathrm{HER,ref}}$ is the HER partial current at that potential. The reference current is derived from the same Ru/C operating point used to calibrate the NRR current [35]:

$$j_{\mathrm{HER,ref}} = (1 - FE_{\mathrm{ref}})\, j_{\mathrm{tot,ref}}. \tag{2.17}$$

Using one calibration point for both partial currents ensures that the model reproduces the measured total current and Faradaic efficiency without combining different electrode systems.
Hu et al. do not report an isolated HER Tafel slope under the selected Ru/C–$\mathrm{LiClO_4}$ conditions. A literature-based value of $b_{\mathrm{HER}} = 0.120\ \mathrm{V\,dec^{-1}}$ is therefore used, corresponding to idealised Volmer-controlled HER. Lower slopes of 0.030 and $0.060\ \mathrm{V\,dec^{-1}}$, associated with Tafel- and Heyrovsky-controlled behaviour, are evaluated as well. These values are idealised and do not prove a particular rate-determining step [15].

Step 3: NRR kinetics and H-coverage suppression (A)
The intrinsic NRR rate is an effective Tafel expression (not a validated universal law) motivated by the potential-dependent activation barriers of [14, 55]:

$$j_{\mathrm{NRR,kin}}(E) = j^{\mathrm{kin}}_{\mathrm{NRR,ref}}\, 10^{(E_{\mathrm{ref}} - E)/b_{\mathrm{NRR}}}. \tag{2.18}$$

Here, b_{NRR} is an effective Tafel slope determined by fitting the complete NRR model to the measured current–potential series. The intrinsic reference current $j^{\mathrm{kin}}_{\mathrm{NRR,ref}}$ is subsequently back-calculated from the observed NRR current at E_{ref}, after accounting for hydrogen coverage and nitrogen transport, as described in the calibration subsection below.
Hydrogen adsorption on the catalyst surface is represented by a suppression factor, accounting for the blocking of active sites that would otherwise be available for nitrogen adsorption and reduction:

$$f_{\mathrm{cov}}(E) = \frac{1}{1 + \exp[(E_{\mathrm{cross}} - E)/w_{\mathrm{cov}}]}, \qquad j_{\mathrm{NRR,surf}} = j_{\mathrm{NRR,kin}}\, f_{\mathrm{cov}}, \tag{2.19}$$

where E_{cross} denotes the midpoint of the H-coverage transition and w_{cov} determines how sharply NRR is suppressed as the potential becomes more negative. This sigmoidal factor provides a reduced-order representation of the coverage-crossover mechanism described by Choi [14], capturing the decline in

NRR current at sufficiently negative potentials. Since neither parameter is reported directly, E_{cross} and w_{cov} are fitted to the measured position and width of the activity maximum.

The physical basis for this term is that nitrogen and hydrogen compete for the same surface sites, and that hydrogen coverage increases as the cathode potential becomes more negative, progressively blocking sites for nitrogen adsorption [14]. Adsorption-energy scaling relations link the binding strengths of nitrogen and hydrogen intermediates on transition-metal surfaces, making it difficult to improve nitrogen adsorption without also increasing hydrogen adsorption [58]. The sigmoid describes the resulting suppression without resolving which adsorbate or elementary step sets the crossover.

Step 4: Nitrogen transport limit (A/D)

The transport-limited current is

$$j_{\mathrm{lim,N_2}} = \frac{6FD_{\mathrm{N_2}}C_{\mathrm{N_2,b}}}{\delta}, \tag{2.20}$$

with $D_{\mathrm{N_2}} \approx 1.9 \times 10^{-5}$ cm^2 s^{-1} [23] and $C_{\mathrm{N_2,b}} \approx 0.64$ mM at 298 K, 1 bar [75] (both fixed); the boundary layer δ is the main uncertainty and is varied as a scenario.

Surface kinetics and transport combine reciprocally,

$$j_{\mathrm{NRR}}(E) = \frac{j_{\mathrm{NRR,surf}}(E)\, j_{\mathrm{lim,N_2}}}{j_{\mathrm{NRR,surf}}(E) + j_{\mathrm{lim,N_2}}}, \tag{2.21}$$

so the smaller of the two limits controls.

With representative parameters $j_{\mathrm{lim,N_2}} \approx 0.5$–$1.4$ mA cm^{-2}, whereas the calibrated j_{NRR} is of order μA cm^{-2}: at 1 bar the system is site-limited, not transport-limited.

This is a model result rather than an assumption: It implies that pressure or gas-diffusion electrodes only help after surface activity and selectivity improve [50].

Calibration

All reference quantities are determined once from a validated operating point reported by Hu et al. [35]. The measured ammonia-production rate and Faradaic efficiency are used to calculate the observed NRR partial current density and total current density:

$$j^{\mathrm{obs}}_{\mathrm{NRR,ref}} = \frac{3F\dot{n}_{\mathrm{NH_3,ref}}}{A}, \qquad j_{\mathrm{tot,ref}} = \frac{j^{\mathrm{obs}}_{\mathrm{NRR,ref}}}{FE_{\mathrm{ref}}}. \tag{2.22}$$

assuming NRR and HER are the only faradaic processes at this point.

The intrinsic prefactor is then obtained by inverting Eqs. (2.19) and (2.21) at E_{ref}:

$$j^{\mathrm{kin}}_{\mathrm{NRR,ref}} = \frac{j^{\mathrm{obs}}_{\mathrm{NRR,ref}}}{f_{\mathrm{cov}}(E_{\mathrm{ref}})\left(1 - j^{\mathrm{obs}}_{\mathrm{NRR,ref}}/j_{\mathrm{lim,N_2}}\right)} \simeq \frac{j^{\mathrm{obs}}_{\mathrm{NRR,ref}}}{f_{\mathrm{cov}}(E_{\mathrm{ref}})}, \tag{2.23}$$

Because the observed NRR current at the reference potential is much smaller than the nitrogen transport limit, the transport correction is small. The shape of the NRR current–potential curve is fitted using b_{NRR}, E_{cross} and w_{cov}. For each candidate set of these parameters, the intrinsic reference current $j^{\mathrm{kin}}_{\mathrm{NRR,ref}}$ is calculated such that the model reproduces the measured current at E_{ref}. The remaining measured operating points are then used to select the parameter set that best reproduces the complete activity curve. Because the reference potential corresponds to the measured activity maximum, a zero-slope constraint is imposed at this point, leaving two independent fitting degrees of freedom for the three shape parameters.

Step 5: Total current and selectivity (D)

$$j_{\mathrm{tot}}(E) = j_{\mathrm{NRR}}(E) + j_{\mathrm{HER}}(E), \qquad FE_{\mathrm{NH_3}}(E) = \frac{j_{\mathrm{NRR}}(E)}{j_{\mathrm{tot}}(E)}. \tag{2.24}$$

FE is thus an output of two independently computed partial currents. The selectivity optimum arises from the competition between the NRR and HER terms: NRR activity rises first, after which HER and hydrogen coverage dominate at more negative potential.

Step 6: Full-cell voltage and energy (A/D)
The anode is evaluated at the total current, $E_{\mathrm{a}} = E_{\mathrm{OER,eq}} + \eta_{\mathrm{a}}(j_{\mathrm{tot}})$, and since E is already the cathode potential,

$$V_{\mathrm{cell}}(E) = E_{\mathrm{a}}(j_{\mathrm{tot}}) - E + j_{\mathrm{tot}}\, ASR, \tag{2.25}$$

with ASR the total area-specific resistance. Further, $E_{\mathrm{OER,eq}} = 1.229$ V versus RHE is the oxygen-evolution equilibrium potential and η_{a} is the OER Tafel overpotential for the selected catalyst.
Production rate and specific consumption follow as $\dot{n}_{\mathrm{NH_3}}/A = j_{\mathrm{NRR}}/3F$ and

$$SEC_{\mathrm{NH_3}}(E) = \frac{4.72\, V_{\mathrm{cell}}(E)}{F E_{\mathrm{NH_3}}(E)} \quad [\mathrm{kWh\,kg^{-1}_{NH_3}}]. \tag{2.26}$$

Performance-gap analysis
Each parameter affects a different aspect of the modelled cell performance. The parameters $j^{\mathrm{kin}}_{\mathrm{NRR,ref}}$ and b_{NRR} describe the intrinsic NRR activity, while E_{cross} and w_{cov} determine the suppression caused by hydrogen coverage. The parameters $j_{\mathrm{HER,ref}}$ and b_{HER} describe the competing HER, and $j_{\mathrm{lim,N_2}}$ represents nitrogen transport. The area-specific resistance and anodic overpotential contribute to the full-cell voltage.

The influence of these parameters is evaluated through their effect on the ammonia partial current density, Faradaic efficiency and full-cell voltage. These cell-level outputs are subsequently translated into specific electricity consumption and required electrode area in Section 3.7. The pseudocode of the aqueous NRR model is provided in Appendix C.3.

2.6.2. Li-mediated NRR: a current-driven model

The lithium-mediated route uses the same thermodynamic, full-cell and energy framework as the aqueous model, but the cathode is represented differently. In aqueous NRR, the cathode potential is varied and separate NRR and HER partial currents are calculated. In Li-mediated NRR, the desired cathodic charge-transfer reaction is lithium plating,

$$\mathrm{Li^+ + e^- \rightarrow Li^0}, \tag{2.27}$$

after which nitrogen is converted through lithium- and solid-electrolyte-interphase-mediated steps. Competing reactions, including proton reduction, electrolyte decomposition and SEI formation, may also consume part of the applied current.
Li-mediated NRR is therefore modelled under galvanostatic operation, with applied current density j as the principal independent variable. The current density directly determines the rate at which lithium is deposited, while the cathode potential remains close to the lithium-plating potential over the investigated current range [86, 49]. The cell voltage required to sustain the selected current is subsequently calculated from the cathode, anode and resistive voltage contributions.

Shared framework and voltage penalty
Both routes are evaluated using the same system-level quantities: ammonia current, Faradaic efficiency, full-cell voltage and specific electricity consumption. This allows direct comparison with aqueous NRR and the Haber–Bosch benchmark.
The main difference is the cathode potential. Lithium deposition requires a substantially more negative potential than the aqueous NRR equilibrium potential of $E^0_{\mathrm{NRR}} = +0.057$ V versus RHE. Westhead et al. report a lithium-plating potential of approximately -3.40 ± 0.07 V versus RHE [95]. Relative to the aqueous NRR equilibrium potential, this corresponds to a voltage penalty of approximately

$$\left|E_{\mathrm{plate}} - E^0_{\mathrm{NRR}}\right| \approx 3.46\ \mathrm{V}. \tag{2.28}$$

Lithium deposition remains the dominant cathodic voltage contribution, even with potential improvements in electrolyte and SEI engineering.

Current-driven cathode

The applied current first drives lithium deposition, after which the deposited lithium reacts through chemical and interphase-mediated steps. The lithium supply rate is therefore proportional to the applied current:

$$r_{\mathrm{Li}} = \frac{j}{F}. \tag{2.29}$$

The cathode potential is approximated as

$$E_{\mathrm{c}}(j) \approx E_{\mathrm{plate}}. \tag{2.30}$$

The approximation neglects variations in cathode potential with current density, electrolyte composition and SEI resistance, which are assumed to be small relative to the approximately 3.4 V lithium-plating potential across the current densities evaluated in the model.

At low current density, increasing j generally increases ammonia production because more reactive lithium is supplied. At higher current density, nitrogen transport, proton-donor supply, SEI transport and side reactions can become limiting. Additional current then contributes increasingly to excess lithium deposition or parasitic reactions rather than ammonia formation [49, 44].

Selectivity from an experimental current sweep

Because no direct electrochemical NRR branch is calculated, the ammonia-equivalent current is obtained by partitioning the applied current:

$$j_{\mathrm{NH_3,eq}}(j) = FE_{\mathrm{NH_3}}(j)\, j. \tag{2.31}$$

Here, $j_{\mathrm{NH_3,eq}}$ represents the ammonia-producing fraction of the applied current.
The Faradaic efficiency $FE_{\mathrm{NH_3}}(j)$ follows the functional form proposed by Lazouski et al. [49], with its parameters calibrated to their reported efficiency maximum. Their controlled current-density sweep provides a consistent basis for modelling the dependence of Faradaic efficiency on operating conditions. The voltage contributions are obtained from complementary studies [95, 25], as no single dataset provides both a current sweep and a complete voltage breakdown. The resulting model combines measurements from different Li-mediated systems and should be interpreted as indicative of their performance limitations.

Developing a mechanistic FE model is outside the scope of this thesis. Faradaic efficiency results from the coupled effects of lithium deposition, SEI formation and transport, nitrogen and proton-donor mass transfer, and competing reactions. Predicting these processes would require a detailed, time-dependent electrochemical and transport model with system-specific parameters that are not consistently available. The resulting $FE_{\mathrm{NH_3}}(j)$ relation is therefore treated as specific to the selected Lazouski system and is not assumed to be universally transferable to other Li-mediated cell configurations.

Full-cell voltage

Because the catholyte is non-aqueous, water oxidation cannot proceed at this anode. The anode is therefore modelled as hydrogen oxidation (HOR), $\mathrm{H_2} \rightarrow 2\mathrm{H^+} + 2e^-$, as used in continuous-flow Li-mediated cells, where it also supplies protons to the catholyte [25]. Since HOR defines the RHE scale, its equilibrium potential is zero by construction and the anode term is entirely overpotential, $E_{\mathrm{a}}(j) = \eta_{\mathrm{a}}(j)$.
The anode overpotential follows the same Tafel form as the aqueous model, calibrated at a reference current density.

$$\eta_{\mathrm{a}}(j) = \eta_{\mathrm{a,ref}} + b_{\mathrm{a}} \log_{10}\left(\frac{j}{j_{\mathrm{ref}}}\right), \tag{2.32}$$

where b_{a} is the HOR Tafel slope. HOR is sluggish in Li-salt/ether electrolytes, with Pt deactivating and stable operation requiring alloyed anodes such as Pt–Au [25]. As no consistent Tafel parameters exist for these media, both $\eta_{\mathrm{a,ref}}$ and b_{a} are assumed terms (A) and are varied in the sensitivity analysis, with a base case of 0.4 V at the reference current density [95]. The current-dependent formulation accounts for the increase in anode overpotential at higher current densities, resulting in a more realistic cell voltage estimate.
The full-cell voltage is then

$$V_{\mathrm{cell}}(j) = \eta_{\mathrm{a}}(j) - E_{\mathrm{plate}} + j\,ASR_{\mathrm{eff}}, \tag{2.33}$$

with ASR_{eff} the SEI-related resistance. E_{plate} is taken as the plating onset, and ASR_{eff} is obtained by dividing the iR-corrected potential rise beyond this onset by the applied current density [95]. Because these potentials are iR-corrected, the electrolyte resistance is not included, which underestimates the cell voltage. At the same time, ASR_{eff} was measured in a low-current cell, and extrapolating it linearly to higher current densities overestimates the voltage. The two effects act in opposite directions, so the net error is uncertain.

Production and energy consumption

The ammonia production rate per electrode area is

$$\frac{\dot{n}_{\mathrm{NH_3}}}{A} = \frac{F E_{\mathrm{NH_3}}(j)\, j}{3F}. \tag{2.34}$$

The specific electricity consumption is calculated using the same relation as for aqueous NRR:

$$SEC_{\mathrm{NH_3}}(j) = \frac{4.72\, V_{\mathrm{cell}}(j)}{F E_{\mathrm{NH_3}}(j)} \quad \left[\mathrm{kWh\,kg^{-1}_{NH_3}}\right]. \tag{2.35}$$

This covers the cell only; the energy required to supply hydrogen or ethanol (as proton donor) to the anode is accounted for in Section 3.7.

Difference from aqueous NRR

The model evaluates whether improvements in Faradaic efficiency, productive current density, resistance and anode performance can compensate for the voltage penalty associated with lithium plating. The pseudocode is provided in Appendix C.4.

2.6.3. Water-fed membrane Li-mediated NRR

The water-fed configuration retains the galvanostatic Li-mediated framework described in Section 2.6.2, using a different proton supply mechanism. An electrically isolated palladium membrane separates the aqueous water-oxidation anode from the non-aqueous Li-plating catholyte and transfers hydrogen species while suppressing direct water crossover [97]. The applied current density remains the principal independent variable, while lithium plating remains the desired cathodic charge-transfer step.
The membrane-based proton supply changes the cathode environment, potentially affecting SEI properties and reaction selectivity. The model uses the Faradaic efficiency and cell voltage measured for the water-fed configuration to account for these differences.

Current-dependent voltage and energy consumption

The reported voltage contributions correspond to the measured operating point and are not assumed constant with current density. The anode potential is described using the same Tafel form as the oxygen-evolution anode of the aqueous model, with the Tafel slope fitted to the measured anode potential of 2.21 V versus RHE at $6\ \mathrm{mA\,cm^{-2}}$ (≈ 0.21 V dec^{-1}), while membrane and resistive losses are represented as current-dependent terms. The full-cell voltage is written as

$$V_{\mathrm{cell}}(j) = \Delta V_{\mathrm{plate}} + \eta_{\mathrm{mem}}(j) + E_{\mathrm{a}}(j) + |j|\, ASR_{\mathrm{cell}}, \tag{2.36}$$

where $\Delta V_{\mathrm{plate}}$ is the positive voltage contribution associated with lithium plating, η_{mem} is the membrane transport loss, and ASR_{cell} represents the remaining resistive losses in the cell.

At the reference current-density magnitude of $6\ \mathrm{mA\,cm^{-2}}$, the reported membrane and resistive contributions are approximately 0.5 and 1.0 V, respectively [97]. Because no complete steady-state membrane polarisation curve is available, the membrane loss is approximated as scaling linearly with current density:

$$\eta_{\mathrm{mem}}(j) = \eta_{\mathrm{mem,ref}} \frac{|j|}{|j_{\mathrm{ref}}|}. \tag{2.37}$$

This corresponds to an apparent membrane area-specific resistance of approximately $83\ \Omega\,\mathrm{cm^2}$. The separate 1.0 V resistive contribution corresponds to an apparent cell resistance of approximately $167\ \Omega\,\mathrm{cm^2}$

at the reference current density. These values are inferred from the reported voltage contributions and serve as first-order engineering approximations.

A current-dependent Faradaic-efficiency relation cannot be derived for the water-fed configuration because the available study does not report a controlled current-density sweep. The reported $FE_{\mathrm{NH_3}} = 48 \pm 5\%$, excluding the prehydridation charge, therefore determines the ammonia production rate at the measured current density. Ye et al. operated the cell in pulses of 1 min on and 1 min off, so the time-averaged ammonia current density is half that during a pulse. Because the prehydridation charge is spent in every cycle, the specific electricity consumption is based on the cycle-level value of $36 \pm 4\%$, which includes it. The sensitivity analysis varies Faradaic efficiency independently of current density. The specific electricity consumption is calculated as

$$SEC_{\mathrm{NH_3}}(j, FE_{\mathrm{NH_3}}) = \frac{4.72\, V_{\mathrm{cell}}(j)}{FE_{\mathrm{NH_3}}} \quad \left[\mathrm{kWh\,kg^{-1}_{NH_3}}\right] \tag{2.38}$$

The measured voltage contributions at $|j_{\mathrm{ref}}| = 6\ \mathrm{mA\,cm^{-2}}$ are used to calibrate the membrane and resistive terms, so the model reproduces the measured cell voltage at this point by construction. The voltage at other current densities follows from the assumed linear scaling and is not independently validated.

The measured increase in membrane potential over time indicates short-term changes in membrane performance. Long-term degradation is not included because the available six-hour experiment is insufficient to establish transferable current- or time-dependent degradation relations. The model therefore captures the first-order influence of current density on membrane, anode and resistive losses, while FE and long-term degradation are treated through sensitivity analysis and model limitations. The pseudocode of the water-fed membrane Li-medated NRR model is provided in Appendix C.5.

2.7. Comparison framework NRR with Electrolyzer + HB

The reduced-order models of the preceding sections return, for each route, the full-cell voltage, the Faradaic efficiency and the total current density. This section sets out how those quantities are compared against the subsystems the cell is intended to replace, and how a route is carried from that comparison into a plant. The framework proceeds in four stages. The cells are first compared as cells, on a common boundary and independently of the plant around them. The gap between each cell and the reference is then decomposed into the terms that cause it, and each term classified by how tractable it is. A route is selected on the basis of that decomposition rather than on present performance alone. The selected route is finally examined in one additional configuration, in which the by-product hydrogen is collected and supplied to a Haber–Bosch loop, an arrangement the literature does not treat.

2.7.1. Cell-level comparison

Comparison boundary and functional unit

An electrochemical cell does not replace an ammonia plant; it replaces the conversion block that turns electricity and feedstock into ammonia, comprising the electrolyser, the hydrogen buffer and the Haber–Bosch synthesis loop. The PV field, wind capacity, the battery, the water supply and the nitrogen generator are required by both routes and are excluded, since retaining them would add the same quantity to each side and obscure the difference the comparison is intended to expose. The functional unit is one kilogram of ammonia delivered from this conversion block.

One route-specific asymmetry is carried explicitly. The direct routes generate protons from water and replace the electrolyser entirely, whereas a lithium-mediated cell with a hydrogen-oxidation anode still depends on an external proton source. This additional requirement is accounted for by including either the electricity demand of hydrogen production by electrolysis or the external ethanol supply, depending on the configuration considered. Other route-specific requirements, including electrolyte recovery, circulation and thermal management, are not included quantitatively at this stage, since the available data do not support defensible fixed values. Faradaic efficiency is evaluated toward ammonia throughout this stage, with the efficiency toward hydrogen recorded separately as a cell property whose value to the plant is examined in Section 2.7.4.

Energy comparison

The electrochemical routes are compared with the electricity consumption of the conversion block they would replace, consisting of the electrolyser and the Haber–Bosch synthesis loop,

$$SEC_{\mathrm{ref}} = SEC_{\mathrm{el}} + SEC_{\mathrm{HB}}, \tag{2.39}$$

where SEC_{el} is the electrolyser consumption and SEC_{HB} that of the synthesis loop, both expressed per kilogram of ammonia. Both terms are calculated from thermodynamic relations, as shown in Figure B.1. For comparison, the reversible cell potential (of direct synthesis) of 1.17 V sets a theoretical minimum of roughly 5.5 kWh $\mathrm{kg}_{\mathrm{NH_3}}^{-1}$ [80].
For the electrochemical routes the corresponding quantity follows directly from the cell model,

$$SEC_{\mathrm{NRR}} = \frac{4.72\, V_{\mathrm{cell}}}{FE_{\mathrm{NH_3}}} \qquad \left[\mathrm{kWh\,kg}_{\mathrm{NH_3}}^{-1}\right], \tag{2.40}$$

in which the constant collects $3F/M_{\mathrm{NH_3}}$ and the conversion to kilowatt-hours. Equation (2.40) gives the cell energy consumption, although current density enters only indirectly through its effect on cell voltage and Faradaic efficiency.
Requiring $SEC_{\mathrm{NRR}} \leq SEC_{\mathrm{ref}}$ gives the condition for energy parity,

$$V_{\mathrm{cell}} \;\leq\; \frac{SEC_{\mathrm{ref}}}{4.72}\, FE_{\mathrm{NH_3}}, \tag{2.41}$$

which defines a straight locus in the $(FE_{\mathrm{NH_3}}, V_{\mathrm{cell}})$ plane rather than a single threshold. Plotting the modelled operating point of each route against this line shows directly how much the cell voltage would have to fall, or the Faradaic efficiency rise, for the route to match the reference. Because the cell voltage cannot fall below the reversible potential, Eq. (2.41) also implies a minimum Faradaic efficiency of $4.72\, E_{\mathrm{cell,min}}/SEC_{\mathrm{ref}}$, below which parity is unattainable at any overpotential.

Productive current density and electrode area

Only the fraction of the applied current that produces ammonia contributes to the productive current density,

$$j_{\mathrm{NH_3}} = \mathrm{FE}_{\mathrm{NH_3}} j_{\mathrm{tot}}. \tag{2.42}$$

Current density determines the active electrode area required for a given production rate. The NRR routes are therefore compared with the alkaline electrolyser on an equal-active-area basis. Producing the hydrogen required for one mole of ammonia requires the same $3F$ of useful charge as direct electrochemical ammonia formation. The ammonia-equivalent productive current density of the reference electrolyser is

$$j_{\mathrm{NH_3,ref}} = \mathrm{FE}_{\mathrm{H_2}} j_{\mathrm{el}}. \tag{2.43}$$

Conventional alkaline electrolysers operate at current densities of 0.2–$0.7\ \mathrm{A\,cm^{-2}}$ [71]; a representative value of $j_{\mathrm{el}} = 0.4\ \mathrm{A\,cm^{-2}}$ is adopted [2]. With $\mathrm{FE}_{\mathrm{H_2}} \approx 1$, this gives

$$j_{\mathrm{NH_3,ref}} \approx 400\ \mathrm{mA\,cm^{-2}}. \tag{2.44}$$

At the 300 t NH_3/yr reference production rate the required charge follows from Faraday's law. Since ammonia formation consumes three electrons per molecule, the continuous current equivalent to an ammonia mass flow $\dot{m}_{\mathrm{NH_3}}$ is

$$I = \frac{3F\,\dot{m}_{\mathrm{NH_3}}}{M_{\mathrm{NH_3}}}, \tag{2.45}$$

where $F = 96\,485$ C mol^{-1} and $M_{\mathrm{NH_3}} = 17.031$ g mol^{-1}. At 300 t/yr of continuous operation, $\dot{m}_{\mathrm{NH_3}} = 34.25$ kg h^{-1} and Eq. (2.45) gives $I \approx 162$ kA. The corresponding active area follows from the productive current density,

$$A = \frac{I}{j_{\mathrm{NH_3}}} = \frac{3F\,\dot{m}_{\mathrm{NH_3}}}{M_{\mathrm{NH_3}}\, j_{\mathrm{NH_3}}}, \tag{2.46}$$

so at $j_{\mathrm{el}} = 0.4$ A cm^{-2} the reference electrolyser requires about 40 m^2. Continuous operation is assumed for both routes, so the area ratio is unaffected.
The relative active electrode area required by an NRR cell to achieve the same ammonia production rate is then

$$\frac{A_{\mathrm{NRR}}}{A_{\mathrm{ref}}} = \frac{j_{\mathrm{NH_3,ref}}}{j_{\mathrm{NH_3}}}. \tag{2.47}$$

Equal active area does not imply equal stack cost, since electrode materials and cell construction differ between technologies. The area ratio is used as an indicator of area productivity rather than as a direct cost comparison.

Comparison outputs

For each route the comparison reports the four quantities listed in Table 2.3. The first two ask whether a cell is energetically competitive with the block it replaces, the last two whether it is productive enough to be built at a sensible size, and each pair is expressed as a distance from the base case rather than as an absolute figure.

Table 2.3: Outputs of the cell-level comparison with the reference conversion block.

Output	Indicates
SEC_{NRR}	electricity per kilogram of ammonia, against SEC_{ref}
Required $FE_{\mathrm{NH_3}}$, V_{cell}	the combinations satisfying Eq. (2.41), and the distance of the modelled point from that locus
$j_{\mathrm{NH_3}}$	productive current density, the rate at which a unit of electrode makes ammonia
$j_{\mathrm{NH_3}}/j_{\mathrm{NH_3,req}}$	area productivity against the electrolyser of the base case, delivering the same output from the same electrode area

2.7.2. Analysis of the performance gap

The outputs of Section 2.7.1 quantify the performance gap between each NRR route and the Haber–Bosch benchmark. Understanding the underlying limitations helps assess how realistically these gaps can be reduced. The analysis links the route-specific limitations in Table 1.1 to the parameters of the corresponding cell models.

Each limitation affects one or more performance indicators. Anodic, cathodic and ohmic losses increase the full-cell voltage and specific energy consumption. Competing hydrogen evolution and side reactions associated with lithium plating and interphase formation reduce the Faradaic efficiency towards ammonia. Limited nitrogen availability, active-site blocking and mass-transfer constraints reduce productive current density and increase the required electrode area. Product dilution, electrolyte recovery and membrane limitations introduce additional challenges related to separation, durability and practical operation.

The mitigation measures in Table 1.1 are classified by the development required. Cell geometry, electrolyte conductivity, separator thickness, gas-diffusion electrodes and process configuration are primarily engineering challenges. Improvements in catalyst activity, selectivity, mediator chemistry and reaction mechanisms require further materials and electrochemical development. The potential for improvement is assessed using progress reported across the literature.

The analysis carries uncertainty because most cell parameters are derived from laboratory-scale experiments of limited duration. Lifetime degradation is assessed qualitatively, and additional process requirements with insufficient data are considered when evaluating the selected route in the hybrid configuration.

2.7.3. Selection of the cell route

A single route is carried forward. The selection is not based on present numerical performance alone, since the comparison is also intended to identify the improvements required for each route. The magnitude of the performance gap is therefore considered together with its origin, as established in Section 2.7.2. A larger gap concentrated in limitations that can realistically be addressed through engineer-

ing may be more promising than a smaller gap that depends on fundamental changes in selectivity or reaction mechanism.

The selection also considers expected durability, prospects for scale-up, separation and operating requirements, and compatibility with an autonomous plant supplied by intermittent renewable electricity. The latter includes the cell's expected tolerance to shutdown, restart and part-load operation. These considerations correspond to the criteria introduced in Section 2.1.1, but are applied here alongside the quantitative cell-performance assessment. The reasoning behind the selection is documented explicitly so that the influence of each consideration remains visible.

2.7.4. Configuration and assessment of the selected route

The preceding comparison considers direct electrochemical ammonia synthesis, where by-product hydrogen is not utilised. As an additional configuration, a hybrid arrangement is examined in which this hydrogen is supplied to a Haber–Bosch loop (Figure 2.7). This could improve the overall efficiency of routes with low ammonia Faradaic efficiency, as hydrogen produced through competing reactions is recovered rather than discarded. The benefit does not apply to Li-mediated NRR with a hydrogen-oxidation anode, where hydrogen is already supplied as a reactant.



(a) Direct electrochemical ammonia synthesis

(b) Hybrid configuration in which by-product hydrogen is supplied to a Haber–Bosch loop

Figure 2.7: Possible plant configurations for integrating the electrochemical nitrogen reduction cell

The hybrid configuration is assessed using the same cell-performance indicators as Section 2.7.1, accounting for the additional ammonia produced from recovered hydrogen and the corresponding Haber–Bosch energy consumption. The full cell voltage remains applicable to all current. Additional hydrogen drying, compression and integration losses are excluded. The results provide an indicative performance comparison rather than a complete plant-level or economic assessment.

2.8. Sensitivity and uncertainty analysis

Sensitivity analysis is used to assess how strongly the optimisation results and NRR comparison depend on uncertain model assumptions. For the Haber–Bosch plant, the analysis considers cost uncertainty, component sizing, location and renewable-resource variability.

Cost uncertainty is assessed through the probabilistic LCOA analysis described earlier, while Spearman rank correlations identify the most influential cost parameters. In addition, alternative cost assumptions from Wang et al. [94] and FESM are used to re-cost and re-optimise the plant, assessing whether the preferred configuration changes. The influence of equipment cost scaling is also tested by applying a scaling exponent of 0.65 to the non-modular components.

Sensitivity around the optimised configuration is evaluated by varying the PV, wind, battery, electrolyser, hydrogen-buffer and Haber–Bosch capacities individually while keeping the remaining capacities fixed. The resulting changes in production, feasibility and contracted LCOA show which components are most important for meeting the monthly production requirement and how sensitive the optimum is to capacity changes.

Location sensitivity is assessed by repeating the optimisation for Geraldton, NEOM and Lüderitz using identical cost assumptions and operating constraints. This allows the influence of local solar and wind profiles on plant sizing, production and cost to be evaluated.

For the NRR routes, uncertainty is evaluated at cell level rather than through a full plant cost model. Uncertain kinetic, transport and voltage parameters are varied within the ranges supported by the reduced-order models, together with reported Faradaic-efficiency scenarios. Their influence on cell voltage, Faradaic efficiency, productive current density, specific electricity consumption and required electrode area is used to assess the robustness of the comparison with the Haber–Bosch reference.

3

Results

Firstly, suitable technologies are selected for the individual plant subprocesses. The energy and mass balances are then established, followed by preliminary sizing using FESM. Next, the autonomous Haber–Bosch plant is simulated and optimised to reduce production costs. Its ability to operate independently under varying renewable conditions is then assessed. Finally, the performance of electrochemical NRR routes is compared with the Haber–Bosch benchmark.

The chapter is organised as follows. Section 3.1 presents the MCDA results, followed by the plant-level energy and mass balances in Section 3.2. Section 3.3 presents the FESM results, while Section 3.4 evaluates the Haber–Bosch base case. Section 3.5 presents the optimised plant configuration and its economic performance, followed by the autonomy assessment in Section 3.6. Finally, Section 3.7 presents the electrochemical NRR results and compares their performance with the Haber–Bosch benchmark.

3.1. MCDA results

Each plant subsystem is assigned a technology selected from a set of candidates. The synthesis route is fixed as electrolysis followed by Haber–Bosch, while the power supply, battery storage, nitrogen supply, water supply and type of electrolyser are selected through the MCDA. All candidates are introduced in Chapter 1, including their operating principles, characteristics and supporting literature. This section focuses on the properties relevant to their comparison.

The same criteria and weights from Section 2.1.1 are applied to all subsystems. Weights and scores range from 1 to 3, with higher scores indicating more favourable performance. The weights sum to 20, giving a maximum attainable score of 60. Energy consumption and costs can be assessed using quantitative data, while autonomy, robustness, modularity and operating conditions require qualitative judgement. The resulting scores provide an indication of the relative suitability of each technology. When candidates achieve similar scores, the final selection is supported by a more detailed assessment of the specific plant requirements.

3.1.1. Power supply

Geothermal, biomass and hydropower are excluded, since each ties the plant to a particular geology, fuel supply chain or water course. Wind is interpreted as onshore wind, since offshore wind would require marine infrastructure and large costs.

For power-supply technologies, the Energy criterion is interpreted as electricity availability and complementarity rather than specific energy consumption.

Table 3.1: Weighted scores for the power supply

		Score		
Criterion	Weight	Solar PV	Wind	Hybrid PV–wind
Autonomy	3	3	2	2
Costs	3	3	1	2
Energy	3	1	1	3
Intermittent compatibility	2	1	2	3
Modularity	1	3	1	2
Operational conditions	2	3	2	2
Robustness	3	3	2	3
Scalability	1	3	1	2
Technology readiness level	2	3	3	3
Weighted total		50	34	50

Solar PV and the hybrid PV–wind system both reach 50 out of 60, while wind alone scores 34 (Table 3.1). The equal scores reflect different advantages. Solar PV performs better on autonomy, modularity and operational simplicity because it has no moving parts and can be installed in small increments. The hybrid system performs better on energy availability and intermittent compatibility, since wind can supply electricity during periods of low or zero solar generation and thereby reduce the residual power gap that must be covered by storage.

Wind alone is less suitable at the small scale considered here, because turbine capacity is added in relatively large increments and introduces additional mechanical maintenance requirements. Solar PV is therefore used in the base case as the simpler autonomous reference configuration. The cost scores in Table 3.1 reflect component costs only and do not capture the storage that wind may avoid at system level. The hybrid PV–wind option is therefore retained in the configuration optimisation of Section 3.5, where the trade-off between wind capacity and storage requirements is evaluated explicitly.

3.1.2. Battery storage

The absence of solar generation at night makes energy storage important for maintaining operation during periods without renewable electricity. Three battery technologies are compared: lithium iron phosphate, the vanadium redox flow battery and lead–acid.

Table 3.2: Weighted scores for the battery

		Score		
Criterion	Weight	Lithium iron phosphate	Vanadium flow	Lead–acid
Autonomy	3	3	2	2
Costs	3	1	1	3
Energy	3	3	1	2
Intermittent compatibility	2	3	3	1
Modularity	1	3	2	2
Operational conditions	2	2	2	1
Robustness	3	2	3	1
Scalability	1	3	3	2
Technology readiness level	2	3	2	3
Weighted total		49	40	38

Lithium iron phosphate reaches 49 out of 60, compared with 40 for the vanadium redox flow battery and 38 for lead–acid (Table 3.2). This result is consistent with most of the reviewed literature, in which lithium-ion batteries, and particularly LFP, are generally identified as the preferred option for stationary renewable-energy storage due to their combination of high efficiency, maturity and modularity.

Lead–acid remains a mature technology but is less suited to the present duty. Its lower usable depth of discharge and shorter cycle life under frequent deep cycling result in a larger required capacity and more frequent replacement, which is undesirable for an autonomous plant.

Vanadium redox flow batteries provide a more competitive alternative, particularly for long-duration storage. Their high cycle durability and independent sizing of power and energy are advantageous for daily overnight storage. However, their higher capital cost, lower round-trip efficiency and additional balance-of-plant equipment, such as pumps, tanks and piping, reduce their attractiveness for an unattended system. The lower efficiency is particularly relevant off-grid, as storage losses must ultimately be compensated by additional renewable generation.

Taken together, these considerations make lithium iron phosphate the preferred battery technology for this study.

3.1.3. Nitrogen supply

Nitrogen is separated from air on site to maintain full control over the plant feedstock. Pressure swing adsorption, membrane separation and cryogenic distillation are compared. At the small production scale considered here, throughput is not the main differentiator; instead, purity, cost, modularity and compatibility with variable operation are more important.

Table 3.3: Weighted scores for the nitrogen supply

		Score		
Criterion	Weight	Pressure swing adsorption	Membrane	Cryogenic
Autonomy	3	3	3	1
Costs	3	3	2	1
Energy	3	2	1	3
Intermittent compatibility	2	3	3	1
Modularity	1	3	3	1
Operational conditions	2	3	2	2
Robustness	3	2	1	3
Scalability	1	2	1	3
Technology readiness level	2	3	2	3
Weighted total		53	39	40

Pressure swing adsorption achieves the highest weighted score, with 53 out of 60, compared with 40 for cryogenic distillation and 39 for membrane separation (Table 3.3). Its main advantages are its relatively low cost, modularity and suitability for small-scale operation. It can also accommodate variable operation more readily than cryogenic separation, which is better suited to large, continuously operated plants.

Cryogenic distillation offers the highest nitrogen purity and favourable specific energy consumption at large scale, but its capital intensity, limited modularity and preference for continuous operation make it less suitable for the decentralised system considered here. Membrane separation is compact and modular, but reaching the required purity becomes increasingly demanding. Weighing these trade-offs, pressure swing adsorption is selected as the nitrogen-supply technology.

3.1.4. Water supply

Water demand is small relative to the other plant flows, at approximately 1.6 kg of water per kilogram of ammonia. Seawater reverse osmosis, atmospheric water harvesting and piped freshwater are compared.

Table 3.4: Weighted scores for the water supply

		Score		
Criterion	Weight	Seawater reverse osmosis	Atmospheric harvesting	Piped supply
Autonomy	3	1	3	1
Costs	3	2	2	1
Energy	3	3	1	3
Intermittent compatibility	2	2	3	3
Modularity	1	3	3	2
Operational conditions	2	1	3	3
Robustness	3	2	2	1
Scalability	1	3	1	2
Technology readiness level	2	3	2	3
Weighted total		42	44	40

Table 3.4 shows that Atmospheric water harvesting obtains the highest score because it is the most autonomous option and does not require access to a water network or coastline. Its main disadvantage is the higher energy demand and its dependence on local humidity. Sorbent-based systems have demonstrated water production at relative humidities of around 10%, but the yield decreases strongly as humidity falls. Local humidity therefore needs to be checked before deployment.

Atmospheric water harvesting is selected because it allows the plant to operate without any external water supply, in line with the autonomous plant concept. Its energy demand is included in the plant model, while its capital cost is assumed as negligible relative to the other components. Where local humidity is insufficient, seawater reverse osmosis offers a practical alternative at the coastal locations considered, so water supply is not expected to constrain the plant configuration.

3.1.5. Electrolyser selection

The electrolyser is the largest single consumer of power in the plant and the block that decides how closely production can follow a supply that changes through the day, so this selection carries further than the others. Three types are compared: Alkaline Water Electrolysis (AWE), proton exchange membrane (PEM) and Solid Oxide Electrolyser Cell (SOEC).

Table 3.5: Weighted scores for the electrolyser

		Score		
Criterion	Weight	AWE	PEM	SOEC
Autonomy	3	2	3	1
Costs	3	3	2	1
Energy	3	2	2	3
Intermittent compatibility	2	2	3	1
Modularity	1	2	3	2
Operational conditions	2	3	3	1
Robustness	3	3	2	1
Scalability	1	3	2	1
Technology readiness level	2	3	3	2
Weighted total		51	50	29

Table 3.5 shows that AWE and PEM electrolysis perform almost equally, with weighted scores of 51 and 50, respectively. Their energy consumption is also similar, at about 52-53 kWh/kg H_2, so both receive the same score on the highest-weighted energy criterion. The main differences are therefore flexibility

and cost. PEM offers faster start-up, a wider operating range and stronger part-load performance, whereas alkaline is more limited at low load because gas crossover through the diaphragm can become problematic. Alkaline, however, has lower capital cost, mature technology and long commercial stack lifetimes. Because the two technologies perform similarly overall, alkaline electrolysis is selected based on its lower cost and long operating history. This choice is also supported by the literature, where alkaline electrolysers are commonly used as the reference technology in green-ammonia and Power-to-X systems.

Solid oxide electrolysis offers the highest electrical efficiency, provided the heat it requires at 600–850 °C can be recovered from other processes rather than supplied electrically, which earns it the top score on energy. It scores lowest on almost every other criterion. Its stack lifetime is already much shorter than that of alkaline and PEM systems, and intermittent operation shortens it further, as load changes and start-stop cycles impose thermal stress on the ceramic and accelerate degradation. Avoiding this requires keeping the stack hot through every night, a thermal-management demand that conflicts with an unattended off-grid plant.

3.1.6. Resulting base-case plant

Table 3.6 collects the five selections. Together with the synthesis route fixed at the outset, they define the base case: a photovoltaic field with lithium iron phosphate (LFP) battery storage supplying an alkaline electrolyser, water from atmospheric water harvesting, nitrogen from a pressure swing adsorption unit, and a Haber–Bosch loop fed through a hydrogen buffer. This configuration is simulated in Section 3.4 and sized in Section 3.5, where wind capacity and ammonia storage are added.

Function	Selected technology	Score
Power supply	Solar photovoltaics	50
Energy storage	Lithium iron phosphate battery	49
Nitrogen supply	Pressure swing adsorption	53
Water supply	Atmospheric water harvesting	44
Hydrogen production	Alkaline electrolyser	51

Table 3.6: Subsystems selected through the multi-criteria analysis

The five subsystems are also compatible at their interfaces, which the table cannot show because each subsystem is scored on its own. The battery buffers electricity for all consuming units, water leaves the harvesting unit as a liquid at ambient temperature and feeds the electrolyser directly, and nitrogen and hydrogen leave their units as gases at ambient temperature and modest pressure. No unit in the front end therefore has to condition a stream for the next one. The step change comes at the synthesis loop, which requires its feed at high pressure and several hundred degrees. The compression and preheating between the front end and the reactor are therefore counted as part of the loop and priced accordingly in Section 2.4.2.

The analysis results in a relatively conservative plant configuration: all selected technologies are commercially available at this scale except for the water-harvesting unit and the small-scale, load-flexible Haber–Bosch loop. This follows from the high weighting of cost, robustness and technology readiness, which favour proven technologies with reliable performance and available cost data. The water unit is the main exception, but its contribution to total plant cost and energy demand is small, which makes the selected configuration a suitable basis for the subsequent techno-economic analysis.

3.2. Plant-level Energy and Mass Balance

3.2.1. Overview system flow

Ammonia synthesis requires nitrogen and hydrogen as molecular feedstock, both of which can be supplied on site from air and water. This makes the system relatively self-contained: air provides the nitrogen feed, while water electrolysis supplies the hydrogen required for synthesis. Water provides the hydrogen incorporated into ammonia, while the remaining oxygen is released as a by-product.

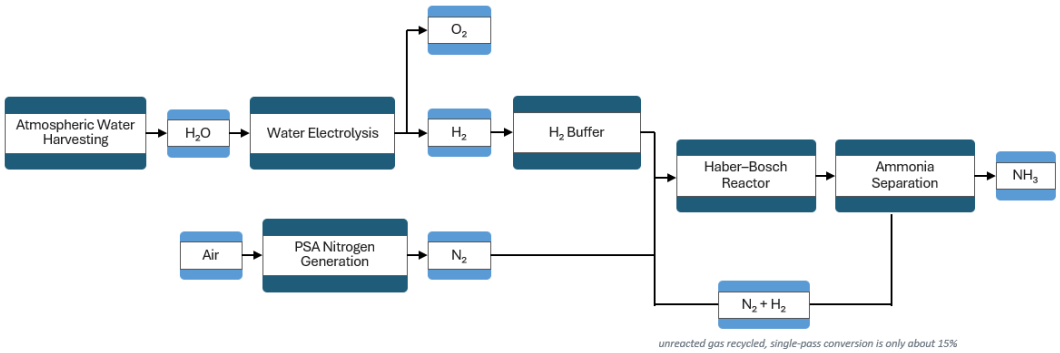

Figure 3.1: Simplified overview of the concept system balance

Figure 3.1 shows the route; the full balance, with stream conditions, block duties and the thermodynamic data behind them, is given in figure B.1 Appendix B. Water is drawn from ambient air by sorbent-based atmospheric harvesting and fed to the electrolyser delivering hydrogen at 30 bar, with oxygen vented. Nitrogen is separated from air by pressure swing adsorption at 99.99% purity, leaving the unit at 5 bar and compressed to 30 bar in two intercooled stages. The two streams are mixed at 30 bar in the stoichiometric ratio of three to one and then compressed together to the loop pressure of 300 bar in three stages. This simplifies the make-up gas train and avoids separate high-demanding hydrogen compression due to hydrogen's low density and high volumetric flow. The syngas is fed to the reactor, where heat released by the exothermic Haber–Bosch reaction raises the gas temperature to approximately 723 K. At a single-pass conversion of about 15%, the outlet stream leaves at 280 bar, after which ammonia is condensed and the unreacted nitrogen and hydrogen are recompressed and recycled to the loop

3.2.2. Mass balance

The mass balance converts the ammonia production target into the feedstock flows that each unit has to supply. Table 3.7 separates the flows fixed by stoichiometry from those that depend on equipment assumptions. The nitrogen and hydrogen demand follow directly from ammonia synthesis, while the water consumption and oxygen by-product follow from electrolysis-based hydrogen production. The air intake, in contrast, depends on the recovery and purity requirements of the nitrogen separation unit.

Table 3.7: Mass balance per kilogram of ammonia

Stream	kg/kg NH_3	Fixed by
Nitrogen to loop	0.822	NH_3 stoichiometry
Hydrogen to loop	0.178	NH_3 stoichiometry
Water, reacted	1.587	Electrolysis stoichiometry
Oxygen vented	1.409	Electrolysis stoichiometry
Air to PSA	1.81	60 % N_2 recovery

The stoichiometric flows are independent of the electrolyser type or synthesis loop design, provided hydrogen is produced from water electrolysis. The air demand is the main equipment-dependent material flow in this simplified balance: it increases when nitrogen recovery decreases or when higher purity requirements reduce PSA recovery. The loop is modelled with full recycle of unreacted nitrogen

and hydrogen, so no purge stream is included. Water polishing losses are neglected, meaning that the atmospheric water harvesting unit must deliver 1.587 kg of water per kilogram of ammonia.

3.2.3. Specific energy consumption

Specific energy demand defines how much renewable electricity the plant must supply per kilogram of ammonia and is therefore set before plant sizing. Table 3.8a compares, for each process step, the reversible minimum with the design demand of the selected equipment; the formulas and input parameters behind both columns are given in Table A.1 (Appendix A.1). Hydrogen production includes the electrolyser stack and auxiliaries, while nitrogen separation includes the feed-air compressor and PSA unit.

Table 3.8: Specific energy consumption by process step and procurement package.

(a) By process step

	kWh/kg NH_3			
Contribution	Rev.	Design	Excess	Share of excess (%)
Water harvesting	—	0.397	0.397	8.2
Electrolysis	5.801	9.710	3.899	80.6
Nitrogen separation	0.005	0.132	0.127	2.6
Nitrogen compression	0.041	0.059	0.018	0.4
Syngas compression	0.210	0.300	0.090	1.9
Feed preheat	—	0.301	0.301	6.2
Recycle compressor	0.005	0.007	0.002	$<$0.1
Total	6.063	10.896	4.834	100.0

(b) By procurement package

Package	kWh/kg NH_3	Share of design (%)
Water harvesting	0.397	3.8
Electrolysis	9.688	91.5
Nitrogen separation	0.132	1.2
Synthesis-loop compression	0.366	3.5
Total	10.583	100.0

The two totals differ because the heat required to bring the syngas to reactor temperature is supplied internally rather than by external electricity. The Haber–Bosch reactor releases 91.8 kW of heat, while the total heat demand to raise the syngas to 723 K is only 36.89 kW. This duty is therefore included in panel (a) as a real process duty, but excluded from panel (b) because it does not add to the external electricity demand used for plant sizing and costing.

The energy demand is dominated by the electrolyser, which accounts for 91.5% of the external electricity demand once feed preheat is supplied internally. This is mainly determined by the cell voltage, increasing from the reversible minimum of 1.23 V to an assumed practical operating voltage of 2.06 V. Consequently, improvements in electrolysis efficiency have the largest effect on the total energy demand, while the other process steps remain comparatively small.

3.2.4. Exergy

The exergy balance is used as a consistency check on the energy balance rather than as a component-level loss analysis. It compares the external electricity input against the chemical exergy stored in the product, and treats the remainder as loss without attributing it to individual units.

Table 3.9: Plant-level exergy balance at the design point

	Exergy (kW)	Share of input (%)
Electricity in	1297.7	100.0
Ammonia, chemical exergy	675.8	52.1
Oxygen vented	5.8	0.4
Recoverable heat	46.0	3.5
Lost	570.1	43.9

Just over half of the supplied electricity is stored as chemical exergy in the ammonia product, compared with a first-law efficiency of 59.1% based on the higher heating value. The exergy efficiency is close to the HHV efficiency because the chemical exergy of NH3 is close to its heating value. The vented oxygen and recoverable heat together carry about 4% of the input exergy, setting an upper bound on what downstream recovery could return. Since heat recovery and component-level exergy destruction are not modelled in detail, the balance is interpreted only at plant level.

3.2.5. Limitations

Several simplifications apply to this balance. The values represent steady-state design-point duties, while dynamic effects from ramping, standby and part-load operation are evaluated separately in Section 3.4. Storage losses are excluded, so battery round-trip losses and curtailment are added at system level. The Haber–Bosch loop is modelled with full recycle of unreacted nitrogen and hydrogen and no purge, neglecting inert build-up and slightly understating circulation duty. Finally, the boundary ends at the synthesis-loop outlet, so ammonia separation, storage, conditioning, transfer and transport are outside the balance.

3.3. FESM Simulation Results

FESM sizes an off-grid plant by minimising the levelised cost of its product subject to an annual mass balance. It was given the same 300 t/yr ammonia contract, the same core conversion technologies and renewable-generation options and the same three sites as the plant modelled in this work, and it returns installed capacities, an annual energy balance and a cost stack for each.

One key property shapes the results: FESM applies an annual production constraint, allowing monthly production to vary as long as the annual target is met. So each site produces the contracted volume exactly and its levelised cost is already a cost per contracted tonne.

Resource

Figure 3.2 reconstructs the renewable profiles underlying the FESM results. Neom and Lüderitz hold the stronger annual resource on both counts, wind at 0.61 and 0.64 against 0.53 at Geraldton and solar at 0.33 and 0.34 against 0.26. Both sites translate the stronger annual resource into only a small cost advantage, with LCOA differing by just 2% across the three locations.

The seasonal profiles differ first. Geraldton's wind is nearly flat, between 0.48 in April and 0.60 in December, so its weakest month still delivers 80% of its strongest. Neom and Lüderitz both halve across the year, 0.45 to 0.92 at Neom and 0.44 to 0.87 at Lüderitz. Their two resources also move together: Neom peaks in both wind and solar in June and July and troughs in both in December, and Lüderitz peaks in both in December. Geraldton is the only site where a flat wind resource sits under a solar resource that varies by a factor of nearly two, from 0.21 in June to 0.38 in November.

The daily profiles separate the sites further. Solar holds a plateau between roughly 08:00 and 17:00 everywhere. Geraldton's wind runs against it, averaging 0.66 between 18:00 and 06:00 against 0.36 between 08:00 and 17:00, a factor of 1.8, with a minimum of 0.26 at 14:00 and a maximum of 0.73 at 01:00. The other two are close to flat across the day, swinging by a factor of 1.19 at Neom and 1.03 at Lüderitz, and Lüderitz peaks at 18:00. Geraldton has the weakest wind resource of the three by annual capacity factor and the only one that arrives mainly when the sun is down.

Because FESM enforces the production balance on an annual basis, seasonal variation does not directly constrain feasibility; instead, short-term mismatches in the daily renewable profile are buffered by the battery.

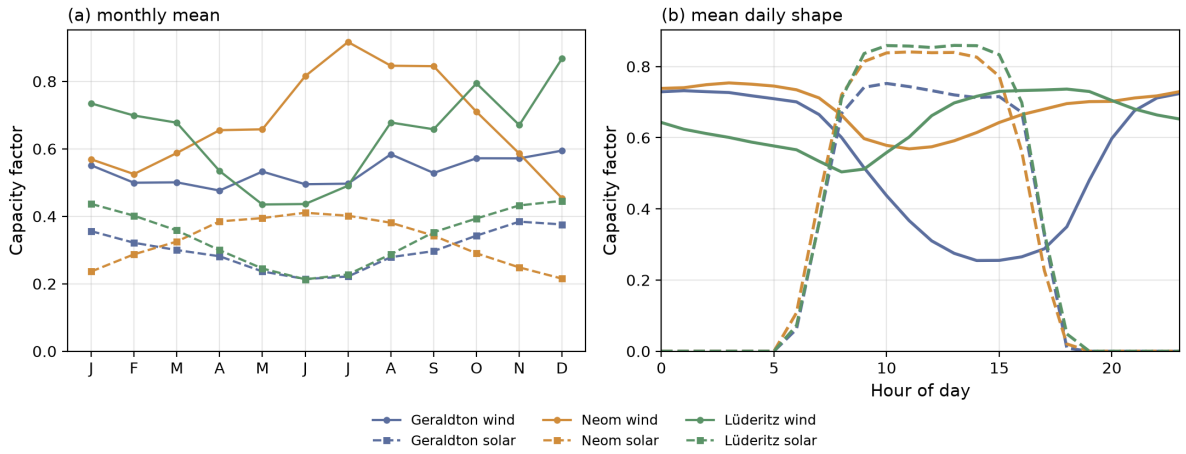

Figure 3.2: Wind and solar capacity factors behind the FESM results. (a) monthly means; (b) mean daily shape.

Configuration

Table 3.10 and Figure 3.3 show that the conversion train changes little between the three locations. Because FESM uses the same annual ammonia-production target at each site, it selects similarly sized electrolysers, nitrogen units and Haber–Bosch loops, operated at high utilisation. The largest differences between locations are found in renewable-generation and storage capacities.

All three configurations remain solar-dominated, but the balance between wind and battery storage differs. Geraldton selects more wind and less battery capacity, while Neom and Lüderitz rely more strongly on storage. This difference follows from the timing of the renewable resource. Geraldton's wind generation is relatively strong during non-solar hours, reducing the amount of electricity that needs to be stored in the battery. At the other sites, wind generation overlaps more with solar production, contributing to periods of already abundant renewable electricity.

The hydrogen buffer remains small at all three locations, indicating that it mainly provides short-term process flexibility. Total capital costs are similar across the sites, although their composition differs. Geraldton spends relatively more on wind generation and less on battery storage, while Neom and Lüderitz allocate a larger share of capital to storage. Since the same component costs are used at every location, these differences reflect the local renewable-resource profiles.

Table 3.10: FESM results at the three sites. Full configurations, energy balances and cost breakdowns are in Appendix A.2.

Quantity	Geraldton	Neom	Lüderitz	Unit
PV peak capacity	1.15	1.29	1.22	MW
Wind capacity	0.25	0.09	0.16	MW
Battery storage	2.56	3.74	3.44	MWh
Electrolyser capacity	0.34	0.32	0.33	MW
Hydrogen buffer	48	20	25	kg H_2
Haber-Bosch loop	35.3	35.5	35.4	kg NH_3/h
Ammonia produced	300.0	300.0	300.0	tonne/yr
Electricity generated	4,207	4,261	4,531	MWh/yr
Electricity consumed	2,788	2,788	2,788	MWh/yr
Curtailed	30.0	29.5	34.2	%
Specific energy consumption	9.29	9.29	9.29	kWh/kg NH_3
Overall efficiency (LHV)	0.368	0.364	0.342	–
Capital cost	3.06	3.01	3.05	MUSD
LCOE, per MWh consumed	63.9	67.3	67.5	$/MWh
LCOA	1,042	1,022	1,035	$/tonne

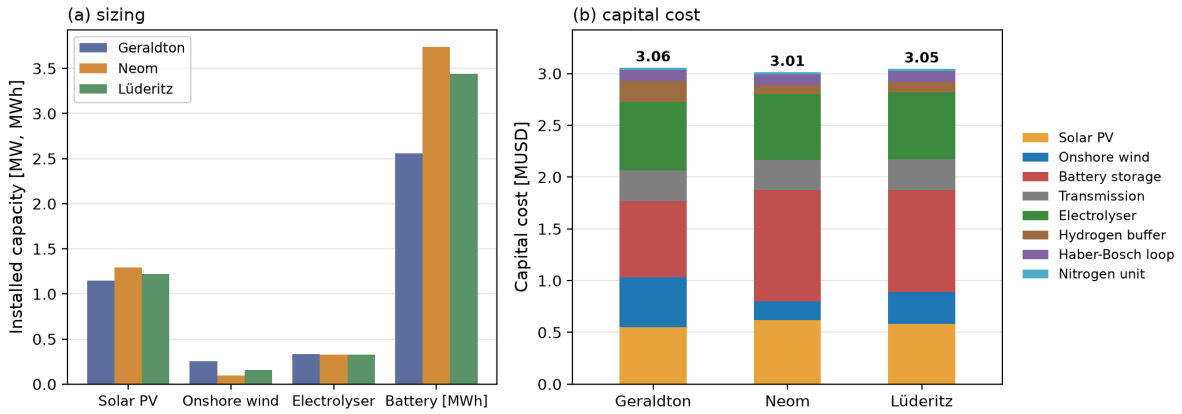

Figure 3.3: FESM configurations. (a) sizing; (b) capital cost by component, with the total in MUSD above each bar.

Energy balance

FESM reports the energy flows of all subprocesses, including conversion losses and curtailment, across the entire ammonia production chain. The model then compares the total energy input to the energy content of the ammonia produced, allowing the overall plant efficiency to be calculated directly. In this framework, the relevant output energy is the lower heating value of the ammonia product, which is 18.6 MJ/kg at all three sites. Electricity flows quoted below are recovered from the installed capacities and capacity factors.

Because the conversion train is identical, so is its demand. All three sites deliver 2788 MWh to the plant, split 2697 MWh to the electrolyser, 55 MWh to the nitrogen unit and 37 MWh to the synthesis loop, and all three reach a specific energy consumption of 9.29 kWh per kg of ammonia at the plant gate. The sites differ only in what it costs to put those 2788 MWh there.

Generation to cover that demand ranges from 4207 MWh at Geraldton to 4531 MWh at Lüderitz. Curtailment is the largest loss at every site, 30.0% of generation at Geraldton, 29.5% at Neom and 34.2% at Lüderitz. Battery round-trip losses run from 72 to 128 MWh at a round-trip efficiency of 90.2%, and transmission losses are approximately 86 MWh at 97.0% efficiency. A third of the electricity generated never reaches the conversion train: 33.7% at Geraldton, 34.6% at Neom and 38.5% at Lüderitz.

The high curtailment reflects the least-cost configuration selected by FESM. In the FESM cost structure, adding generation capacity is cheaper than installing enough battery storage to absorb every surplus kilowatt-hour. Since the battery only shifts electricity that must first be generated, the model accepts some oversizing of the renewable system and the resulting curtailment when this gives a lower total system cost.

Electrolysis is the second loss and is identical everywhere. 2697 MWh produces 53.4 t of hydrogen, a specific consumption of 50.5 kWh/kg and an efficiency of 66.0% on a heating value basis, consistent with alkaline technology. The 53.4 t matches the 53.3 t required stoichiometrically for 300 t of ammonia, so there is essentially no net change in hydrogen inventory over the annual balance. A further 250 MWh is lost across the ammonia-synthesis step when converting hydrogen to ammonia. End to end the plant converts 34.6 to 37.2% of the electricity it generates into ammonia, with Lüderitz lowest because it curtails most.

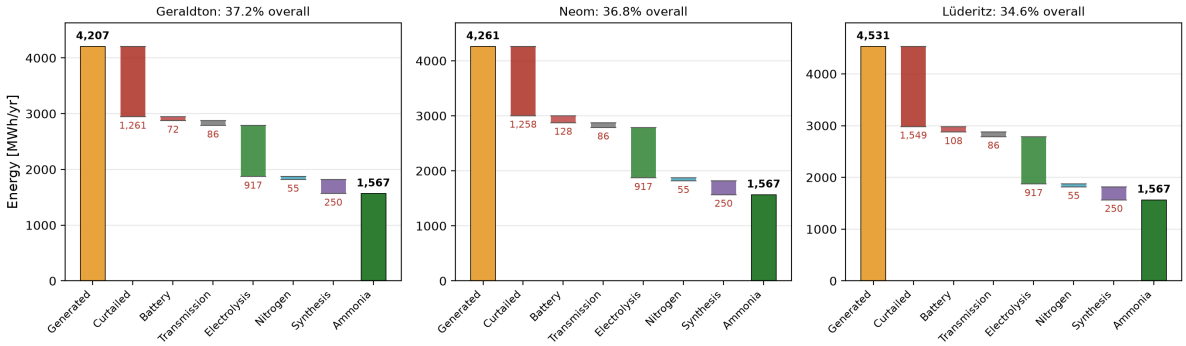

Figure 3.4: Annual energy balance at each site, from generated electricity to the heating value of the ammonia produced. Losses are labelled in red. The underlying flows are tabulated in Table A.3.

Cost

FESM returns very similar LCOA values across the three locations, indicating that the stronger renewable resources at Neom and Lüderitz translate into only a small cost advantage over Geraldton. The detailed electricity-cost and component-level breakdowns are given in Tables A.4 and A.5.

Figure 3.5(a) shows how the cost of electricity increases from generation to delivery at the plant. The generator-only cost is lowest at Neom and Lüderitz because of their stronger renewable resources. Once battery storage, curtailment and transmission are included, however, the differences between the sites become small. Geraldton benefits from using more wind during non-solar hours, which reduces its dependence on battery storage and partly offsets its higher generation cost.

The component breakdown in Figure 3.5(b) shows that battery storage and electrolysis dominate the LCOA. The electrolyser contribution is similar at all locations because the conversion train is nearly

unchanged, whereas the battery and wind contributions vary with the local renewable profile. Geraldton spends more on wind and less on storage, while Neom and Lüderitz rely more heavily on batteries. These opposing cost shifts explain why the total LCOA remains similar despite the different plant configurations.

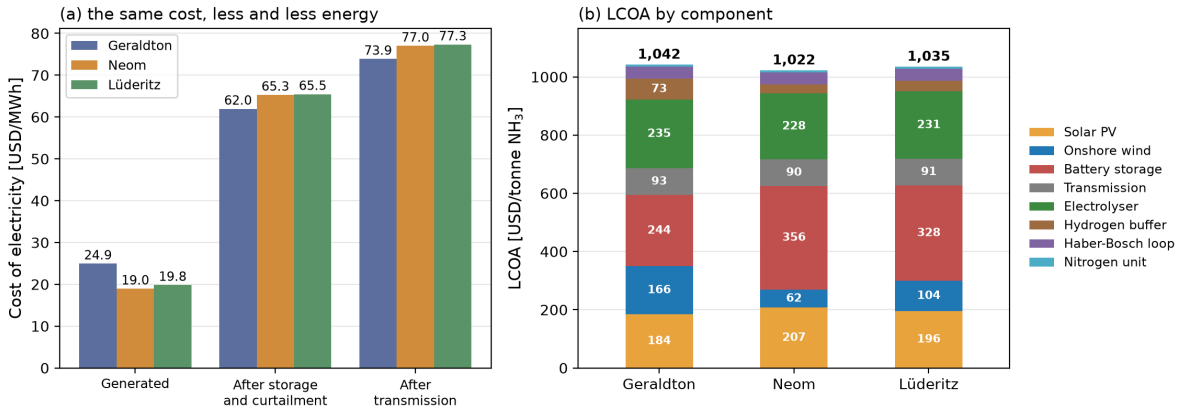

Figure 3.5: FESM cost structure: (a) electricity cost across the supply system; (b) LCOA by component.

Discussion

Neom and Lüderitz have stronger annual wind and solar resources than Geraldton, although the LCOA differs by only 2% across the three sites. The hourly distribution of renewable generation helps explain this small difference. Geraldton's wind is strongest during non-solar hours, reducing battery requirements. At Neom and Lüderitz, wind generation overlaps more with solar production. Despite having the lowest annual wind capacity factor, Geraldton installs the most wind and achieves similar costs through lower storage requirements.

The small cost difference is partly explained by FESM's annual production constraint, which allows weaker months to be compensated by higher production elsewhere in the year. Seasonal variation influences plant sizing, with Geraldton benefiting from more stable wind generation throughout the year. The custom plant model imposes a monthly target of 25 t, making seasonal shortages more consequential. Section 3.5 examines the effects of this stricter constraint, the longer weather record and differences in conversion efficiency.

3.4. Base Case

The base-case sizing was informed from an earlier solar-only FESM optimisation, in which the annual production target was increased to ensure that at least 25 t NH_3 could be produced in every month. This gives a 12 000 m^2 photovoltaic field (2.7 MW peak), a 12 MWh lithium-iron-phosphate battery, a 0.5 MW alkaline electrolyser, a 500 kg hydrogen buffer and a Haber–Bosch loop rated at 100 kg NH_3/h. No control strategy is applied beyond the state machine of Section 2.4; the plant follows the solar resource. All results below are for Geraldton, Australia, over a single meteorological year at hourly resolution.

Table 3.11 and Table 3.12 summarise the annual performance. The monthly target of 25 tonnes is met in all twelve months, so the configuration is feasible. However, it is met with a wide margin: the plant delivers 417.8 tonnes against a contracted 300 tonnes per year, an overshoot of 39%. The monthly production pattern is much flatter than the solar profile would suggest. June is the leanest month at 30.5 tonnes and October the richest at 36.9 tonnes, a spread of only 21%, whereas generation itself swings by 81% between June and December. The relatively stable production is mainly explained by the limited conversion capacity, which restricts output during periods of high renewable generation. With the electrolyser and atmospheric water harvesting operating near their combined nominal capacity, little flexibility remains to convert surplus summer generation into additional ammonia. The limited conversion capacity leads to substantial curtailment during periods of high generation, contributing to the high LCOA.

Function	Value	Units
Monthly targets met	12/12	–
Ammonia delivered	417.8	tonne
Hydrogen produced	73 735	kg
Production energy input	4432.6	MWh
Curtailment	1242.0	MWh
Battery round-trip losses	443.2	MWh
Specific energy consumption	10.61	kWh/kg
LCOA (all production)	1993	$/tonne
LCOA (contracted production)	2775	$/tonne

Table 3.11: Yearly performance of the base case

State	HB loop	Electrolyser
Producing	95.7	97.0
Ramping up	2.3	0.7
Ramping down	0.4	0.2
Standby	0.4	0.6
Off	1.2	1.5
Total	100.0	100.0
Capacity factor	47.7	96.2

Table 3.12: Operating-state distribution

Table 3.12 shows that both subsystems spend most of the year in the producing state, although their actual utilisation differs considerably: the loop averages only 51% of its 100 kg NH_3/h rating while producing, giving a capacity factor of 47.7% against the electrolyser's 96.2%. The loop is oversized. At 17.65 kg H_2/h it can process twice what the 0.5 MW electrolyser can ever supply, 8.75 kg H_2/h. What holds it back is the 500 kg buffer, which rarely carries more than a few hours' feed (11 kg on average while producing), causing the loop's production rate to follow the hydrogen supply from the electrolyser. It also loses more time to non-producing states than the electrolyser despite dispatch priority, since its six-hour cold start and three-hour shutdown make every interruption costly in hours. These periods are concentrated in winter, particularly from May to July, when consecutive overcast days exceed the battery's ability to sustain operation (Figure 3.6).

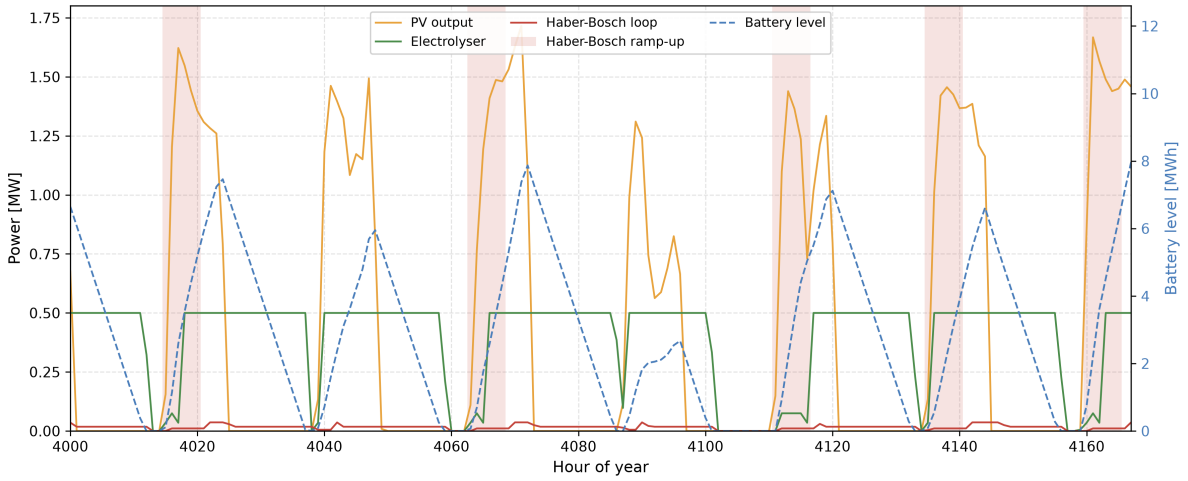

Figure 3.6: Winter week subprocesses output overview

3.4.1. Energy accounting and sizing

Table 3.13 lists the electrical energy each part of the plant consumes over the year, together with the losses that never reach it.

	Energy (MWh/yr)	Specific (kWh/kg NH_3)
Electrolyser stack, producing	4048.0	9.69
Electrolyser, ramp and standby	8.1	0.02
Atmospheric water harvesting	165.9	0.40
Haber-Bosch, producing	152.9	0.37
Haber-Bosch, ramp and standby	2.5	0.01
PSA nitrogen unit	55.1	0.13
Delivered to plant	4432.6	10.61
Battery round-trip losses	443.2	1.06
Curtailed	1242.0	2.97
Solar generation	6118.7	14.65

Table 3.13: Base case annual electrical energy balance

The plant produces 417.8 tonnes of ammonia, that carry 2158.6 MWh at a lower heating value of 18.6 MJ/kg, so the chain from irradiance to product returns 35.3%; measured against only the energy that reaches the equipment it is 48.7%. The thirteen points separating the two ammonia figures are storage and curtailment. The battery absorbs 2654.9 MWh, 43% of the generated energy, and returns it at a cost of 443.2 MWh over 221 full cycles a year at a mean state of charge of 63%, making the assumed ten-year battery replacement interval an important cost assumption. Curtailment is the larger term: 1242.0 MWh, a fifth of everything generated, is curtailed, nearly three times the battery loss, because the electrolyser cannot take up the midday surplus. Energy consumption during ramping and standby is limited to 10.6 MWh, or 0.03 kWh/kg, due to the few interruptions in plant operation. These additional energy demands are excluded from the nameplate specific energy consumption and explain the small difference between the simulated and design values. It is the reason the simulated specific energy of 10.61 kWh/kg is slightly above the design value of 10.58 kWh/kg in Table 3.8. Figure 3.7 traces this cascade and sets the installed capacity of each unit against what is actually used.

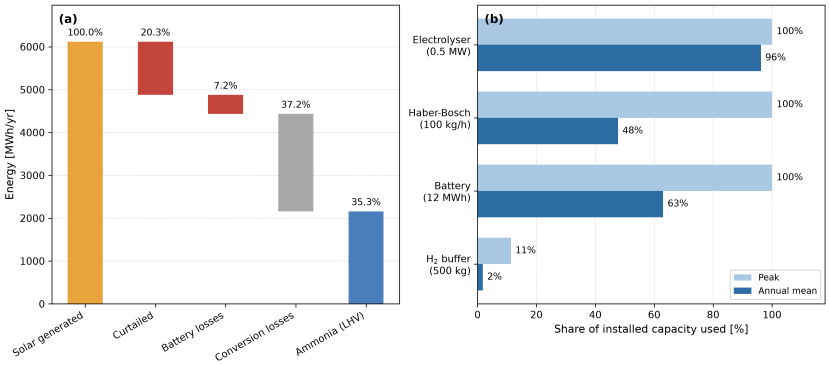

Figure 3.7: Installed capacity against capacity actually used

The downstream conversion capacity is small relative to the PV array. At full load, the electrolyser, Haber–Bosch loop and PSA together consume approximately 0.550 MW, while the 12 MWh battery can sustain this demand for roughly twenty hours. As a result, the plant operates with few interruptions, and the electrolyser reaches a capacity factor of 96.2%. Its limited spare capacity contributes to substantial curtailment, amounting to 1242.0 MWh or 20.3% of annual PV generation. In December alone, solar generation reaches 649.7 MWh, yet ammonia production exceeds the monthly target by only 11.9 tonnes. These results indicate that the subsystem capacities are poorly balanced, with conversion capacity limiting the utilisation of available renewable electricity. Section 3.5 investigates a more cost-effective balance between generation, storage and conversion capacity.

3.5. Optimised Plant Configurations

The base case of Section 3.4 meets its contract but does so inefficiently from an economic perspective: it delivers 39% more ammonia than required and reaches an LCOA of $1,993/t, well above recent large-scale green-ammonia tender prices. The 2025 SECI auctions in India achieved prices of approximately $641/t, with producers eligible for an additional first-year incentive of around $100/t [81]. The H2Global tender established a net price of approximately $890/t, excluding delivery [40]. Modelled delivered prices can be higher, with Argus estimating around $1,160-1350/t [5]. The base case is therefore a technically feasible reference rather than a least-cost design. This section presents the configuration optimisation, varying seven design variables: PV area, wind capacity, battery capacity, electrolyser rating, hydrogen-buffer size, Haber–Bosch loop capacity, and ammonia-storage capacity. The optimisation uses 15 design years (2001–2015) and 10 independent validation years (2016–2025). It examines the optimal configuration, the effect of the addition of wind and ammonia storage, economic competitiveness, and sensitivity to key assumptions. To enable comparison with the base case, the optimisation is first performed for Geraldton, Australia. The analysis is then extended to the other locations. Two optimisation objectives are considered:

- **Scenario A:** minimises $\text{LCOA}_{contracted}$, the cost per contracted tonne, based on 25 t/month, without crediting surplus production.
- **Scenario B:** Minimises the LCOA across all ammonia produced, including surplus production beyond the contractual requirement.

The analysis focuses on Scenario A, as the aim is to meet the contractual requirement at the lowest cost.

3.5.1. Search

The optimisation varied seven quantities: photovoltaic area, onshore wind, battery, electrolyser, hydrogen buffer, Haber–Bosch loop and ammonia tank. Table 3.14 gives the best $\text{LCOA}_{contracted}$ after each search stage.

Table 3.14: Best contracted LCOA after each search stage, against the 15-year criterion.

Search stage	$\text{LCOA}_{contracted}$	Unit
Coarse grid, 4800 designs	965	$/tonne
Refined grid	913	$/tonne
Full grid, 316 008 designs	864	$/tonne
Tank in the optimum	18	tonne

Refining around the coarse optimum lowered the contracted LCOA from $965 to $913/tonne, and the full-grid walk lowered it to $864/tonne. The walk is ordered cheapest first and needed to test only the 18 260 designs whose plant alone was cheaper than the refined result, so no cheaper design on the grid meets the criterion. The refined stage only moves from the coarse winner to the cheapest feasible design nearby, so a cheaper feasible mix in another region of the grid is found only by the full walk. Without a tank the sequence runs from $1297 through $1213 to $1129/tonne. In both runs every cheaper design fails the criterion, so the optimum lies on the feasibility boundary; the nearest point of that boundary is not always the cheapest.

The same coarse-to-fine search was also run on the LCOA of Scenario B, the annualised cost over all ammonia produced, as a check on the objective. For the source year, it reached $795/tonne on the refined grid, but its optimum produces 1726 t/yr, almost six times the contract. Output above 300 t/yr has no buyer under the single-offtaker premise. The contracted LCOA is therefore used as the objective for all subsequent results.

3.5.2. Optimised configuration and performance

Table 3.15 compares the optimised configuration, referred to as the final design, with the base case.

Table 3.15: Base case and final design at Geraldton. Operating indicators and annual results are given in Appendix A.4.

Quantity	Base case	Final design	Change	Unit
PV area	12 000	3000	−75%	m^2
Wind capacity	0.00	0.50	–	MW
Battery storage	12.0	0.5	−96%	MWh
Electrolyser capacity	0.50	0.50	0%	MW
Hydrogen buffer	500	25	−95%	kg H_2
Haber–Bosch loop	100	50	−50%	kg NH_3/h
PSA nitrogen unit	1.98	0.99	−50%	t N_2/d
Ammonia tank	0	18	–	tonne
Capital cost	6.37	2.14	−66%	M$
$LCOA_{25}$, contracted	2775	864	−69%	$/tonne
Ammonia produced, mean	413.8	310.6	−25%	tonne/yr
Design years meeting contract	15 of 15	14 of 15	–	–
Validation years meeting contract	10 of 10	8 of 10	–	–

Most of the cost reduction comes from storage. The battery and hydrogen buffer are cut by an order of magnitude, and their roles are taken over by wind and by the ammonia tank, as Section 3.5.5 explains. The wind turbine and the tank add $274 and $7 of the $864/tonne, so the storage saving outweighs the cost of the new equipment.

The gap between production and delivery in the table is surplus that the buyer cannot take. Delivery is capped at 25 t/month, so the 10.9 t/yr difference between production and delivery is output above the contract. The mean shortfall of 4.3 t/yr in the missed years brings delivery just below 300 t. The monthly dips are covered by the tank, which Figure 3.8 shows. Its median level falls from 18 t at the end of March to 10.9 t at the end of July and refills by November, so most months below 25 t do not cause an annual miss. A miss needs both an empty tank and a year whose total output is close to 300 t, which is the case in 2013. Although the design meets the 90% reliability criterion during optimisation, it meets the contracted delivery target in only 8 of the 10 validation years, falling below the required threshold.

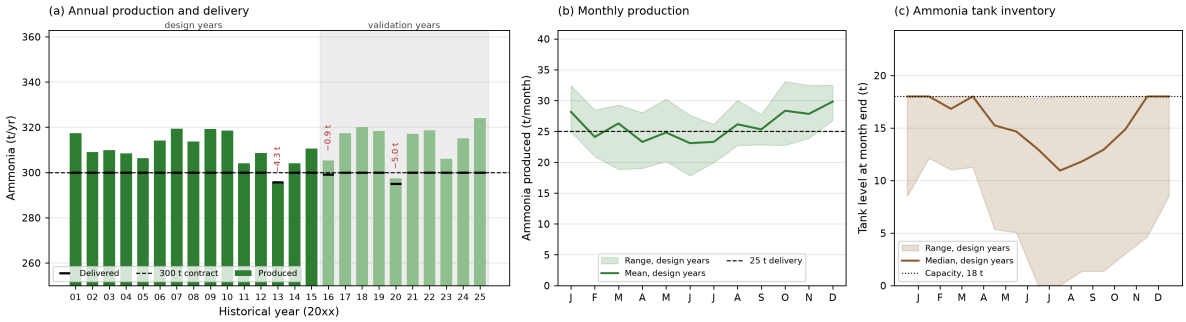

Figure 3.8: The final design over the 25 historical years at Geraldton. (a) Annual production and delivery against the 300 t contract. (b) Monthly production, mean and range over the design years. (c) Ammonia tank level at the end of each month, median and range over the design years.

The final design does not meet the contract in every year, and the criterion does not require it to. It meets the contract in 14 of the 15 design years and 8 of the 10 validation years, and misses in 2013, 2016 and 2020 by 4.3, 0.9 and 5.0 t. In each of these years a run of weak winter months empties the tank. The misses are small: the largest is 1.7% of the annual contract, and the cost per delivered tonne, $865, is almost equal to the contracted LCOA. On the unseen years the design performs slightly worse. Two misses in ten is one more than the 90% rule allows, although the mean shortfall of the failing years,

3.0 t, stays within the 6 t limit. The design is therefore somewhat, but not strongly, fitted to the years it was sized on. The base case meets the contract in all 25 years only because its weakest month never falls below 25.4 t, which requires 114 t/yr more production than it can deliver. The final design accepts a few tonnes of shortfall in 3 of 25 years and in return costs 69% less.

Two qualifications apply. First, each year is evaluated on its own, with the tank starting at the level that the same year restores by its end, so a depleted tank carried from one weak year into the next is not represented. Second, the result is an optimum of the grid: the synthesis loop is stepped in 5 kg/h increments, and the hydrogen buffer lies on the lower edge of the grid at 25 kg. Section 3.5.7 examines both.

3.5.3. Operating behaviour and energy flows

The base case and the final design meet the same contract in different ways. The base case runs at a nearly constant rate, bridges the night with a 12 MWh battery and produces at least 25 t every month. The final design follows the renewable supply, covers the night with wind and uses the ammonia tank to balance the months. Annual values are means over the design years unless a year is named; the hourly figures show 2013, the design year in which the contract is missed. Table 3.16 gives the annual energy balance of both designs.

Table 3.16: Annual electrical energy balance, as means over the design years.

	Base case		Final design	
	kWh/kg	%	kWh/kg	%
Electrolyser, producing	9.69	66.3	9.69	78.3
Electrolyser, ramp and standby	0.02	0.2	0.09	0.7
Atmospheric water harvesting	0.40	2.7	0.40	3.2
Haber–Bosch, producing	0.37	2.5	0.37	3.0
Haber–Bosch, ramp and standby	0.01	0.0	0.02	0.1
PSA nitrogen unit	0.13	0.9	0.13	1.1
Delivered to plant	10.62	72.6	10.69	86.4
Battery round-trip losses	1.07	7.3	0.09	0.7
Curtailed	2.92	19.9	1.59	12.9
Solar generation	14.62	100.0	4.87	39.4
Wind generation	0.00	0.0	7.50	60.6
Total generation	14.62	100.0	12.37	100.0
Generation converted to ammonia	–	35.4	–	41.8

The plant itself uses almost the same electricity per kilogram in both designs, because each unit has a fixed specific demand; only the ramp and standby terms grow, from 0.03 to 0.11 kWh/kg. The difference lies upstream: battery losses and curtailment fall from 27 to 14% of generation, so the final design needs 15% less generation per kilogram and converts 41.8% of it into ammonia, against 35.4% in the base case.

Renewable supply and wind variability

The final design replaces stored electricity with wind. The base case uses 48% of its electricity at night, all of it from the battery, which cycles 2655 MWh/yr. In the final design 39% is used at night and wind supplies 94% of it, so the battery cycles only 169 MWh/yr (Table A.16). This works because wind falls as the sun rises and recovers in the evening, with an hourly correlation of -0.32 with solar (Section 3.5.8). Figure 3.9(a) shows a representative week: the week of 2013 with median generation. While the wind is weak in the first three days, the load follows the sun; from the fourth day the wind keeps the plant near full load through the night. Over the year, wind supplies 61% of generation (Table 3.16).

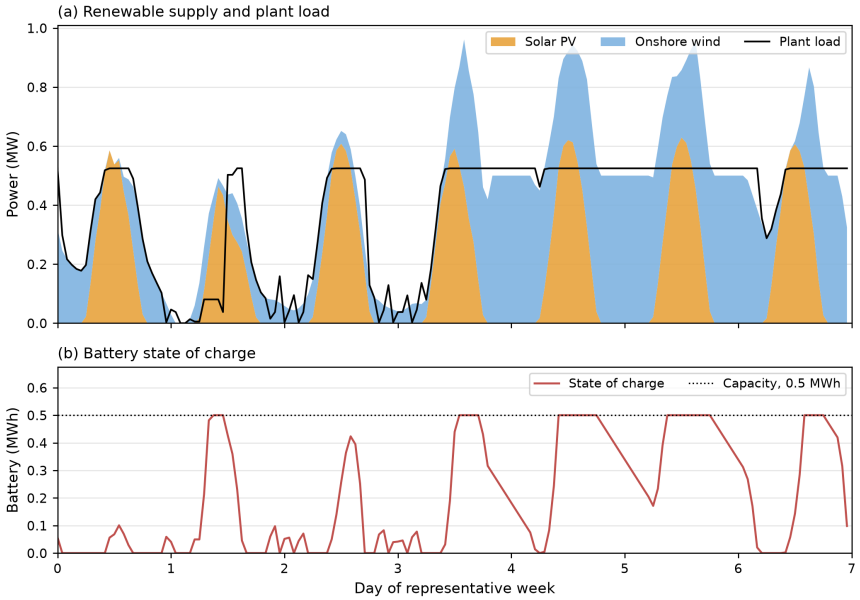

Figure 3.9: Final design in a representative week of 2013. (a) Solar and wind generation against plant load. (b) Battery state.

The battery changes from a bulk store, which in the base case is empty for only 248 h/yr, to a short-term buffer that tops up the wind. It fills around midday and empties overnight (Figure 3.9(b)), and is empty for 39% of the year. It completes more full cycles than the base-case battery, 339 against 221 a year, but handles so little energy that battery losses fall from 7.3 to 0.7% of generation. The fixed ten-year battery life in the cost model does not reflect this higher cycling rate.

Curtailment falls from 19.9 to 12.9% of generation (Table A.16). What remains occurs when the electrolyser, battery or hydrogen buffer is at its limit. Absorbing it would require extra capacity to make ammonia that has no buyer, so curtailing is cheaper. This holds only for an off-grid plant without another use for surplus electricity.

Electrolyser and hydrogen storage

Both designs use the same 0.50 MW electrolyser, but the final design pairs it with far less generation (3.84 instead of 6.05 GWh/yr) and storage (0.5 instead of 12 MWh). This raises the overall energy efficiency: with less electricity curtailed or stored, the share of generation converted to ammonia rises from 35.4 to 41.8% (Table 3.16). The price is a fluctuating load. Whereas the base case runs the electrolyser at full load 95% of the year, the final design runs it at full load for 4526 h/yr, at part load for 3106 h/yr and not at all for 1128 h/yr (Figure 3.10(c)). Within a week its load cycles between zero and full rating (Figure 3.10(a)); over a year it swings by more than half its rating on 261 days against 54, and starts up 63 times against 34. This may accelerate stack ageing, which the model does not capture, as it assumes a fixed stack life and a load-independent efficiency.

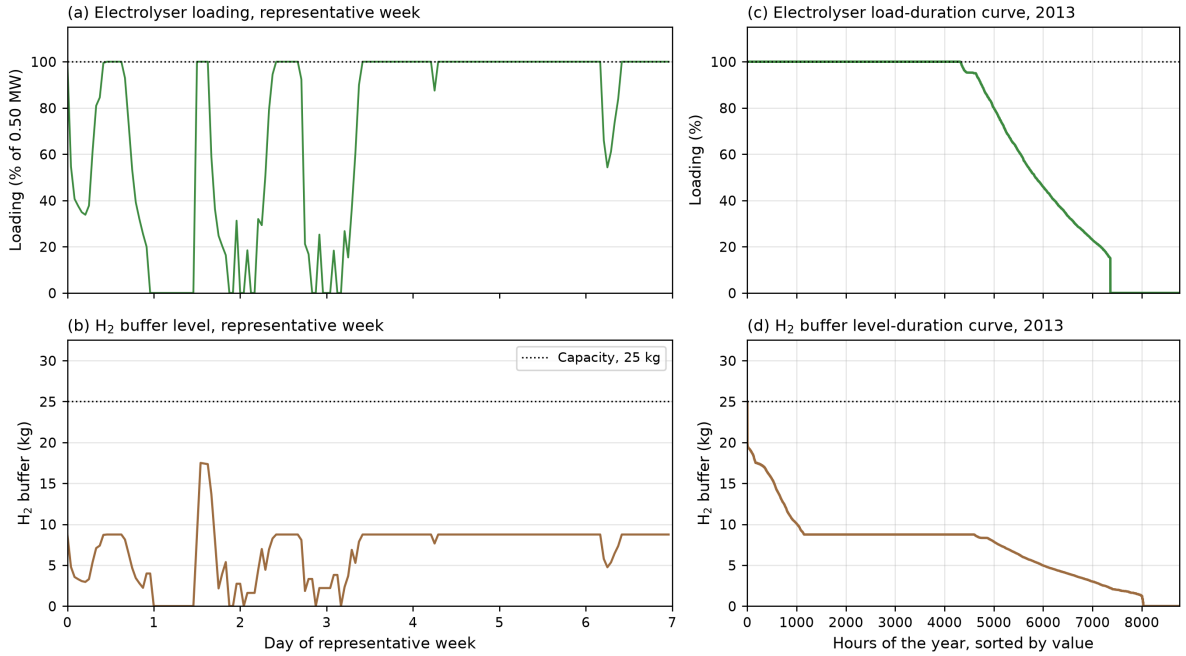

Figure 3.10: Electrolyser loading (a, c) and hydrogen buffer level (b, d) of the final design, in the representative week and as duration curves over 2013. Loading includes water harvesting.

The hydrogen buffer shows the shift from storage to flexibility most clearly. In the base case hydrogen is consumed as fast as it is produced, so the 500 kg buffer never holds more than about 60 kg: 88% of a component costing $431 per contracted tonne is never used. The final design's 25 kg buffer holds 2.8 h of feed for the 50 kg/h loop. With electrolyser and loop both at full load it settles at about 8.8 kg, one hour of feed (Figure 3.10(b) and (d)), and it is full for only 1.5 h/yr. The buffer smooths hourly mismatches rather than storing hydrogen over days, consistent with a 15 kg buffer still passing the criterion (Section 3.5.7). Weather events are bridged elsewhere: by the battery in the base case and by the ammonia tank in the final design.

Haber--Bosch loop operation

The base case's 100 kg/h loop is twice as large as its electrolyser can feed, since 0.50 MW supplies hydrogen for only about 50 kg NH_3/h. It runs almost all year at half its rating, a capacity factor of 47%. The final design halves the loop and nitrogen unit without losing output, which raises the capacity factor to 71%, with 4700 h/yr at or near full rate (Figure 3.11(b)).

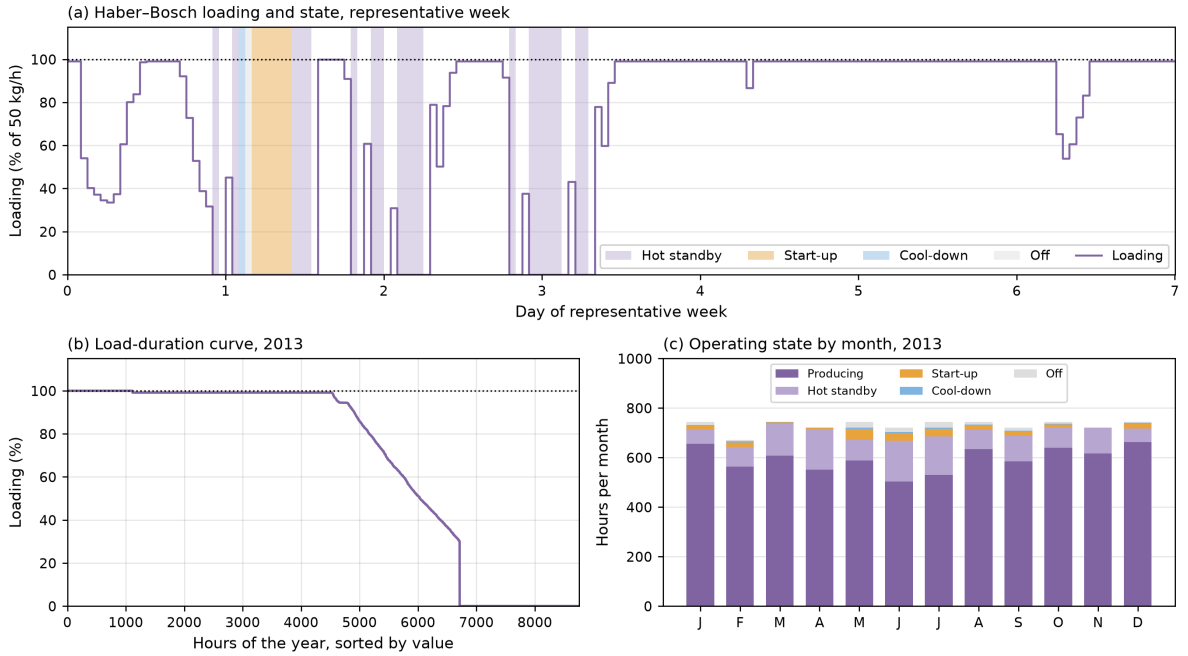

Figure 3.11: Haber–Bosch loop of the final design. (a) Loading and operating state in the representative week. (b) Load-duration curve and (c) monthly hours per operating state over 2013.

Because the supply is intermittent, the loop cannot run steadily: it must run at full rate when energy is available to make up for the hours when it is not. Its 50 kg/h rating therefore lies 40% above its average output, and whenever the small buffer runs empty the loop drops to hot standby, for 1025 h/yr against 54 h/yr in the base case (Figure 3.11(a)). Full shutdowns are rarer, 30 a year against 38, with 181 rather than 228 h/yr in start-up (Table A.16), because wind usually keeps the loop warm; without wind, start-up time rises to 496 h/yr (Section 3.5.5). In 2013 the start-ups cluster in winter, May to July (Figure 3.11(c)).

Standby barely affects energy use (Table 3.16), but its maintenance and degradation costs are not modelled; with fewer cold starts it is probably lower than the base case, but the effect is limited.

Ammonia storage and offtake

The ammonia tank replaces the overproduction of the base case. The base case must produce at least 25 t every month, leaving 114 t/yr without a buyer. The final design lets its weakest month fall to 20.8 t on average and covers the gap from the tank. Each month the tank supplies what production cannot, and is refilled by production above 25 t. Figure 3.12 shows this for 2001, when the contract is met, and 2013, when it is missed.

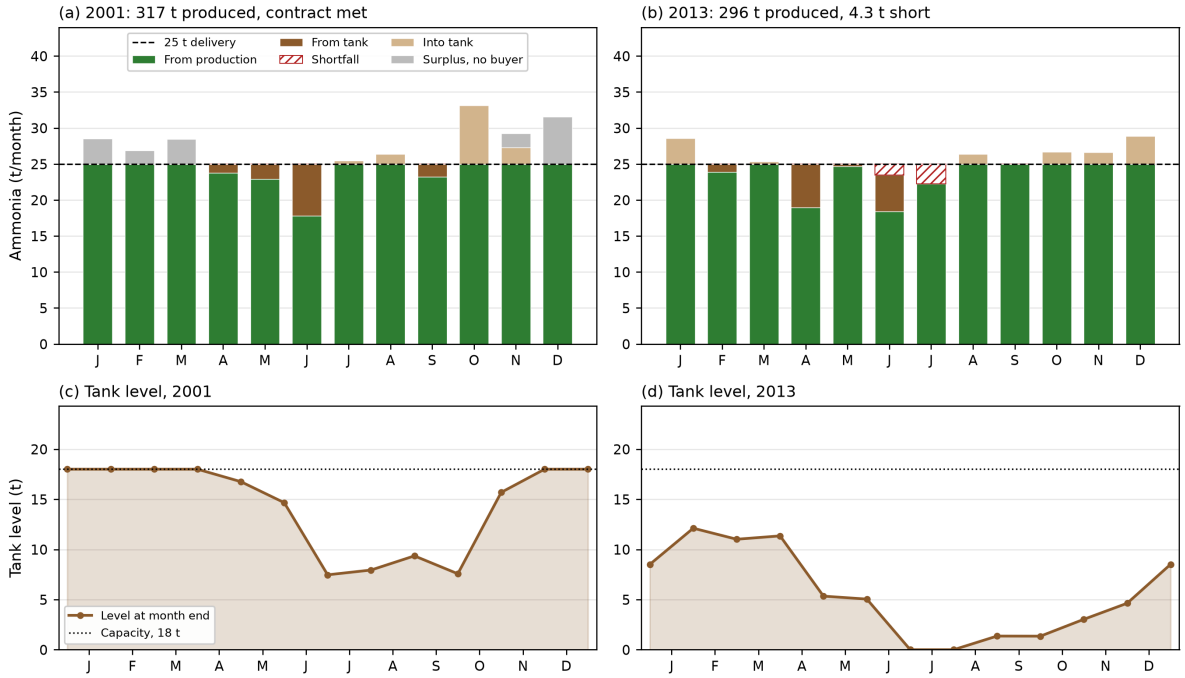

Figure 3.12: Ammonia tank of the final design in 2001 and 2013. (a, b) Monthly ammonia balance against the 25 t delivery. (c, d) Tank level at the end of each month.

In 2001 production falls below 25 t in four months, down to 17.8 t in June. The tank supplies 12.3 t, drops to 7.5 t at the end of June and is full again by November; only 17.4 t is surplus, against 116 t in the base case. In 2013, which produces only 295.7 t, the tank is empty at the end of June and July and 4.3 t of the contract is not delivered. No tank could have prevented this: a tank shifts ammonia between months but cannot make up for a year that produces too little.

Over the design years 96.5% of production reaches the buyer, against 72.5% in the base case. Because the tank covers the weakest month, the plant no longer has to be sized for it: generation falls by a third, from 5.75 GWh/yr without a tank to 3.84 GWh/yr, and the contracted LCOA by $264/tonne (Section 3.5.5), for a tank costing only $6.8/tonne.

3.5.4. Cost breakdown

The cost of the final design is examined in two steps, the electricity it uses and the ammonia by subsystem, and compared with the base case and with FESM (Appendix A.2.3).

Levelised cost of electricity

The electricity supply of the final design, photovoltaics, wind and battery, costs $140.1 k/yr: $36.5 per MWh generated and $42.2 per MWh consumed (Figure 3.13, Table A.18). The difference is the cost of the 13.6% of generation that never reaches the plant: $5.4/MWh for curtailment and $0.3/MWh for battery losses. Wind makes up 59% of the supply cost, photovoltaics 30% and the battery 11%. Wind dominates although its energy, at about $35/MWh, is more expensive than that of photovoltaics, at about $28/MWh.

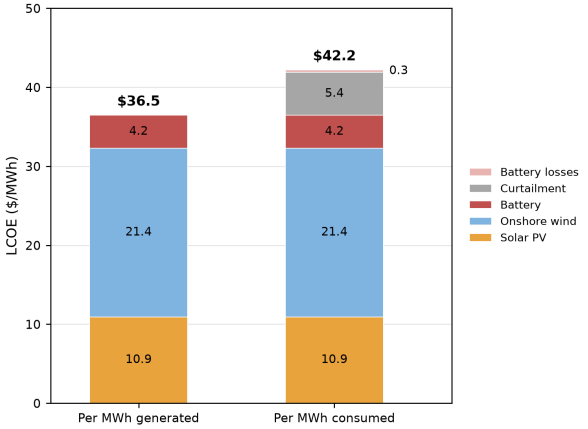

Figure 3.13: Levelised cost of electricity of the final design.

The base case pays $91.2 per MWh generated and $125.7 per MWh consumed. Its 12 MWh battery makes up 70% of its supply cost without generating any energy, and 27.4% of its generation never reaches the plant. The final design thus lowers the cost per MWh consumed by 66%.

For FESM the result depends on the boundary (Table A.4). Its headline $24.95/MWh covers only photovoltaics and wind per MWh generated; on that boundary this design costs more, $32.3/MWh, because 61% of its generation comes from the more expensive wind. Including the battery, the order reverses: FESM reaches $42.3 per MWh generated and $63.9 per MWh consumed, against $36.5 and $42.2 here. The battery makes up 41% of FESM's supply cost, whereas here wind covers the night and is also cheaper, at $1445 against $1913/kW. Per MWh consumed the gap widens because FESM delivers only 66% of its generation to the plant, against 86% here. Transmission, which a co-located plant does not need, raises FESM's cost further to $73.9 per MWh consumed.

Standalone, wind and photovoltaics cost about $35 and $28/MWh in this model, below the $41–55 and $35–47/MWh reported by Fraunhofer ISE [31]. This places the model at the favourable end of published estimates, partly because it excludes land, civil works and photovoltaic degradation (Table A.6).

Per tonne, electricity accounts for $467 of the $864, or 54%, against 66% in the base case and 57% in FESM before transmission. The remaining $397/tonne is the conversion train and the tank.

LCOA breakdown by subsystem

Table 3.17 and Figure 3.14(a) divide the annualised cost of $0.259 M/yr among the components. Since the costs follow from the design rather than the weather, the breakdown holds for every year.

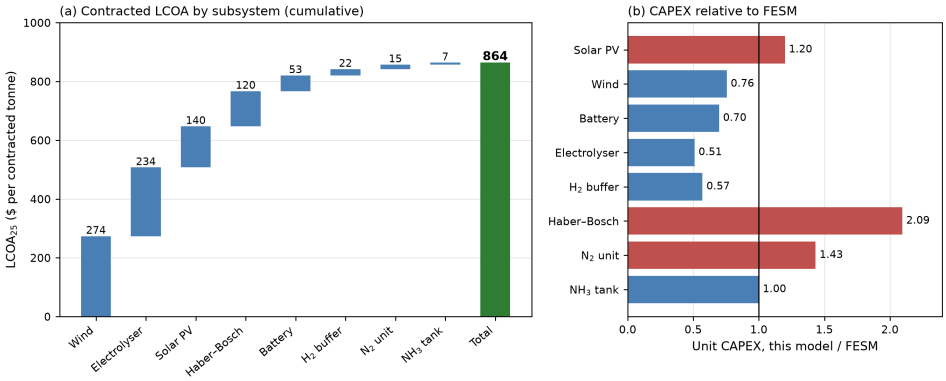

Figure 3.14: Contracted LCOA of the final design. (a) Cost by subsystem. (b) Unit capital cost relative to FESM.

Table 3.17: Annualised cost of the final design by component, over the contracted 300 t/yr.

Component	Annualised cost, M$/yr	Per contracted tonne, $	Share, %
Wind turbine (0.50 MW)	0.082	273.7	31.7
Alkaline electrolyser (0.50 MW)	0.070	233.7	27.0
Solar PV (3000 m^2)	0.042	140.0	16.2
Haber–Bosch loop (50 kg/h)	0.036	119.8	13.9
Battery (0.5 MWh)	0.016	53.3	6.2
Hydrogen buffer (25 kg)	0.006	21.5	2.5
PSA nitrogen unit	0.005	15.4	1.8
Ammonia tank (18 t)	0.002	6.8	0.8
Total	0.259	864.3	100.0

The cost has shifted from storage to generation and hydrogen production. Wind and the electrolyser make up 59% of the contracted LCOA, while the battery and hydrogen buffer, 62% of the base case's cost, make up 9%: the battery falls from $1280 to $53/tonne and the buffer from $431 to $22/tonne, against $274/tonne for wind. Under the model's cost assumptions, wind is the cheaper way to cover periods of low solar output, so the optimisation favours it over additional battery or hydrogen storage

(Section 3.5.5). The electrolyser costs $234/tonne in both designs, but its share rises from 8 to 27% as the rest becomes cheaper.

Because the final design produces only 3.5% more than the contract, its cost per tonne produced, $835, is close to the contracted $864/tonne. In the base case they differ by 27%, $2775 against $2012/tonne, as over a quarter of its output is not sold.

FESM reaches $1042/tonne for the same site and contract, with $3.06 M of capital against $2.14 M (Tables 3.10 and A.5). The comparison is not direct: FESM meets only an annual target, assumes 9.29 instead of 10.69 kWh/kg and includes transmission. Of the $178/tonne difference, $127 comes from cheaper electricity and $93 from transmission, while the conversion train and tank cost $42/tonne more here. The electrolyser costs about the same in both, $234 against $235/tonne, but for opposite reasons: 0.50 MW at $1000/kW here against 0.34 MW at $1961/kW. Wind and battery together cost $327 against $410/tonne, with the balance reversed: $274 on wind and $53 on the battery here, against $166 and $244/tonne in FESM (Section 3.5.5). The Haber–Bosch loop costs more here, $120 against $40/tonne, as both its unit price and its size are higher.

Figure 3.14(b) compares the unit capital costs (Table A.19). This model is cheaper for the electrolyser, hydrogen buffer, battery and wind, at 0.51 to 0.76 times FESM's prices, and more expensive for photovoltaics (1.20), the nitrogen unit (1.43) and the Haber–Bosch loop (2.09). The differences arise because this study costed each subsystem individually, with its own system boundary, for a plant of this configuration and scale (Section 2.4.2), whereas FESM uses older, generic cost assumptions not tailored to this plant. With FESM's prices the order reverses: the final design then costs $1127/tonne (Section 3.5.6), $85/tonne more than FESM's own optimum.

3.5.5. Value of wind and ammonia storage

The final design adds wind and an ammonia tank to the base case and re-sizes every other capacity around them. The value of each is measured by repeating the full search without it, with the same grid, cost model and 15-year criterion (Tables A.16 and A.17, Appendix A.4).

Without wind, the optimum costs $1359/tonne, 57% more than the final design (Figure 3.15). It combines 8500 m^2 of photovoltaics with a 6 MWh battery, a 0.40 MW electrolyser, a 40 kg/h loop and a 16 t tank. Re-sizing alone already halves the cost of the base case, mainly by halving the battery and cutting the hydrogen buffer from $431 to $22/tonne. A solar-only plant must still bridge every night with its battery, however: it cycles 1987 MWh/yr, loses 7.7% of generation and makes up 47% of the cost. Adding wind removes a further $495/tonne: 0.50 MW of wind costs $274/tonne but saves $587/tonne of battery and $257/tonne of photovoltaics, while the larger electrolyser and loop needed to take the supply directly, without a large battery to smooth it, add $71/tonne. Wind is chosen for when it produces rather than for its price (Section 3.5.4): it varies by only a factor of 1.25 between months and complements solar within the day (Section 3.5.3), so it supplies energy in the hours and months for which a solar-only plant must store it. This agrees with Wang et al. [94], who find that combining wind and solar with flexible operation substantially reduces storage needs in off-grid green-ammonia systems.

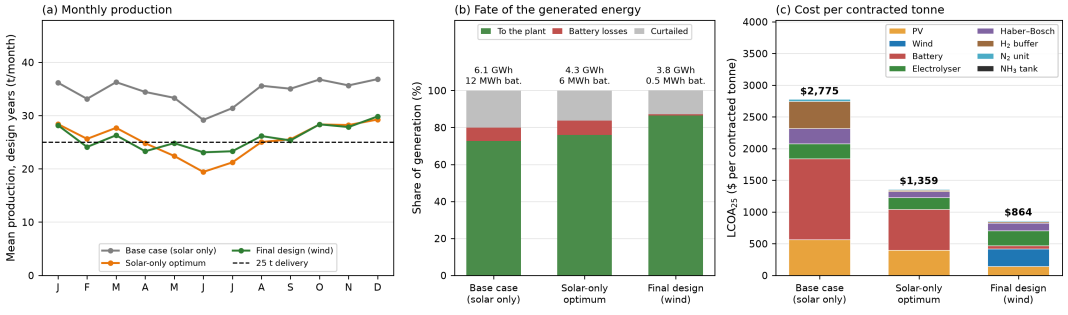

Figure 3.15: Base case, solar-only optimum and final design, as means over the design years. (a) Monthly ammonia production. (b) Fate of the generated energy. (c) Contracted LCOA by component.

Without a tank, the optimum costs $1129/tonne, so the 18 t tank, at $6.8/tonne, saves $264/tonne at equal reliability: both optima meet the contract in 14 of the 15 design years and 8 of the 10 validation

years (Figure 3.16). Without a tank every month must produce 25 t on its own, so production capacity must be sized for the weakest month: 0.80 instead of 0.50 MW of wind, a 0.60 MW electrolyser, 4000 m^2 of photovoltaics and a 55 kg/h loop. This plant generates 5.75 instead of 3.84 GWh/yr, curtails 27.2% of it and produces 389.9 t/yr, of which 23% has no buyer. The tank removes this constraint: it carries surplus ammonia from strong months into weak ones (Figure 3.16(b)), so production capacity no longer has to be oversized for the weakest month, avoiding both overcapacity and overproduction (Section 3.5.3).

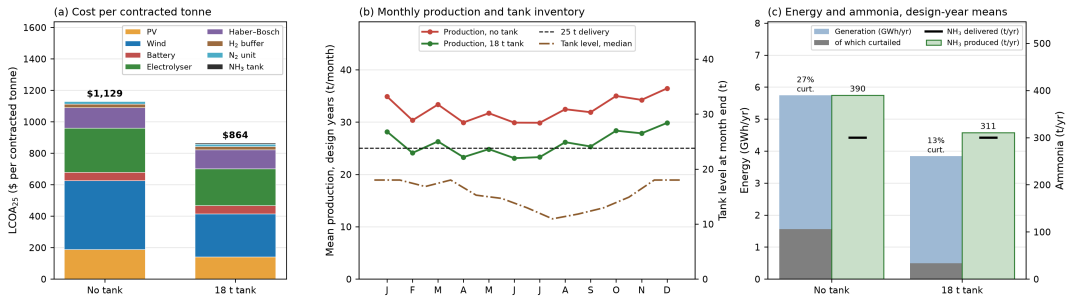

Figure 3.16: Optima without and with an ammonia tank, as means over the design years. (a) Contracted LCOA by component. (b) Monthly production and median tank level. (c) Annual generation, curtailment, production and delivery.

3.5.6. Cost sensitivity and probabilistic LCOA

The calculated LCOA depends on the assumed component costs, which vary considerably across the literature. To assess their influence, the design is first re-optimised using cost assumptions from other models to examine how the configuration and LCOA change. Subsequently, probability distributions are assigned to the individual cost assumptions, as described in Section 2.4.4, to estimate a realistic range of LCOA values for the final design. All results refer to the contracted LCOA.

Cost assumptions

The model prices each subsystem with a linear cost function, $\mathrm{CAPEX}_i = c_i S_i$ (Equation (2.6)), annualised over its lifetime n_i at the discount rate r (Equation (2.7)). The full search was repeated with two alternative price lists, re-optimising the design for each: the optimistic 2030 cost assumptions of Wang et al. [94], which replace only c_i, and FESM's cost basis, which also replaces n_i and r by a uniform 25-year life and a 7% WACC. Table A.19 in Appendix A.5.1 compares both with the cost assumptions of this model. Because feasibility does not depend on price, any change in the optimum is caused by the cost assumption.

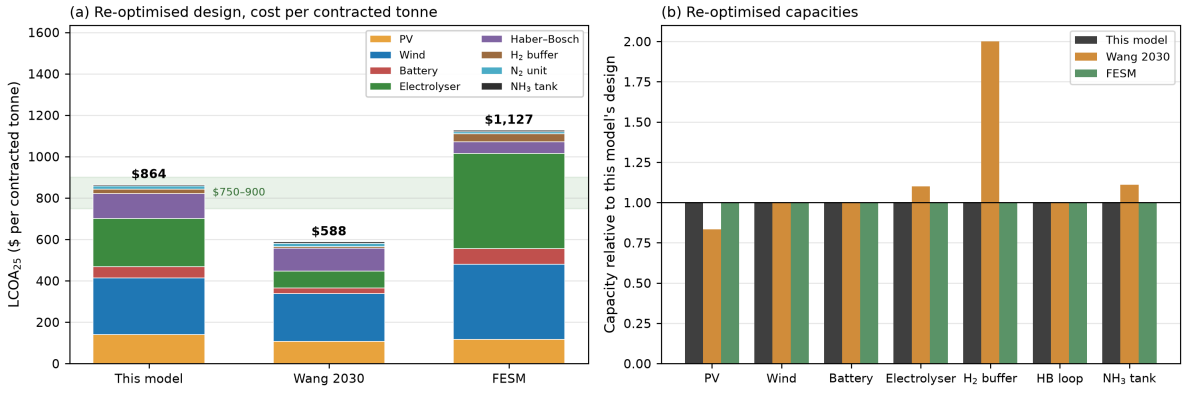

Figure 3.17: Final design re-optimised under each price list. (a) Contracted LCOA by component, against the $750–900/tonne market range. (b) Capacities relative to the final design.

The configuration hardly changes (Figure 3.17). Under FESM's prices the search returns the final design, at $1127/tonne; under Wang's it shifts slightly towards conversion, with a 0.55 MW electrolyser, a 50 kg buffer, a 20 t tank and 500 m^2 less photovoltaics, at $588/tonne. Wind and battery stay at

0.50 MW and 0.5 MWh, although Wang's list halves the battery price. This is because the design is limited by the energy available in the weakest months: a battery only shifts solar energy from day to night, whereas wind adds energy in the hours and months in which solar is weak. Replacing wind by storage also requires more photovoltaics, as in the solar-only optimum with 8500 m^2 and 6 MWh (Section 3.5.5); re-costed at Wang's prices, that plant would still cost about \$854/tonne, against \$588/tonne for the final design.

Two simplifications of the cost model were also tested on the final design without re-optimisation. A 5% balance-of-plant allowance on the annualised cost raises the contracted LCOA to \$908/tonne. Replacing the linear cost function by $c_i S_{i,\mathrm{ref}}(S_i/S_{i,\mathrm{ref}})^{0.65}$ for the Haber–Bosch loop, nitrogen unit and hydrogen buffer, using the base-case capacities as reference, raises it to \$941/tonne. The exponent below one accounts for economies of scale: reducing equipment size yields less-than-proportional capital cost savings. Since all three components are smaller than in the base case, their costs are therefore higher than under linear scaling (Table A.25).

Probabilistic LCOA

The price-list scenarios change all costs together and re-optimise the design for each. The Monte Carlo analysis (Section 2.4.4) instead keeps the final design fixed and samples each capital cost independently within its own range (Table A.23). It therefore shows how uncertain the cost of this particular design is. The deterministic contracted LCOA is \$864/tonne; all five cases are summarised in Table A.24 (Appendix A.5.2).

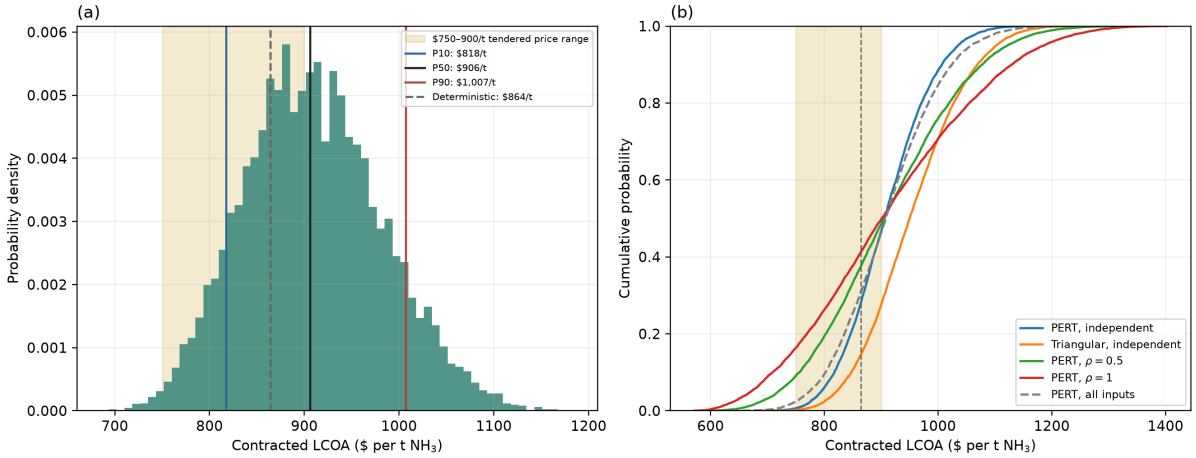

Figure 3.18: Contracted LCOA of the final design under sampled capital costs. (a) Main case, independent beta-PERT distributions. (b) All five cases. The band marks the \$750–900/tonne range of tendered prices.

In the main case, the contracted LCOA ranges from \$818/tonne (P10) to \$1007/tonne (P90), with a median of \$906/tonne (Figure 3.18a). The median lies just above the \$750–900/tonne range of tendered prices, and only 46% of draws fall within it. Since hardly any draws fall below \$750/tonne, this is also roughly the probability that the design breaks even at the top of the range. The deterministic value of \$864/tonne sits at the 28th percentile. The model values lie towards the lower end of their literature ranges, which extend further upwards and often reflect standalone subsystems with their own infrastructure. The deterministic result is therefore optimistic: about 72% of main-case samples cost more.

The other four cases test how far this result depends on the assumed input distributions (Figure 3.18b). The triangular case shifts the median to \$950/tonne and its P10–P90 range to \$847–1069/tonne, because it places more weight on the upper part of each cost range. Correlation changes the spread more than the median: at $\rho = 0.5$, the range is \$756–1078/tonne with a \$904/tonne median, and at $\rho = 1$ it widens to \$709–1130/tonne while the median remains \$901/tonne. Stronger common cost movements therefore widen the tails without materially shifting the middle of the distribution. Sampling financial and operating inputs gives a median of \$908/tonne and a range of \$802–1025/tonne, modestly wider than the main case. In all five cases, the median lies at or above the upper edge of the range of tendered prices.

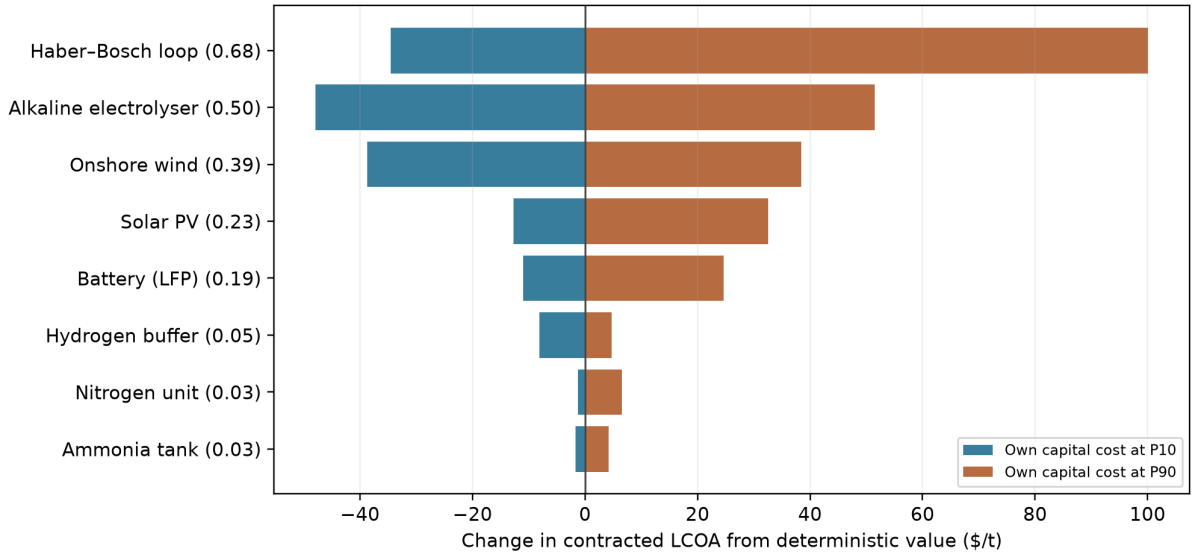

Figure 3.19: Change in contracted LCOA with one capital cost at its own P10 or P90 and all others at their model values. Spearman coefficients of the main case in brackets.

Most of the uncertainty comes from three components (Figure 3.19). The Haber–Bosch loop has the strongest rank correlation with the LCOA (Spearman 0.68), and raising its cost alone to its P90 adds $100/tonne. The electrolyser (0.50) and onshore wind (0.39) follow. Narrowing the Haber–Bosch cost estimate would do most to reduce cost uncertainty.

3.5.7. Sensitivity around the optimum

Because the final design is an optimum on a fixed grid, each capacity, including the tank, was varied in turn with all others fixed, tested against the 15-year criterion and replayed on all 25 historical years. Figure 3.20 normalises the seven sweeps to the final design.

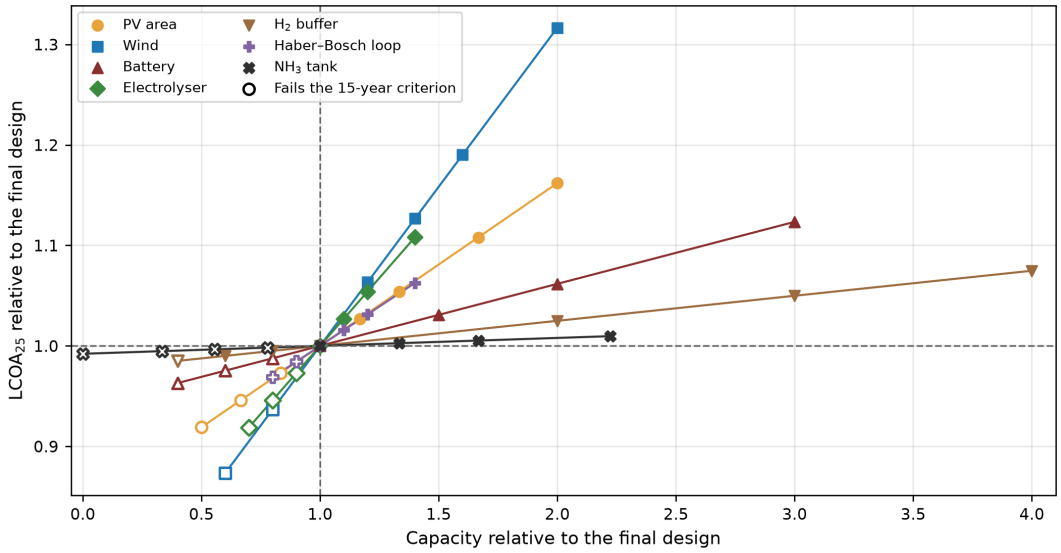

Figure 3.20: One-at-a-time sensitivity about the final design, both axes normalised to that design. Open markers fail the 15-year reliability criterion.

Every single step down breaks the 15-year criterion, except for the hydrogen buffer. The generation and conversion capacities fail clearly: with one step less wind (0.40 MW) the contract is met in none of the 25 years, and with a smaller electrolyser or PV field in only 3 and 17 years. The storage components fail only narrowly. A smaller battery still meets 22 years, but its worst shortfall rises above the 6 t limit,

and a tank below 18 t meets 20 years. Without a tank the contract is met in no year at all, although the whole tank costs only $6.8/tonne. The hydrogen buffer is the only component with slack: 15 kg still passes and would save $8.6/tonne, but the optimisation grid stops at 25 kg as a deliberate margin, since the hourly model does not capture the sub-hourly fluctuations a smaller buffer would have to absorb.

Upward steps show what further reliability costs. One more step of wind, 0.60 MW, meets all 25 years for $54.7/tonne, 6.3% more; one more step of photovoltaics or electrolyser reaches 24 years for about $23/tonne, and a 24 t tank 23 years for $2.3/tonne. A larger loop or buffer adds cost without adding years. Wind therefore both limits the cost and sets the reliability, and the tank is the cheapest reliability on offer.

3.5.8. Location sensitivity

The same search was repeated at Neom in Saudi Arabia and Lüderitz in Namibia, each sized on its own 2001–2015 record and validated on 2016–2025, with and without a tank. Grid, criterion and costs are kept identical to isolate the resource, so site-specific financing, land and construction costs are excluded. Both sites have stronger wind and sun than Geraldton, but their wind varies by a factor of two between months rather than 1.25 and hardly complements the sun (Figure 3.21, Table 3.18).

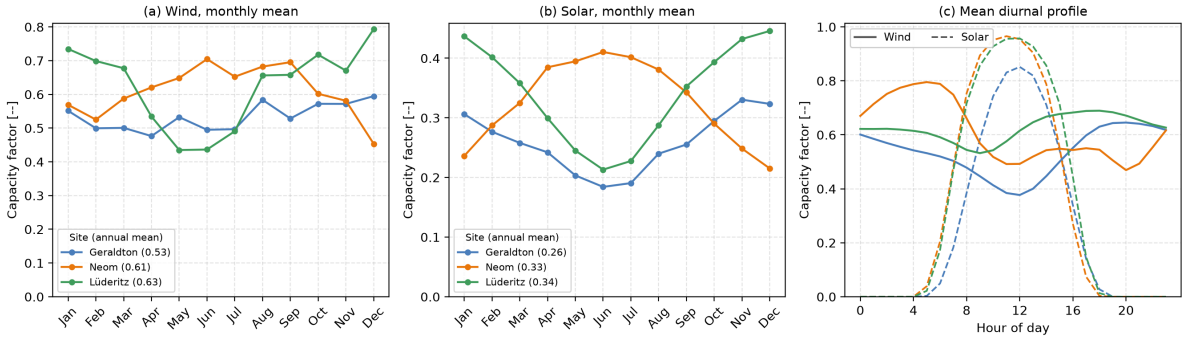

Figure 3.21: Resource at the three sites in the source year (2019). (a) Monthly wind and (b) solar capacity factor. (c) Mean daily profile, wind solid and solar dashed.

With a tank, the three optima are almost the same plant and cost within 2.6% of each other (Table 3.18). Wind, electrolyser, buffer and loop are identical at all three sites. Because the tank shifts production between months, the wind farm is sized on its annual output rather than on the weakest month. Neom and Lüderitz have 14% and 17% more wind than Geraldton over the year, but one step down in the grid, from 0.50 to 0.40 MW, removes 20% of the capacity, so a smaller wind farm would lose more than the better resource gains. The surplus instead allows a smaller solar field, 1000 m^2 smaller at Neom and 500 m^2 at Lüderitz, but this saving is partly spent on a larger battery at Neom and a larger tank at Lüderitz, which makes these sites only slightly cheaper.

Table 3.18: 15-year optimum with an ammonia tank by site. Table A.10 gives the full comparison. Capacity factors are means over 2001–2025.

Quantity	Geraldton	Neom	Lüderitz	Unit
Wind capacity factor	0.53	0.61	0.63	–
Solar capacity factor	0.26	0.33	0.34	–
PV area	3000	2000	2500	m^2
Battery storage	0.5	0.8	0.5	MWh
Ammonia tank	18	18	22	tonne
Validation years met	8 of 10	7 of 10	10 of 10	–
$LCOA_{25}$, no tank	1129	1111	1199	$/tonne
$LCOA_{25}$, with tank	864	850	842	$/tonne
Value of the tank	264	262	357	$/tonne

The configurations differ in how they store energy, which depends on the timing of the resource rather than its annual mean. Neom replaces part of the solar field with a larger battery, which shifts energy within the day. Lüderitz instead needs to shift energy between seasons: its wind and sun are both weak from May to July, so the plant must overproduce in summer and store the surplus as ammonia. This requires a larger tank and a larger solar field than at Neom, despite Lüderitz having the strongest sun. Without a tank the timing matters even more, because every month must deliver 25 t on its own. Lüderitz, with three weak months in a row, then becomes the most expensive site, while Neom, whose weak period is limited to December, stays the cheapest (Figure 3.22(a)). The tank removes most of this penalty, so it is worth most where the seasonal swing is largest: \$357/tonne at Lüderitz against about \$263/tonne at Neom and Geraldton (Figure 3.22(b)).

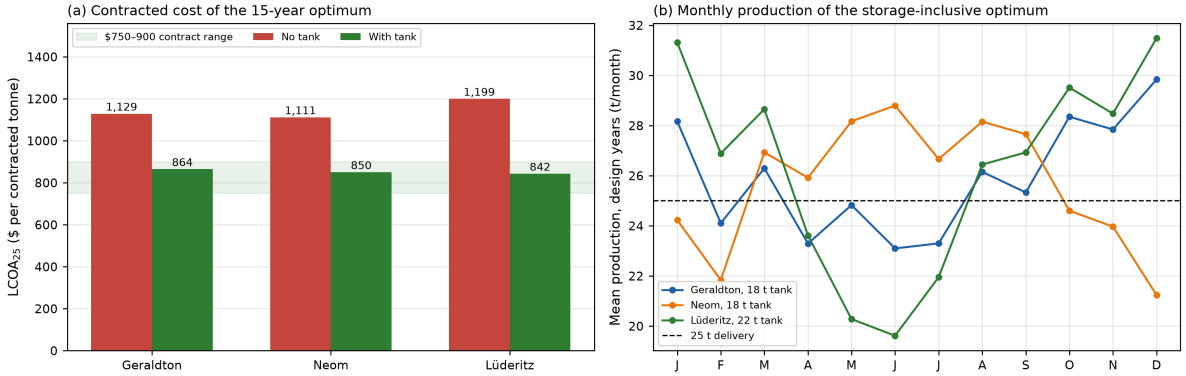

Figure 3.22: 15-year optima at the three sites. (a) Contracted LCOA without and with an ammonia tank. (b) Mean monthly production with a tank, against the 25 t delivery.

The sites differ more in reliability than in cost. All three meet the contract in 14 of the 15 design years, but in the validation years Lüderitz meets it in all 10, Geraldton in 8 and Neom in 7. This follows the margin of annual production over the 300 t contract: about 7% at Lüderitz, 4% at Geraldton and 2% at Neom. With so little margin, Neom misses exactly in its weakest wind years, 2018 to 2020, when annual output falls below 300 t and no tank can make up the difference. Lüderitz is also helped by a validation decade that is windier than its design years.

The timing of the resource, within the day and across the year, therefore matters more than its annual capacity factor, for both configuration and cost. With a tank the sites end close in cost, because storage makes the monthly requirement behave much like an annual one; FESM, which constrains only annual production, likewise ranks them within 2% (Section 3.3). The sites differ mainly in reliability, where Lüderitz, with the widest production margin, is the most robust, although part of its record comes from a windier validation decade.

3.5.9. Competitiveness

Figure 3.23 places the final design among published prices and costs of green ammonia.

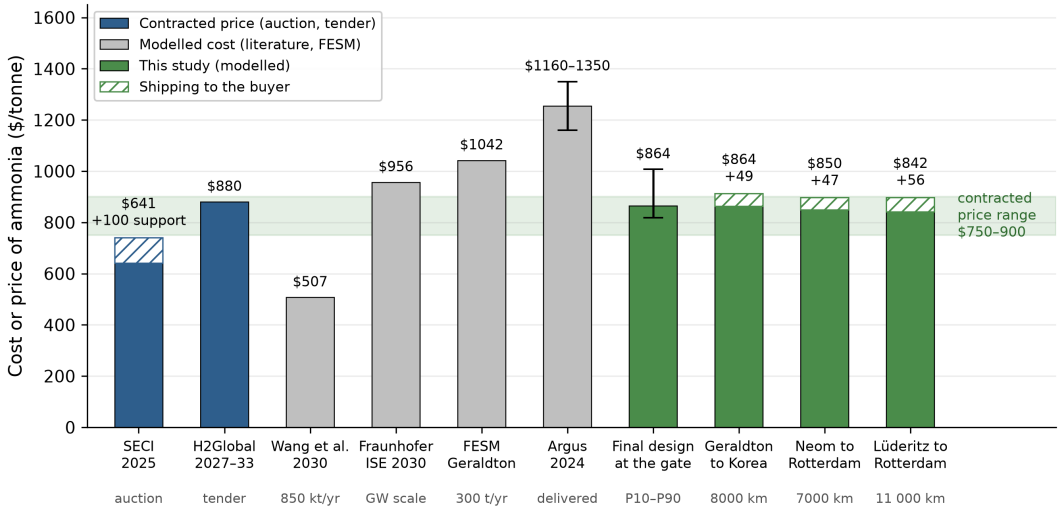

Figure 3.23: The final design against published prices and costs of green ammonia.

The benchmarks differ in reliability and system boundary. The SECI auction and H2Global tender provide the strongest market references, as they represent contracted supply prices rather than modelled costs. The 2025 SECI auction resulted in $641/tonne, supplemented by approximately $100/tonne in production support during the first three years [39]. H2Global awarded a supply contract at approximately $890/tonne for 2027–2033 [40]. Together, these provide an indicative supported reference range of $750–900/tonne. Neither represents an unsubsidised market price.

The remaining benchmarks are modelled costs and differ considerably in scale, system boundaries and underlying cost assumptions: $507/tonne for Wang et al. [94], $956/tonne for Fraunhofer ISE [48], $1042/tonne from FESM (Section 4.3), and $1160–1350/tonne for delivered ammonia from Argus [5].

At $864/tonne, the final design falls within the indicative reference range. The optimised costs at Neom and Lüderitz are slightly lower,at $850 and $842/tonne, respectively. Shipping adds $47–56/tonne, resulting in delivered costs of $897–913/tonne across the three locations. However, these shipping estimates assume large ammonia carriers, which are unlikely to be economical for the small production volumes considered here. Actual transport costs could be higher, further weakening the competitiveness of decentralised production.

Cost uncertainty weakens this competitive position. The Monte Carlo median is $906/tonne, with a P10–P90 range of $818–1007/tonne, and only 46% of simulations fall within the reference range (Table A.24). The deterministic result of $864/tonne represents a relatively favourable outcome. The assumed capital costs remain a major source of uncertainty, as demonstrated by the sensitivity analysis in Section 3.5.6.

3.6. Autonomy of the optimised plant

On the measures of Section 2.5, the final design remains autonomous in the same operational sense as the base case: it runs off-grid without external support. It does so with far less operating margin, because its storage and production surplus leave little room to absorb renewable shortfalls. Table 3.19 gives the measures for both designs as means over the 15 design years. The optimum without a tank (Section 3.5.5) is included as a reference, to separate the effect of the optimisation from that of the tank. Operation itself is described in Section 3.5.3; this section concentrates on the margins.

Table 3.19: Autonomy measures at Geraldton, as means over the design years 2001–2015; the last row covers all 25 historical years. Non-producing hours are all hours outside the producing state.

Measure	Base case	No tank	Final design	Unit
Synthesis loop, non-producing	456	1003	1336	h/yr
share of the year	5.2	11.4	15.2	%
hot standby	54	704	1025	h/yr
cold starts attempted	38	30	30	per year
abandoned partway	0	0.5	0.3	per year
Electrolyser, without output	390	944	1127	h/yr
Battery throughput	221	289	339	cycles/yr
Buffer at 30% turndown	94.4	8.6	9.4	h of feed
Weakest month above the floor	+15.9	+9.9	-16.9	%
Production above the contract	+37.9	+30.0	+3.5	%
Tank level at its yearly minimum	–	–	9.3	tonne
Years meeting the contract	25	22	22	of 25

The final design remains operationally autonomous, but spends far more time waiting. Its synthesis loop is out of production for 15% of the year against 5% in the base case, and this extra time is entirely hot standby, which keeps the loop warm and ready without a restart: the hours in hot standby rise from 54 to 1025, while the hours shut down or starting up fall from 402 to 311. Cold starts, the costliest events for unattended operation, fall from 38 to 30 a year, and only 5 of about 450 over the design years are abandoned partway. The optimum without a tank lies in between, because its larger generation keeps the loop fed for more of the year.

This waiting follows from the much smaller short-term storage. The hydrogen buffer holds about 9 h of feed at minimum load instead of 94 h, so the loop has to wait on the electrolyser within the day (Section 3.5.3). The battery is also far smaller and used much harder, at 339 equivalent full cycles a year, so the ten-year life assumed in Section 2.4.2 may be optimistic. Longer shortfalls are bridged only by the ammonia tank, which at its yearly minimum still holds about 11 days of deliveries.

The tank therefore also carries the delivery margin. The base case clears the monthly floor by 16% in its weakest month and produces 38% more than the contract, and the optimum without a tank keeps a monthly margin of 10%, bought with a 30% annual surplus that has no buyer. The final design lets its weakest month fall 17% below the floor and produces only 3.5% above the contract over the design years, yet it meets the contract in as many years as the optimum without a tank, 22 of 25, because the tank carries production between months.

With such a small annual production margin, the final design is sensitive to output losses and changes in dispatch control. Predictive control may reduce ramping and shutdowns, but can also reduce production [29]. However, improved control cannot fully overcome multi-day renewable shortages with a hydrogen buffer covering only about 9 h. Small output losses may initially reduce surplus production, while larger losses can cause the plant to miss its contracted deliveries.

For the final design this happens quickly. Over all 25 historical years it produces only 4.0% above the contract, so a uniform 4.5% loss lowers mean output below the contract and halves the years meeting it, from 22 to 11; a 12% loss leaves none. A larger tank cannot recover this, because it only moves ammonia between months, so the margin has to come from generation. One more step of wind, 0.60 MW at $54.7/tonne (Section 3.5.7), restores 23 of 25 years under a 4.5% loss, whereas a 12% loss needs 0.80 MW, $164/tonne above the final design, to keep 22. These values are not predictions for this plant, since Groot's system differs in architecture, renewable mix, storage and objective, and a uniform loss is only a first-order approximation, but they show how little output the final design can lose.

The final design and the base case are therefore autonomous in different ways. The base case relies on overproduction: every month clears the floor on its own, and it delivers in all 25 years. The final design relies on inventory: about five months a year fall below the floor (Table 3.15), and the tank covers them in 22 of the 25 years, with little room for any loss of output.

3.7. Electrochemical NRR results

The three cell models of Section 2.6 (Aqueous NRR, Li-mediated NRR and Water-fed membrane Li-mediated NRR) are evaluated here on the cell-level boundary of Section 2.7.1. Each model is first run over its own independent variable to give cell performance, meaning the Faradaic efficiency toward ammonia, the full-cell voltage and the total current density. Those quantities are then split the way the framework of Section 2.7 splits them. The energy side combines voltage and selectivity into a single specific consumption, $4.72\,V_{\mathrm{cell}}/FE_{\mathrm{NH_3}}$ by Eq. (2.40), so a cell can be poor on either and fail. The production side keeps them apart, since only the current that reaches ammonia contributes to rate, $j_{\mathrm{NH_3}} = FE_{\mathrm{NH_3}}\, j_{\mathrm{tot}}$ by Eq. (2.43). Each side is measured against the same reference block and the three routes are then set against each other, because a change that improves one side generally moves the other.

The reference is the base-case conversion block: the alkaline electrolyser at 9.71 and the Haber–Bosch loop at 0.38 kWh kg^{-1}, giving $SEC_{\mathrm{ref}} = 10.09$ kWh kg$^{-1}_{\mathrm{NH_3}}$. The same block delivers 300 t/yr, or 34.25 kg/h. Since producing the hydrogen required for one mole of NH_3 by electrolysis involves the same charge of $3F$ as direct electrochemical NH_3 formation, the electrolyser current density can be used as the equal-active-area reference. A representative alkaline electrolyser value of 0.4 A cm^{-2} therefore gives $j_{\mathrm{NH_3,ref}} \approx 400$ mA cm^{-2}.

The two sides do not carry equal weight in this plant. Generation and storage are the largest cost component, at 54.1% of the levelised cost of the optimised Geraldton configuration and 66.3% of the base case (Table A.8), and this cost scales directly with the electricity the conversion block draws. A cell that consumes ten times the reference energy multiplies that share of the plant by ten, whereas a cell that only needs more electrode area adds stack capital alone. The energy side is therefore taken first: each route is evaluated at its most energy-efficient point (lowest SEC), and the current density is read off there.

3.7.1. Cell performance

Figure 3.24 gives the Faradaic efficiency, the productive current density and the specific consumption of each route across its modelled range, and Table 3.20 lists the operating points.

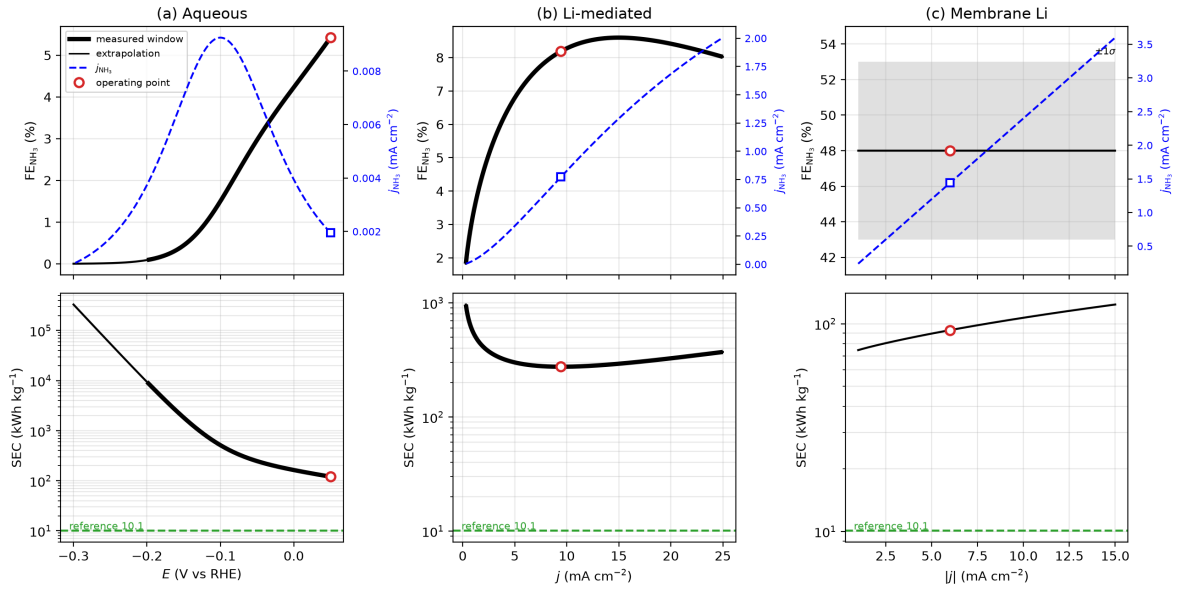

Figure 3.24: Modelled cell performance. Top: Faradaic efficiency (black) and productive current density (blue). Bottom: specific consumption against the reference. Thin segments are extrapolation.

Figure 3.24 presents the modelled performance curves, with representative operating points selected for comparison. The aqueous and dry Li-mediated cells are taken at lowest specific consumption: for the Li-mediated cell, Faradaic efficiency saturates while cell voltage keeps climbing, so V_{cell}/FE turns over at 9.44 mA cm^{-2}, and that minimum is the point reported. The membrane cell has no such

optimum, since its Faradaic efficiency is held constant for a lack of data, so it is reported at its single measured current instead.

For aqueous NRR, specific energy consumption decreases as the potential approaches equilibrium, with the minimum occurring at the boundary of the modelled range. Thermodynamics fixes this point. Nitrogen reduction has its equilibrium at $E^0_{\mathrm{NRR}} = +0.0568$ V vs RHE and the reported $+0.05$ V sits 6.8 mV inside it, so the cell is taken at the least negative potential that still drives a reaction. Going the other way restores current but gives it to hydrogen evolution and adds anodic overpotential, so specific consumption rises immediately.

The membrane cell is modelled across its full current range, but only the voltage terms respond to current; Faradaic efficiency is held constant at the single reported value, 48 ± 5% at 6 mA cm^{-2}, because no measurements are available to determine how Faradaic efficiency varies with current density. Therefore, this measurement point is used as the representative operating point. This is an optimistic assumption: using the 8.19% Faradaic efficiency reported for the dry Li-mediated cell would increase the specific energy consumption from about 93 to roughly 410 kWh kg^{-1}. Both values remain far above the reference due to the combined effect of the high cell voltage and limited Faradaic efficiency.

The same points are set out in Table 3.20, where the productive current density belongs next to the specific consumption. The aqueous cell reaches its lowest energy figure at the potential where it makes the least ammonia, 2.0 μA cm^{-2} against the 400 mA cm^{-2} that would match the electrolyser stack. The dry Li-mediated cell splits the same way in weaker form, so both ends of each are carried through the comparison.

Table 3.20: Modelled operating points on the comparison boundary. A_{stack} sized for 300 t/yr, Eq. (2.46).

Quantity	Aqueous	Li-mediated	Membrane Li	Unit
Independent variable	$E = +0.05$	$j = 9.44$	$\lvert j\rvert = 6.0$	V vs RHE, mA cm^{-2}
Operating point	Min current	min SEC	reference j	–
$FE_{\mathrm{NH_3}}$	5.42	8.19	48.0	%
V_{cell}	1.38	4.78	7.10	V
$j_{\mathrm{NH_3}}$	0.0020	0.773	1.44	mA cm^{-2}
SEC_{NRR}	121	275	93	kWh kg^{-1}
against reference	11.9	27.3	9.2	$\times$
FE needed at this V	64.7	224	332	%
A_{stack}	8 255 000	20 900	11 200	m^2
$j_{\mathrm{NH_3}}/j_{\mathrm{NH_3,req}}$	4.9×10^{-6}	1.9×10^{-3}	3.6×10^{-3}	–

The aqueous cell reaches a maximum ammonia partial current of 9.3 μA cm^{-2} at -0.10 V, after which increasing hydrogen coverage suppresses NRR activity. This creates opposing trends in selectivity and production rate: moving from $+0.05$ to -0.10 V increases the ammonia current by a factor of 4.7, while Faradaic efficiency decreases by a factor of 3.6, raising specific consumption from 121 to 514 kWh kg^{-1}. At the calibration point, the ammonia current is only 6.6×10^{-3} of the nitrogen transport limit, indicating that surface activity is the main limitation. Increasing nitrogen availability through higher pressure or gas-diffusion electrodes would offer limited benefits until surface activity improves.

The dry Li-mediated cell reaches its Faradaic maximum of 8.60% at 15 mA cm^{-2}, but its specific-consumption minimum of 275 kWh kg^{-1} occurs at a lower current, 9.44 mA cm^{-2}. This minimum arises because Faradaic efficiency levels off while the lumped resistive term keeps growing with current, so the product V_{cell}/FE turns over. The reported SEC is a cell-level value and excludes the upstream energy required to supply the proton donor or anodic feed, such as ethanol or H_2; the route-level energy consumption would therefore be even higher.

The membrane cell has by far the highest selectivity but also the highest cell voltage, 7.10 V. Its Faradaic efficiency is 48% during the NRR stage, which sets the production rate, and 36% once the prehydridation charge is included, which is used for the specific consumption. Both values come from a single recent study [97]. so the figure rests on a single source. The tests behind it ran for 6 hours, and membrane degradation is not captured by the model but would lower performance over longer operation, so the reported performance represents the initial operating conditions. Nothing in the model changes with time, since selectivity and every voltage term are fixed. Capturing the drift would require a

degradation law and a time variable, which a single study cannot calibrate and the cell-level comparison of this chapter does not need.

Nevertheless, having established the operating points, it is worth examining the cell voltages behind them: Figure 3.25 shows where each comes from.

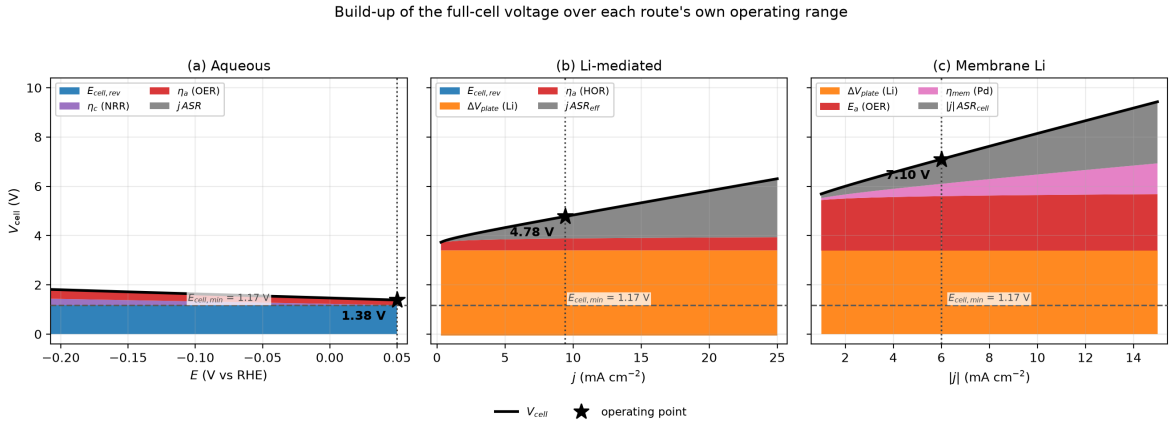

Figure 3.25: Full-cell voltage split into its terms, on the RHE scale. Stars mark the operating points of Table 3.20.

Of the aqueous cell's 1.38 V, 1.17 V is the reversible minimum, leaving 0.21 V of overpotential. Ohmic and transport losses are negligible at 0.0369 mA cm^{-2}, so most of the overpotential occurs at the oxygen anode. The cathode operates only 7 mV from E°_{NRR}, resulting in a low ammonia partial current of 2 μA cm^{-2}. The cell voltage is also below the equivalent base-case electrolyser voltage of approximately 2.06 V. However, with only 5.42% of the applied charge contributing to ammonia production, its specific energy consumption remains nearly twelve times higher than the reference.

The two mediated cells are the reverse. On a common RHE scale the lithium plating detour costs 3.4 V, the same step at the same price in each, since both plate from the lithium couple. That is more than twice the whole aqueous cell voltage, and the mediator chemistry requires it, so no choice of cell design removes it. What remains above it is more tractable: 0.90 V of lumped resistance and 0.48 V of anode in the dry cell, and 2.21 V of anode with 1.50 V of combined membrane and cell resistance in the water-fed one. The anodes differ because their reactions do: the dry cell's 0.48 V is pure overpotential on hydrogen oxidation, whose equilibrium is zero, while the water-fed cell's 2.21 V includes the 1.23 V oxygen equilibrium and leaves 0.98 V of overpotential on the slower reaction. Only those upper bands widen with current. The plating detour means running either cell harder raises production but always at a rising specific consumption, because the fixed 3.4 V is paid per electron while the terms above it grow with current.

3.7.2. Energy parity

Figure 3.26 places the three operating points against the parity locus of Eq. (2.41). The locus is a straight line through the origin with slope $SEC_{\mathrm{ref}}/4.72 = 2.14$ V, and the reversible potential difference $E_{\mathrm{OER,eq}} - E^{0}_{\mathrm{NRR}} = 1.172$ V sets a floor beneath which no cell voltage can fall. The two meet at 54.8%, and below that Faradaic efficiency no cell reaches the reference at any overpotential, however small. At its own Faradaic efficiency each of the three cells is allowed 0.12, 0.18 and 0.77 V before it exceeds the reference, so all three sit beneath that floor.

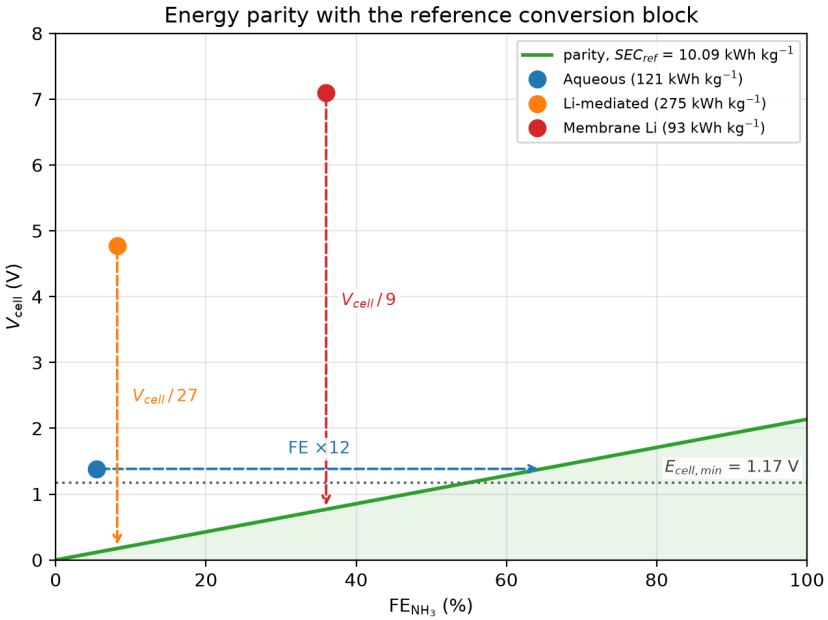

Figure 3.26: The three cells against the parity locus. Points in the shaded region match the reference.

The plane separates the routes into two kinds of shortfall. The aqueous cell needs 64.7% Faradaic efficiency at its 1.38 V to match the reference, a demanding target. Held at 100% selectivity the same voltage would give 6.5 kWh kg^{-1}, already beneath the reference. Its whole gap, a factor of 11.9, is selectivity.

Both mediated routes fail the opposite test. The Li-mediated cell would need 224% Faradaic efficiency at 4.78 V and the membrane cell 332% at 7.10 V, so neither reaches parity even at perfect selectivity. Their voltage must come down as well, and Figure 3.25 shows that most of it sits in the plating detour. For the dry Li-mediated route, this comparison is already favourable, since the upstream energy required to supply ethanol or H_2 is not included.

The aqueous cell's Faradaic loss is different from that of the mediated routes: charge that does not produce ammonia forms hydrogen, which can then be fed to the retained Haber–Bosch loop as in the hybrid argument of Section 2.7. This recovery route is less relevant for the Li-mediated cells because of their plating-based mechanism. The aqueous hybrid configuration is assessed further in Section 3.7.5.

3.7.3. Productive current density and electrode area

Energy parity alone does not show whether a route can reach the required production rate. Figure 3.27 therefore compares productive current density and the active area required for 300 t/yr.

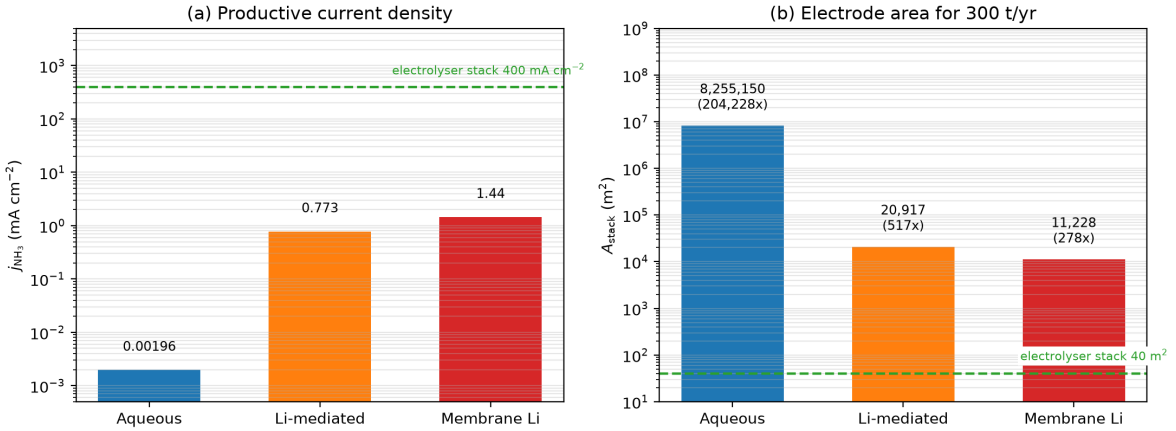

Figure 3.27: Production side. (a) Productive current density and (b) electrode area for 300 t/yr, both against the electrolyser stack.

As derived in Section 2.7, the reference electrolyser corresponds to an ammonia-equivalent productive current density of 400 mA cm^{-2}, which gives an active stack area of approximately 40 m^2 for the 300 t/yr production target. All three NRR routes fall far below this value. The membrane cell reaches 1.44 mA cm^{-2} and the dry Li-mediated cell 0.77 mA cm^{-2}, only 3.6×10^{-3} and 1.9×10^{-3} of the reference, respectively. Meeting the same 300 t/yr target requires approximately $11\,200$ and $20\,900$ m^2 of active electrode, compared with about 40 m^2 for the reference electrolyser stack. The aqueous route is far more restrictive: $j_{\mathrm{NH_3}} = 2.0$ μA cm^{-2} corresponds to only 4.9×10^{-6} of the reference and requires about 8.3 km^2 of active electrode. For a fixed production target, low productive current density therefore appears directly as a large electrode-area requirement.

This trade-off is particularly severe for the aqueous cell. Moving from its minimum-SEC point to its rate optimum at -0.10 V increases the ammonia current by a factor of 4.7 and reduces the required area from 8.3 to 1.7 km^2. However, specific consumption rises from 121 to 514 kWh kg^{-1}, increasing the energy gap from about 12 to 51 times the reference while the area requirement remains roughly 4×10^4 times that of the reference electrolyser stack. The dry Li-mediated cell shows the same trade-off in weaker form: moving from its minimum-SEC point at 9.44 mA cm^{-2} to its Faradaic-efficiency maximum at 15 mA cm^{-2} reduces the required area from $20\,900$ to $12\,500$ m^2, while SEC increases from 275 to 293 kWh kg^{-1}.

What the models support

These cell models are used to compare the behaviour of each route with the reference conversion block, rather than to provide absolute performance predictions. Each model is anchored in a limited number of reported data points and extended across the operating range using fitted or assumed relations. Table 3.21 summarises the basis of the main model inputs and how they are extrapolated beyond the available measurements.

Table 3.21: What each governing number is anchored on, and what carries it away from the anchor.

Route	Quantity	Value	Anchor	Away from the anchor
Aqueous	FE at $+0.05$ V	5.42%	1.50% at -0.10 V	coverage–Tafel model, three fitted parameters
	V_{cell}	1.38 V	OER equilibrium, 1.229 V	literature-based Tafel anode slope and $0.5\ \Omega$ cm^2 zero-gap ASR
	Current scale	$1.96\ \mu$g h^{-1} cm^{-2}	given numerically	Reference current derived from experimental anchor; fitted Tafel slope
Li-mediated	FE at 9.44 mA cm^{-2}	8.19%	two reported (j, FE) points	two-parameter law fixed in closed form by them
	V_{cell}	4.78 V	one (j, E) pair at 2 mA cm^{-2}	resistance forced linear, literature-based Tafel anode slope
	Plating detour	3.40 V	reported plating onset	held constant with current
Membrane Li	FE, operating	48%	one reported value at 6 mA cm^{-2}	held constant, no current dependence resolved
	FE, cycle	36%	reported stage charges, share 0.750	follows the operating value
	V_{cell}	7.10 V	four terms reported at 6 mA cm^{-2}	plating constant, two linear and literature-based Tafel anode slope

The dry Li-mediated cell is the most extensively constrained by reported data. Its selectivity and voltage data nevertheless come from different cells, while the voltage model uses literature-based anode kinetics and a resistance linearised through one point at 2 mA cm^{-2}. This overestimates the reported voltage above 5 mA cm^{-2} and therefore makes the calculated SEC conservative in this region. The precise location of the minimum near 9.44 mA cm^{-2} depends on this resistance relation, but the underlying trade-off between increasing Faradaic efficiency and increasing cell voltage remains.

The membrane model does not predict how selectivity varies with current density: the 48% Faradaic efficiency is an input, while the 36% cycle value follows from the reported stage charges. Its four voltage contributions are also anchored at the same measured current density and sum to 7.10 V, close to the reported 7 V. Away from this point, the current sweep is largely an extrapolation. Varying Faradaic efficiency over the reported $\pm 5\%$ range still places its specific consumption well above the reference, but does not support identification of an operating optimum. The measured 6 mA cm^{-2} point is therefore retained as the representative operating point.

The aqueous model reproduces the qualitative shape of the reported data across the potential window using coverage–Tafel kinetics, hydrogen-evolution competition and site blocking. Its absolute current scale, however, rests on a single calibration point. The resulting 121 kWh kg^{-1} and 8.3 km^2 should therefore be interpreted as indicative rather than exact. The qualitative conclusions are nevertheless robust: at 5.42% Faradaic efficiency, energy parity would require a cell voltage of only about 0.12 V, well below the 1.172 V thermodynamic minimum, while its productive current density remains orders of magnitude below the reference.

3.7.4. Potential for Performance Improvement

Figure 3.28 puts both shortfalls on one axis. Energy runs from 9 to 27 times the reference block and electrode area from 278 to $204\,000$ times, so the two are not the same size of problem and so closing one gap does not necessarily close the other.

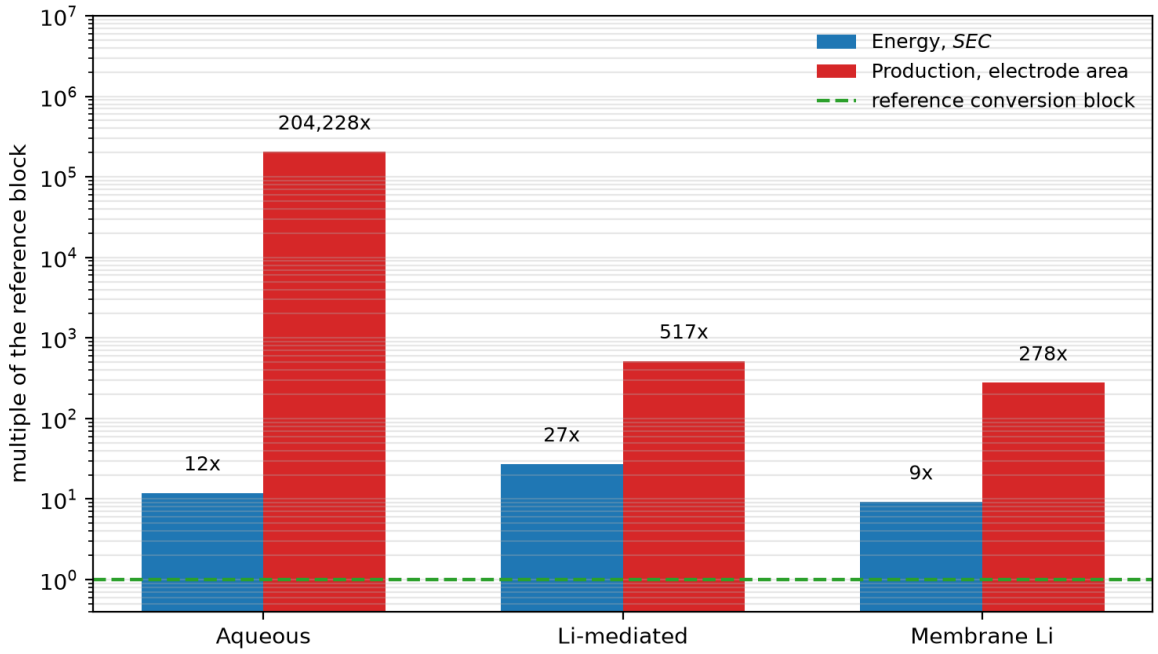

Figure 3.28: Both shortfalls as multiples of the reference conversion block.

Section 2.7.2 defines how the performance gaps are assessed, with the results summarised in Table 3.22. Each limitation from Table 1.1 is linked to the affected model indicator, the corresponding performance gap, the required improvement, and the type of development needed. A score from 1 to 3 is used to indicate how tractable each limitation is, ranging from changes that are already demonstrated to constraints imposed by thermodynamics or the reaction mechanism.

Table 3.22: Key limitations of the modelled NRR routes and their impact on the performance indicators.

Limitation	Affected indicator(s)	Modelled impact	Required improvement	Constraint type	Score
Membrane Li-mediated					
Pulsed operation and prehydridation charge	FE, $j_{\mathrm{NH_3}}$	Cycle efficiency falls to 36% from 48% at the electrode; the 50% duty cycle reduces $j_{\mathrm{NH_3}}$ to 1.44 mA cm^{-2}	Sustain lithium plating and protonation continuously within a single cell	process	2
Cell and membrane resistance	V_{cell}	1.50 of 7.10 V at 6 mA cm^{-2}, corresponding to $250\ \Omega$ cm^2	Reduce separator thickness and electrode spacing while retaining the required non-aqueous environment	engineering	2
Dry Li-mediated					
Interphase formation and interfacial losses	V_{cell}, FE	Interfacial loss rises from 0.90 V at 9.44 mA cm^{-2} to 2.38 V at 25 mA cm^{-2}, while FE remains below 8.6%	Develop a thin, stable and nitrogen-permeable interphase	materials	2
Proton-donor supply and water sensitivity	SEC	The cell-level SEC excludes the upstream energy required to supply ethanol or H_2.	Develop a water-tolerant mediator or alternative reaction pathway	process	2
Shared across Li routes					
Lithium plating potential *(both mediated)*	V_{cell}	Lithium plating contributes 3.40 of 4.78 V and 3.39 of 7.10 V, exceeding the respective voltage budgets	Use a mediator depositing at a less negative potential, or avoid metal deposition entirely	thermodynamic	3
Aqueous					
Potential N_2 transport limitation at higher activity	$j_{\mathrm{NH_3}}$	$j_{\mathrm{NRR}}/j_{\mathrm{lim,N_2}} = 6.6 \times 10^{-3}$, showing that transport does not presently limit the cell	Gas-diffusion electrodes or increased pressure once catalytic activity approaches the transport limit	engineering	1
Competing hydrogen evolution	FE	Hydrogen evolution is kinetically favoured, strongly reducing ammonia selectivity	Increase nitrogen selectivity relative to hydrogen evolution	mechanistic	3
Hydrogen-induced site blocking	FE, $j_{\mathrm{NH_3}}$	Free-site fraction decreases from 0.96 to 0.05 between 0.00 and -0.20 V, separating rate and selectivity optima	Weaken hydrogen adsorption without weakening nitrogen binding, which requires breaking the BEP scaling	materials/ mechanistic	2

Score: 1 = established route to improvement; 2 = plausible but not yet demonstrated; 3 = constrained by thermodynamics or reaction mechanism.

The scoring distinguishes the aqueous and mediated routes. In the aqueous cell, competing hydrogen evolution remains the most fundamental limitation and scores 3: the reversible potentials of the two reactions lie within 57 mV of one another, so any potential that drives nitrogen reduction drives hydrogen evolution as well. This competition remains difficult to overcome with current aqueous NRR catalysts. Hydrogen-induced site blocking is the kinetic consequence and scores 2, because catalyst, surface or electrolyte design can plausibly reduce it, though not freely: nitrogen and hydrogen binding energies are correlated through adsorbate scaling relations [58], so a surface tuned to adsorb nitrogen more strongly tends to adsorb hydrogen more strongly as well, and selectivity cannot be tuned independently of activity. This is why the rate and selectivity optima do not coincide, and why driving the cathode to more negative potentials lowers both FE and the free-site fraction rather than raising the ammonia current. Nitrogen transport scores 1 but is not yet limiting, with $j_{\mathrm{NRR}}/j_{\mathrm{lim,N_2}} = 6.6 \times 10^{-3}$; it would become relevant only once catalytic activity increases substantially. Higher ammonia current density therefore first requires improved nitrogen selectivity and reduced hydrogen-induced blocking, in that order.

The mediated routes show the opposite pattern, and they begin by avoiding the constraint that dominates the aqueous cell: nitrogen is activated at plated lithium rather than at an adsorption site that hydrogen can occupy, so the two reactions no longer compete for the same surface. What they

pay for it is their largest common contribution, the lithium plating potential, which scores 3 because it follows from the lithium redox couple rather than from cell architecture. Most additional losses score 2 and could in principle be reduced through improved cell, interphase or process design. Removing the two membrane-specific limitations would lower the membrane-cell voltage to 5.60 V while restoring the 48% electrode efficiency and full duty operation, corresponding to approximately 55 kWh kg^{-1} and $5\,600$ m^2. Even then, energy use remains 5.5 times the reference and required area 139 times larger, leaving lithium plating as a major structural penalty of the mediated pathway.

3.7.5. Route selection and hybrid configuration

On present evidence, none of the routes is close to replacing the conversion block. On the criteria of Section 2.7.3 the membrane cell is the least distant, but its lead rests on a Faradaic efficiency reported by one study and several times anything the dry cell reaches, which is more than a single measurement can carry. What is left once its tractable entries are cleared is the plating detour in any case. For the dry Li-mediated route, the comparison is additionally optimistic because the upstream energy required to supply ethanol or H_2 is excluded. Ranking the three against each other settles little, since they differ from one another by far less than any of them differs from the reference.

The hybrid arrangement of Section 2.7.4 retains the Haber–Bosch loop and feeds it the hydrogen the cell makes as a side reaction, and that changes the test. Both pathways require three electrons per ammonia molecule, either directly through NRR or indirectly through hydrogen production followed by ammonia synthesis. Current diverted to hydrogen can therefore still contribute to ammonia production. Specific consumption then stops depending on selectivity and becomes $4.72\,V_{\mathrm{cell}} + SEC_{\mathrm{HB}}(1 - FE_{\mathrm{NH_3}})$. Setting that equal to SEC_{ref} leaves a ceiling on cell voltage of 2.06 V and no requirement on Faradaic efficiency at all. That ceiling is the electrolyser's own equivalent cell voltage, so the hybrid test reduces to beating the stack on volts.

One number then separates the routes. The mediated cells sit at 4.78 and 7.10 V, so crediting every non-ammonia electron as recoverable hydrogen still leaves them at 2.2 and 3.3 times the reference, and they fail the hybrid test as they failed the direct one. The aqueous cell spans 1.38 to 1.80 V across its window and clears the ceiling everywhere, between 0.68 and 0.88 times the reference. Figure 3.29(a) puts the two configurations against the whole selectivity range. The direct curves are hyperbolic in FE and only the aqueous one crosses the reference, at 64.7%, whereas the hybrid lines are nearly flat and sit wherever the cell voltage puts them.

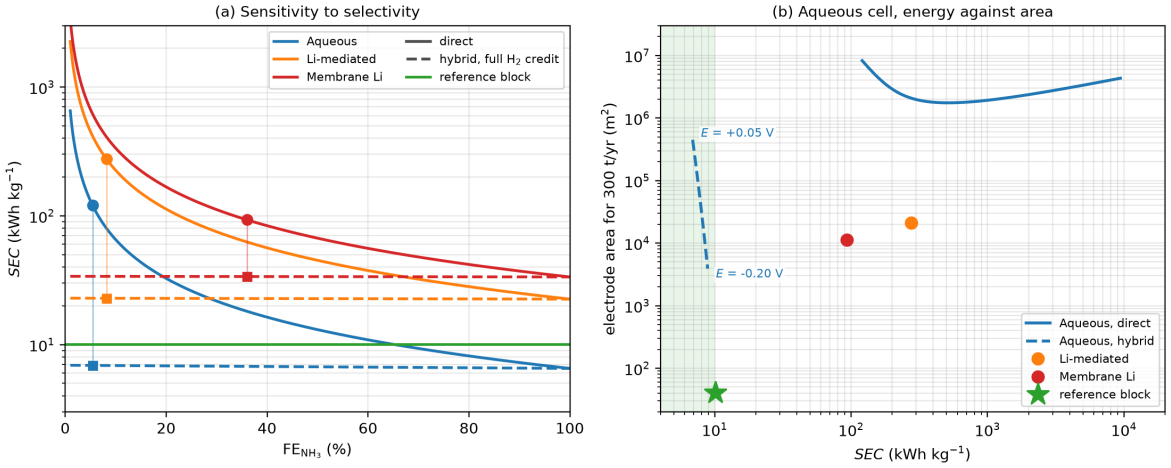

Figure 3.29: (a) Specific consumption against Faradaic efficiency, direct and hybrid. (b) Electrode area against specific consumption for the aqueous cell across its potential window.

Panel (b) follows the aqueous cell across that window, and the production side is what the arrangement changes most. Directly, the electrode carries only the ammonia current, so the trajectory remains well above the reference in energy consumption and turns back on itself at -0.10 V where the rate peaks. In the hybrid the whole current counts, and driving the cell from $+0.05$ to -0.20 V trades 6.89 for 8.88 kWh kg^{-1}, still beneath the reference, against an area falling from $448\,000$ to $3\,900$ m^2. Sacrificing

selectivity therefore carries little energy penalty in the hybrid configuration while increasing the effective production current by a factor of about 115. Even so, the required active area remains about two orders of magnitude above the reference: $3\,900$ m^2 compared with approximately 40 m^2 for the reference electrolyser.

The aqueous cell appears most relevant for further testing, although the nature of its hybrid advantage requires qualification. At -0.20 V its Faradaic efficiency is only 0.09%, meaning that almost all current produces hydrogen rather than ammonia. Its energy advantage arises primarily from the low full-cell voltage assumed for the engineered zero-gap cell, with the recovered hydrogen subsequently contributing to ammonia synthesis. The hybrid configuration is thus closer to a low-voltage hydrogen-producing cell with limited direct NRR contribution. Further experiments should test whether such low full-cell voltages can be maintained as current density is increased toward technologically relevant values while retaining measurable ammonia production. For the mediated routes, further improvement would instead require operation at less negative mediator potentials.

4

Discussion

Within the assumptions of the model, an off-grid plant built from commercially available technologies can supply 25 t of green ammonia every month. The least-cost design combines wind and solar generation with a small battery, a hydrogen buffer and an ammonia tank, and produces contracted ammonia at $864/tonne, near the upper end of current contract prices for green ammonia. Because the optimisation minimises cost subject to a reliability threshold, the resulting design lies close to that threshold. This chapter examines how strongly these results depend on the operating, reliability and cost assumptions, and under which conditions decentralised production could become competitive.

The electrochemical analysis compares three NRR routes with the electrolyser–Haber–Bosch reference. None of them currently matches the reference in both specific energy consumption and productive current density. Aqueous NRR is limited mainly by selectivity and production rate, and Li-mediated NRR by the voltage needed to plate lithium. The third section considers how robust this result is and what it implies for small plants.

4.1. Technical feasibility: plant sizing, location and robustness

The monthly delivery target is the main driver of the design. Without ammonia storage the plant must produce at least 25 t in every month, which leads to about 30% annual overproduction (Section 3.5.5). For the same reason, the seasonal profile of the renewable resource matters more than its annual capacity factor. Without a tank, the stronger resources at Neom and Lüderitz bring little or no saving, since much of the additional energy arrives outside the binding months. With a tank, the cost difference between the three sites falls below 3%, ranging from $842/tonne at Lüderitz to $864/tonne at Geraldton. At such similar costs, differences in delivery reliability become more relevant when comparing locations.

The reliability requirement has a significant influence on the optimal plant configuration. Designing for multiple weather years requires sufficient generation and conversion capacity to maintain production during periods of low renewable availability. Ammonia storage reduces these capacity requirements by allowing surplus production to be used in months with lower output (Section 3.5.5). The choice of reliability criterion also affects the optimisation. The 90% threshold allows a certain number of years to miss the production target without penalty, while exceeding this allowance makes a configuration infeasible. Assigning a cost to undelivered ammonia could lead to a different optimal design.

The optimised design has limited reliability beyond the conditions used for optimisation. Cost minimisation places it close to the feasibility boundary (Section 3.5.7). It meets the contract in 14 of 15 design years, but only 8 of 10 validation years, with shortfalls of up to 5 t. Its annual production margin is approximately 4%, and a 4.5% reduction in output reduces successful years from 22 to 11 out of 25. The historical evaluation also has limitations. Each year is assessed independently, so the effect of a depleted ammonia tank carrying over into the following year is excluded. The 25-year weather record may also miss more extreme conditions or longer-term changes in renewable availability. Given the small production margin, even modest reductions in renewable output, equipment availability or conversion efficiency could significantly affect delivery reliability.

Firstly, the modelled wind capacity factors of 0.53–0.64 are relatively high for onshore wind farms, although they are based on the established VORTEX wind-resource database. Actual electricity pro-

duction may differ due to turbine availability, site-specific conditions and operational losses. Given the limited production margin of approximately 4%, even modest deviations from the assumed wind output could affect delivery reliability.

Secondly, the model assumes full technical availability of all plant components, excluding maintenance, equipment failures and unplanned downtime. Given the limited operational margin, this is an important assumption: a 4.5% reduction in output reduces successful years from 22 to 11 out of 25. Additional wind capacity can improve weather-related reliability, achieving 25 successful years at a 6.3% higher LCOA (Section 3.5.7), but cannot fully compensate for equipment downtime. A practical design would require additional storage, backup capacity or carefully scheduled maintenance, increasing costs. Other simplifications, including constant specific energy consumption, negligible purge losses and excluded degradation, may further overestimate real-world performance.

The model also assumes considerable operational flexibility. The electrolyser consumes most of the plant's electricity and follows the renewable supply, spending 1127 hours per year without production in the final design. Although commercial electrolysers operate over a wide load range, the effects of frequent load changes on their lifetime remain uncertain. The Haber–Bosch loop has different constraints: it can operate down to 30% of its rated capacity, remain in hot standby and restart within six hours (Section 2.4.1). In the final design, it is out of production for 15% of the year, mostly in hot standby (Section 3.6). Such flexibility has yet to be demonstrated commercially for small-scale Haber–Bosch systems. More restrictive operation could reduce production and require additional wind capacity, battery storage or hydrogen buffering, increasing costs.

Beyond component flexibility, autonomous operation also depends on the control strategy. In this model, energy allocation, production and switching between operating states are managed by reactive control logic at hourly resolution (Section 1.4). Groot [29] shows that predictive control can reduce load fluctuations and ramping, potentially limiting component degradation, although this may come at the expense of production. While these results are not directly transferable to the present model, this trade-off is relevant given its production margin of approximately 4%. Compared with the base case, the final design operates more intensively, with battery cycling increasing from 221 to 339 equivalent full cycles per year and Haber–Bosch hot standby from 54 to 1025 hours. However, component lifetimes remain fixed in the cost model, so the potential benefits of smoother operation on degradation and replacement costs are not captured. Furthermore, fault handling, safety redundancy and the continuous energy demand of monitoring and control systems are excluded.

4.2. Economic feasibility: cost assumptions, scale and use case

Under the reference cost assumptions, the plant is marginally competitive with current green-ammonia prices. Its LCOA of $864/tonne lies near the upper end of the $750–900/tonne contract price range, while delivered costs reach $897–913/tonne. These delivered costs assume shipping in a fully loaded large ammonia carrier, which is optimistic for a single small-scale plant. In addition, the median cost under uncertainty is higher, and the extra costs of small-scale, remote operation are not fully captured. Competitiveness also depends on policy support, as grey ammonia is cheaper, averaging $550/tonne in Europe in 2025 [96] and reaching $750/tonne in early 2026 due to rising gas prices [72]. The green-ammonia premium is supported by public tenders [81, 40] and EU carbon regulation [20], making future competitiveness sensitive to policy changes.

The economic competitiveness of the plant is highly sensitive to the assumed component costs. Applying the 2030 cost assumptions of Wang et al. [94] reduces the LCOA from $864 to $598/tonne, with re-optimisation lowering it further to $588/tonne (Section 3.5). In contrast, the FESM cost basis increases it to $1127/tonne, mainly due to higher wind and electrolyser costs. Plant scale has a smaller effect, with an economy-of-scale exponent of 0.65 increasing the LCOA by only $77/tonne. This sensitivity is also reflected in the probabilistic analysis, which gives a median LCOA of $906/tonne, with only 46% of simulations falling within the green-ammonia price band (Section 3.5.6). Across all five uncertainty scenarios, the median remains at or above the upper end of this band. The Haber–Bosch loop contributes most to cost uncertainty, followed by the electrolyser and wind capacity.

Some costs associated with a small first-of-a-kind plant are only partly represented. Site infrastructure is included where already covered by component costs, while a 5% balance-of-plant allowance raises the LCOA to $908/tonne. Although remote locations may offer inexpensive land, additional costs for installation, integration, safety systems and autonomous control could increase this allowance. The

extent of these costs remains uncertain and depends strongly on local conditions. Operation and maintenance, modelled as a fixed fraction of capital cost, also excludes remote-site logistics and staffing. At 300 t/yr, a single full-time operator at an illustrative $100 000 annually would add over $300/tonne. Unattended operation is thus important for economic feasibility, although the additional costs required to achieve it are not fully captured.

The Haber–Bosch loop is the largest source of cost uncertainty, showing the highest Spearman rank correlation with the LCOA (Section 3.5.6). Although Haber–Bosch is a mature industrial process, small-scale loops capable of flexible and autonomous operation have not yet been demonstrated commercially, and reliable cost data remain limited. The reference cost is close to large-scale estimates, while bottom-up estimates for small loops are considerably higher, resulting in an upward-skewed cost distribution. The applied economy-of-scale exponent of 0.65 captures part of this difference but does not account for additional equipment required for flexible operation. Achieving costs close to the reference estimate may depend on further development and standardisation of modular Haber–Bosch systems.

Besides the Haber–Bosch loop, the renewable cost assumptions are also relatively favourable, particularly for wind. The assumed wind costs are based on larger installations, while a small remote wind farm may face higher costs due to transport, foundations and installation. PV costs are more transferable to smaller plants due to their modular nature. The ammonia tank cost is also uncertain, as it is based on larger installations. However, even tripling the assumed tank cost would increase the LCOA by only around $15/tonne, suggesting that its economic benefit remains substantial.

The more relevant economic question for decentralised production concerns the delivered cost. A small autonomous plant is unlikely to compete with a large plant at the production gate. Its potential advantage lies where ammonia is used far from established production, so that the buyer also pays for transport, storage, handling and distribution. In remote agricultural regions supplied from distant import ports, these costs can substantially raise the price paid by farmers [62], and a local plant could avoid most of that supply chain. The modelled sites do not represent this use: Geraldton, Neom and Lüderitz are resource-rich export locations, so the plant studied here is in effect a small export plant competing with large ones on their own ground. For local supply to pay, the avoided delivery costs, together with any value placed on supply security, must exceed the production-cost penalty of the small plant. Repeated deployment offers a second route, mainly for the units not yet bought as modules: the synthesis loop, nitrogen unit and hydrogen buffer. Series production could lower their cost, but because the optimal capacities differ between sites (Section 3.5.8), standardisation would rely on a few unit sizes or several identical units in parallel, with some oversizing. Clustered plants could share infrastructure and maintenance, although this moves back towards centralised production; neither effect is quantified here.

Economic feasibility is not demonstrated for decentralised ammonia as a general substitute for large-scale production. The results identify the conditions under which it could become competitive: substantial avoided delivery costs, cost reductions through repeated deployment, or shared infrastructure, in each case combined with policy that sustains a price for low-carbon ammonia. Establishing any of these cases would require a site-specific delivered-cost comparison with explicit assumptions on learning and shared costs.

4.3. Implications for electrochemical NRR

Each NRR route is represented by a reduced-order model based on published experimental data and reported loss mechanisms. These models capture the main relationships between cell voltage, Faradaic efficiency and ammonia production rate, but rely on simplified assumptions and limited data. The results should be interpreted as an indication of each route's limitations and its performance gap relative to Haber–Bosch, rather than as predictions of actual cell performance.

The choice of datasets involved a trade-off between recent performance and complete, consistent measurements. The aqueous model uses a single isotope-verified operating point [35] and the hydrogen-coverage mechanism of Choi et al. [14]. The dry Li-mediated model combines a 2019 Faradaic-efficiency sweep [49] with voltage data from later studies [95, 25]. This older dataset provides the operating dependence required for modelling, although its maximum efficiency of 8.6% is below more recent results [25, 16]. The membrane model relies on a single six-hour study [97], with constant Faradaic efficiency due to insufficient data. While recent advances could narrow the perfor-

mance gap, the main conclusions remain: below 54.8% Faradaic efficiency, no cell can match the reference SEC, and lithium plating alone prevents the Li-mediated routes from reaching energy parity even at perfect selectivity.

The aqueous model describes the cathodic current with a one-directional Tafel expression, which neglects the reverse reaction. This approximation is generally valid at sufficiently high overpotentials, but near the equilibrium potential the reverse rate becomes significant, and the Tafel form may overestimate the net current at a given potential. The model may consequently underestimate the voltage needed at low current density, potentially giving an optimistic minimum specific energy consumption if the optimum falls in this region. A more detailed kinetic treatment, such as Butler–Volmer, could increase the predicted minimum energy and widen the gap to the reference. However, the overall conclusion is unlikely to change, as the productive current density at such low overpotentials is already far below that of the reference.

The comparison boundary is a second choice. Each cell is compared with the conversion block it would replace, at its most energy-efficient operating point. Ammonia recovery from a dilute aqueous or organic electrolyte, electrolyte management, supply of the proton donor, degradation and balance of plant are excluded, and including them would widen the gap on both axes. The boundary also excludes what NRR could save beyond energy. The cells operate close to ambient temperature and pressure, and a single stack with its own electrolyte and product recovery would replace the electrolyser, hydrogen buffer and high-pressure synthesis loop. The electrode-area comparison uses the same boundary: it covers only the electrolyser stack and not the hydrogen buffer and synthesis loop that the reference route also requires. The area ratio is therefore unfavourable to direct NRR and does not represent total plant footprint. How a full plant comparison would turn out is therefore open. The cells are also evaluated at steady state, so their ability to follow a variable renewable supply is not tested.

Within these limits, the NRR routes face different technological barriers to reaching parity with Haber–Bosch. For aqueous NRR, low Faradaic efficiency and productive current density remain the main limitations, as increasing the applied potential favours hydrogen evolution. Overcoming this requires catalysts that improve ammonia selectivity and production rates, potentially by addressing the underlying adsorption-energy scaling relations. Li-mediated NRR faces a different challenge: lithium plating alone requires approximately 3.4 V, making energy parity difficult even if other voltage losses are reduced. Further improvements in membranes and cell design could reduce these losses, but a lower-energy reaction pathway would be needed to approach the reference SEC. Although NRR could eventually simplify ammonia production by eliminating the conventional hydrogen supply and synthesis loop, its current performance does not offer a competitive alternative for the autonomous plant considered here.

4.4. Model scope and limitations

The model assesses the techno-economic feasibility of autonomous ammonia production through hourly energy flows, operating states and production constraints. The dynamics of individual process units are simplified, and the hourly resolution limits the accuracy of very small hydrogen-buffer simulations, where artificial on–off cycling can occur. More detailed dynamic modelling would help validate the operation and sizing of these components.

A second limitation is that technical and economic uncertainties are evaluated separately. The optimisation identifies the lowest-cost configuration under fixed performance and reliability assumptions, while the probabilistic analysis varies costs for that same design. Lower renewable output, reduced availability or weaker component performance could affect both the optimal configuration and its cost. These effects may compound, as additional capacity needed for reliable operation would further increase costs already close to or above current market prices. The analysis establishes the feasibility and cost sensitivity of the modelled configuration, but cannot determine the joint probability of reliable and profitable operation.

5 Conclusion

This research set out to answer two questions: whether a decentralised autonomous ammonia plant powered by renewable energy sources is techno-economically feasible, and whether electrochemical nitrogen reduction (NRR) can replace the electrolyser and Haber–Bosch loop as the synthesis route of such a plant. The first question is answered by designing and costing a Haber–Bosch-based plant and comparing it across three sites, the second by comparing three NRR routes with that plant as the benchmark. Under the model assumptions, the plant can meet its monthly contract, but its reliability falls short of the target in independent validation years and its economics are marginal. NRR cannot yet replace the Haber–Bosch route, since none of the three routes studied comes close in energy use or production rate.

5.1. Autonomous renewable ammonia plant

A decentralised autonomous ammonia plant is technically feasible within the assumed operating conditions, but its reliability is not yet proven. At Geraldton, the final design meets its contract of 25 t per month using local solar and wind electricity, air and water in 14 of 15 design years (93.3%), which satisfies the 90% reliability criterion (Table 5.1). In the independent validation years, it meets the contract in only 8 of 10 (80%), and across all 25 historical years in 22 (88%), both below that criterion. The model also assumes 100% technical availability, without maintenance downtime or equipment failures. Technical feasibility is thus demonstrated for the design period under these assumptions, but reliable operation has not been confirmed against the validation criterion.

Table 5.1: Final plant design, reliability and cost at Geraldton.

Component or indicator	Value	Unit
Solar PV	3000 (0.68 MW peak)	m^2
Onshore wind	0.50	MW
Battery storage (LFP)	0.5	MWh
Alkaline electrolyser	0.50	MW
Hydrogen buffer	25	kg H_2
Haber–Bosch loop	50	kg NH_3/h
PSA nitrogen unit	0.99	t N_2/d
Ammonia tank	18	t NH_3
Contracted output	300 (25 per month)	t NH_3/yr
Design years meeting contract	14/15 (93.3%)	years
Validation years meeting contract	8/10 (80%)	years
All years meeting contract	22/25 (88%)	years
Assumed technical availability	100	%
Contracted LCOA, deterministic	864	$/tonne
Contracted LCOA, median (P10–P90)	906 (818–1007)	$/tonne

The plant concept follows from the multi-criteria analysis, which selected solar photovoltaics for the base case (joint highest score with the hybrid PV–wind option), lithium iron phosphate batteries, an alkaline electrolyser, pressure swing adsorption and atmospheric water harvesting around a Haber–Bosch loop. Onshore wind was retained as an option and added during configuration optimisation. Most of these technologies are commercially established; the atmospheric water supply and a small, flexible Haber–Bosch loop are less proven. Electrolysis dominates the energy demand, accounting for 91.5% of the plant's electricity use, so its efficiency largely determines the size of the renewable supply.

The cost of off-grid operation is determined mainly by how the plant deals with seasonal variation in renewable supply. Combining wind and solar strongly reduces the need for battery and hydrogen storage, and a small ammonia tank is the cheapest way to absorb the remaining seasonal mismatch. Together, these measures reduce the cost from $2775/tonne for the solar-only base case to $864/tonne. Sizing the plant across multiple weather years is essential, since a design based on a single year meets the contract in only 3 of the 25 historical years.

Among the three sites, Geraldton, Lüderitz and NEOM, location affects cost mainly through the seasonal timing of wind and solar. Without an ammonia tank, the weakest months set the plant size, so Lüderitz is 6% more expensive than Geraldton despite its stronger annual resource. With a tank the three sites lie within 3% of each other. All three sites were selected for strong renewable profiles, so this result compares favourable sites with each other. Among such sites, product storage has a larger effect on cost than the choice of site.

Economically, the plant approaches current green ammonia prices but cannot yet be considered competitive. Its LCOA of $864/tonne lies within the indicative $750–900/tonne tender-price band, although cost uncertainty and potential reliance on policy support limit this comparison. The results show that economic feasibility depends strongly on component costs, which remain uncertain and scale-dependent, particularly for small-scale ammonia production. Competing with large centralised plants at the production gate is therefore unlikely under current assumptions. The main economic opportunity for decentralised production may instead lie in supplying remote users directly, where avoided transport, storage and distribution costs could offset higher production costs. As this potential advantage was not quantified, the economic case for decentralised production remains unproven.

Operationally, the final design maintains off-grid operation in the hourly simulation, but with little margin. Its annual production exceeds the contract by approximately 4%, and a 4.5% reduction in output reduces the number of successful years from 22 to 11 out of 25. The model assumes full component availability and simplified operating-state control, while degradation, unplanned outages and detailed safety and maintenance requirements are excluded. These limitations, together with the shortfall in the independent validation years, mean that further operational validation and potentially additional capacity are needed before reliable unattended operation can be claimed.

5.2. Electrochemical nitrogen reduction

Electrochemical nitrogen reduction cannot yet replace the electrolyser and Haber–Bosch loop of such a plant. At the operating points represented by the reduced-order models, the three routes studied use between 9 and 27 times the energy of the benchmark, which requires 10.09 kWh/kg. Their productive current densities are several hundred to about 200 000 times lower, so for the same output they would need correspondingly larger electrode areas.

Each route is limited by a different mechanism, which indicates where improvement must come from. The aqueous route is limited by selectivity and production rate: it would match the benchmark energy only at a Faradaic efficiency about twelve times its present value. The Li-mediated routes are limited by the voltage of about 3.4 V needed for lithium plating, which prevents energy parity even at perfect selectivity. Combining an aqueous cell with the Haber–Bosch loop lowers its energy use, but only because the cell then acts mainly as a large, low-voltage hydrogen generator, so this hybrid offers no route to direct synthesis.

These comparisons cover cell-level energy use and production rate. They exclude downstream duties such as ammonia recovery and electrolyte management, and they rest on limited experimental datasets. They also leave out the potential advantages of NRR: operation near ambient temperature and pressure, a more modular production route, and no high-pressure synthesis loop. These advantages address the constraints this study found in the Haber–Bosch loop, which is out of production for 15% of the year, mostly in hot standby. However, these benefits were not quantified, and the ability of

NRR to operate flexibly under intermittent renewable electricity remains unproven. Given the substantial gaps in energy consumption and productive current density, none of the investigated NRR routes is currently a viable alternative to Haber–Bosch. Significant improvements in Faradaic efficiency, current density and cell voltage are required before NRR could become attractive for small-scale autonomous ammonia production.

6

Recommendations

This chapter draws on the limitations of the study to identify areas for further research and support a more comprehensive assessment of decentralised ammonia production. It covers a remote-demand use case, validation of subsystem operating assumptions, refinements to cost estimates and system modelling, and electrochemical nitrogen reduction.

6.1. A remote-demand use case

Site and delivered-price benchmark: The three sites of this study were selected for their renewable resource, and partly for the availability of weather data in the simulation software, not for a nearby ammonia demand. The plant was also judged against tendered prices, $750–900/tonne band. The economic argument for decentralised production, however, rests on a site where the ammonia is used directly and centrally produced ammonia has to be transported, stored and distributed to the point of use. A worked-out use case should model such a site, for example an inland agricultural region that applies ammonia as fertiliser or a remote operation that uses it as fuel, with weather data from a source not limited to the built-in sites of the software. It should compare the local plant with the delivered cost of centralised ammonia at that site, including inland transport, storage and distribution, so that the comparison is made where decentralisation could have its advantage.

Demand profile: The present contract asks for 25 t every month, whereas fertiliser demand is typically concentrated in a few application windows a year. Because location acts mainly through the timing of the weather, a seasonal demand turns that timing into a design variable: a resource that peaks ahead of the application season may need less generation, though a larger tank, than a resource with a stronger annual total that peaks after it. The use case should therefore size the plant against the demand profile of the site rather than a flat monthly contract.

Product form: The plant-level boundary ends at the synthesis-loop outlet, and the use case should extend it to the form in which the ammonia is used. Direct application as anhydrous ammonia requires storage and handling at the point of use, whereas conversion to urea or ammonium nitrate adds process units and, for urea, a carbon dioxide source that the autonomous plant concept does not provide.

Carbon score and carbon policy: This study assessed cost but not life-cycle emissions. Future research should quantify the emissions associated with the plant, particularly those embodied in the solar field, wind turbine, battery and electrolyser, and compare them with conventional ammonia production. Steam methane reforming alone emits approximately 1.22 t CO_2 per tonne of ammonia, excluding additional emissions from fuel combustion, natural gas supply and transport [43].

Carbon emissions also affect economic competitiveness through policy. For example, the EU requires renewable fuels of non-biological origin to achieve at least 70% greenhouse-gas savings [19], while its Carbon Border Adjustment Mechanism introduces a carbon cost for imported ammonia and fertilisers [20]. Future research should therefore determine the carbon price at which local green ammonia becomes competitive with delivered fossil ammonia and assess which policies apply to the selected

market, since EU regulations do not necessarily benefit producers serving remote markets outside the EU.

6.2. Validating subsystem operating assumptions

The optimised design relies on simplified assumptions about how individual subsystems respond to variable renewable power. Future work should refine these assumptions using supplier data, component tests and operating records, then assess how the revised inputs affect plant sizing, costs and delivery reliability.

Haber–Bosch synthesis loop. The model assumes that the loop can turn down to 30% of its rated capacity and restart from cold within six hours. Under these assumptions, the optimised loop spends 1,025 h/yr in hot standby and makes about 30 cold starts per year. Testing should establish the minimum stable load, standby heat loss and restart time, and assess how repeated cycling affects catalyst performance. The model should also account for purge losses and inert build-up.

Atmospheric water harvesting. The model uses a single energy-demand estimate of 0.40 kWh per kilogram of ammonia, while water yield depends strongly on humidity. Measurements across a range of temperatures and humidities would allow water output and electricity consumption to vary with the weather in the model.

Control, maintenance and degradation. The model uses predefined control rules, a fixed annual maintenance cost and fixed component lifetimes. The simulated duty includes 339 battery cycles and 63 electrolyser starts per year. Future work should use operating data and control tests to estimate how cycling, faults and maintenance affect equipment availability and service life. These estimates would allow the optimisation to account for the trade-off between operating flexibility and equipment wear.

6.3. Cost basis

Component costs: The LCOA is highly sensitive to component costs (Section 4.2), particularly the small-scale Haber–Bosch loop. Its cost should be validated through supplier quotations or a bottom-up estimate at approximately 1.2 t/d. Site-specific balance-of-plant, water-harvesting and sub-megawatt electrolyser costs should also be established, as well as wind costs for one or a few turbines at a remote site.

Repeated deployment: Building the same design repeatedly could reduce the cost of the units not yet bought as modules: the synthesis loop, nitrogen unit and hydrogen buffer. Future work should estimate their learning rates and weigh the savings of a few standard unit sizes against the cost of oversizing, since optimal capacities differ between sites (Section 3.5.8). The assessment should also examine whether deploying several plants at the same site could reduce the cost per tonne by sharing ammonia storage, maintenance services and other site infrastructure.

Financing and uncertainty: The 8% discount rate should be reassessed for a remote first-of-a-kind plant. The cost correlations in the probabilistic analysis are scenario assumptions and could be estimated from observed price data, and the design could be re-optimised for selected cost scenarios.

6.4. Weather Variability and Model Scope

Multi-year weather, control and reliability: Each year is simulated independently, with the ammonia tank returning to its initial level, so consecutive weak years are not represented. A continuous multi-year simulation, extended with synthetic or climate-projected weather data, would better capture these risks. Furthermore, the current rule-based dispatch could also be compared with model predictive control (MPC) based on weather forecasts. Since smoother operation may come at the expense of output [29], such a comparison should quantify the trade-off between operating stability, component wear and delivery reliability. Finally, the 90% reliability threshold treats permitted shortfalls without economic penalties. Introducing delivery penalties or backup supply costs would allow the optimiser to balance additional capacity against the cost of missed deliveries. Combining weather, availability

and cost uncertainty in a single analysis would show the probability that the plant is both reliable and economic.

Time resolution and system boundary: The hourly model cannot reliably resolve hydrogen buffers much smaller than one hour of electrolyser output. Since a 15 kg buffer remains feasible and reduces costs by $8.6/tonne, sub-hourly modelling could determine whether further reductions are possible. Furthermore, the plant-level energy balance excludes ammonia separation, storage and handling duties. Future work should quantify these additional energy requirements, particularly for refrigerated or pressurised ammonia storage.

6.5. Nitrogen reduction and other synthesis routes

Electrochemical nitrogen reduction is far less developed than Haber–Bosch. It could nevertheless suit decentralised production, as it operates near ambient conditions, avoids the high-pressure synthesis loop and could potentially operate more flexibly under intermittent power. Realising these advantages requires progress in cell performance, stability and verification, which are addressed below.

Performance and stability: Experiments should improve cell voltage, Faradaic efficiency and productive current density together rather than individually. They should also show whether these improvements hold at higher production rates and over long-term continuous and intermittent operation, with ammonia production verified by isotope-labelled experiments [3]. Once cell performance improves, a plant-level comparison with Haber–Bosch should include product recovery, electrolyte management and the equipment that NRR would replace, rather than the conversion block alone.

Research priorities: For the aqueous route, the priority is nitrogen selectivity over hydrogen evolution, followed by reduced hydrogen site blocking; gas-diffusion electrodes or higher pressure help only once activity approaches the transport limit. Experiments should also test whether the low voltage of a zero-gap cell holds as current density rises, since that decides the hybrid case. For the lithium-mediated routes, the plating potential cannot be engineered away, so the priority is a mediator that deposits at a less negative potential or a pathway without metal plating. A stable interphase and a water-tolerant mediator would then address the remaining losses and the upstream feed energy.

Alternative synthesis routes: Beyond electrochemical NRR, future research should investigate alternative synthesis technologies that could improve the flexibility and economics of small-scale ammonia production. Absorption-enhanced Haber–Bosch and improved low-pressure catalysts could reduce the operating requirements of the conventional synthesis loop. Chemical-looping ammonia synthesis offers another promising pathway by separating nitrogen activation from ammonia formation. Further research should focus on their energy efficiency, compatibility with intermittent renewable power and long-term material stability to assess their suitability for autonomous operation.

6.6. Concluding recommendation

The next step is to establish whether the modelled plant remains technically and economically viable under real operating conditions. Three priorities stand out. These are identifying a remote-demand use case and comparing local production with the delivered cost of conventional ammonia, validating small-scale Haber–Bosch and balance-of-plant costs, and using targeted subsystem tests and operating data to assess assumptions about operational flexibility, autonomy, water supply and equipment degradation. Together, these would provide a stronger basis for determining where decentralised autonomous ammonia production could be competitive.

In the longer term, alternative synthesis routes could further improve the feasibility of small-scale production. Electrochemical nitrogen reduction could suit decentralised production, but substantial progress in energy efficiency, production rate and long-term stability is needed before a reliable plant-level assessment can be made.

7

Use of AI

During the preparation of this thesis, the AI tools ChatGPT (OpenAI) and Claude (Anthropic) were used to support both the research and the writing process. They were used throughout the project for the following purposes:

- Literature research: searching for and identifying relevant scientific publications, summarising their content, and compiling literature values used as model inputs and for comparison with the results.
- Modelling and code: developing, structuring, debugging and optimising the Python code for the techno-economic plant model, the configuration optimisation, the uncertainty analysis and the reduced-order electrochemical NRR models.
- Analysis and interpretation: discussing and testing interpretations of the simulation results, and comparing technologies, plant configurations and locations.
- Writing: redrafting text, and improving the clarity, consistency and academic language of the thesis.
- Formatting: assisting with LaTeX formatting and with the preparation of tables and figures.

The research questions, methodology, model structure, assumptions, analyses and conclusions were developed independently by the author. AI-generated outputs were critically reviewed and verified before use. Literature values and references were checked against original sources, while code and model results were validated through calculations and energy and mass balance checks. All reported results were obtained directly from the models, and AI-supported text was reviewed to ensure accuracy. The author remains fully responsible for the content and conclusions of this thesis.

References

[1] AACE International. *Development of Factored Cost Estimates: As Applied in Engineering, Procurement, and Construction for the Process Industries*. Recommended Practice 59R-10. Morgantown, WV: AACE International, 2011. URL: https://web.aacei.org/docs/default-source/toc/toc_59r-10.pdf.

[2] Z. Abdin, C. J. Webb, and E. M. Gray. "Modelling and simulation of an alkaline electrolyser cell". In: *Energy* 138 (2017), pp. 316–331. DOI: 10.1016/j.energy.2017.07.053.

[3] S. Z. Andersen et al. "A Rigorous Electrochemical Ammonia Synthesis Protocol with Quantitative Isotope Measurements". In: *Nature* 570.7762 (2019), pp. 504–508. DOI: 10.1038/s41586-019-1260-x.

[4] M. Appl. *Ammonia: Principles and Industrial Practice*. Weinheim: Wiley-VCH, 1999. DOI: 10.1002/9783527613885.

[5] Argus Media. *Argus Ammonia: Issue 24-22*. Argus Media, May 30, 2024. URL: https://view.argusmedia.com/rs/584-BUW-606/images/FER-Sample-Report-Argus-Ammonia-2024-05-30.

[6] A. Arora et al. "Design Standardization of Unit Operations for Reducing the Capital Intensity and Cost of Small-Scale Chemical Processes". In: *AIChE Journal* 66.2 (2020), e16802. DOI: 10.1002/aic.16802. URL: https://doi.org/10.1002/aic.16802.

[7] R. Arunthavanathan et al. "Process Safety 4.0: Artificial Intelligence or Intelligence Augmentation for Safer Process Operation?" In: *AIChE Journal* 70.7 (2024), e18475. DOI: 10.1002/aic.18475.

[8] A. Badgett et al. *Updated Manufactured Cost Analysis for Proton Exchange Membrane Water Electrolyzers*. Tech. rep. NREL/TP-6A20-87625. National Renewable Energy Laboratory, 2024. DOI: 10.2172/2311140. URL: https://www.osti.gov/biblio/2311140.

[9] M. Baldea et al. "From Automated to Autonomous Process Operations". In: *Computers & Chemical Engineering* 196 (2025), p. 109064. DOI: 10.1016/j.compchemeng.2025.109064.

[10] J. R. Bartels and M. B. Pate. *A Feasibility Study of Implementing an Ammonia Economy*. Tech. rep. 07S-01. Iowa State University, Iowa Energy Center, 2008. URL: https://p2infohouse.org/ref/50/49540.pdf.

[11] A. Buttler and H. Spliethoff. "Current Status of Water Electrolysis for Energy Storage, Grid Balancing and Sector Coupling via Power-to-Gas and Power-to-Liquids: A Review". In: *Renewable and Sustainable Energy Reviews* 82 (2018), pp. 2440–2454. DOI: 10.1016/j.rser.2017.09.003.

[12] M. W. Chase Jr. *NIST-JANAF Thermochemical Tables, Fourth Edition*. Journal of Physical and Chemical Reference Data Monograph 9. American Chemical Society, American Institute of Physics for the National Institute of Standards, and Technology, 1998, pp. 1–1951.

[13] H. Chen et al. "Review of Low-Temperature Plasma Nitrogen Fixation Technology". In: *Waste Disposal & Sustainable Energy* 3 (2021), pp. 201–217. DOI: 10.1007/s42768-021-00074-x.

[14] C. Choi et al. "Understanding Potential-Dependent Competition between Electrocatalytic Dinitrogen and Proton Reduction Reactions". In: *Nature Communications* 12.1 (2021), p. 4353. DOI: 10.1038/s41467-021-24539-1.

[15] M. Corva et al. "Differential Tafel Analysis: A Quick and Robust Tool to Inspect and Benchmark Charge Transfer in Electrocatalysis". In: *ACS Catalysis* 12.21 (2022), pp. 13805–13812. DOI: 10.1021/acscatal.2c03581. URL: https://doi.org/10.1021/acscatal.2c03581.

[16] H.-L. Du et al. "Electroreduction of Nitrogen with Almost 100% Current-to-Ammonia Efficiency". In: *Nature* 609.7928 (2022), pp. 722–727. DOI: 10.1038/s41586-022-05108-y.

[17] B. Endrődi et al. "Challenges and Opportunities of the Dynamic Operation of PEM Water Electrolyzers". In: *Energies* 18.9 (2025), p. 2154. DOI: 10.3390/en18092154.

[18] J. W. Erisman et al. “How a century of ammonia synthesis changed the world”. In: *Nature Geoscience* 1 (2008), pp. 636–639. DOI: 10.1038/ngeo325.

[19] European Commission. *Commission Delegated Regulation (EU) 2023/1185 establishing a minimum threshold for greenhouse gas emissions savings of recycled carbon fuels and specifying a methodology for assessing greenhouse gas emissions savings from renewable liquid and gaseous transport fuels of non-biological origin and from recycled carbon fuels*. Official Journal of the European Union, L 157, https://eur-lex.europa.eu/eli/reg_del/2023/1185/oj. Sets the 70% savings threshold and the 94 gCO2eq/MJ fossil comparator. 2023.

[20] European Parliament and Council of the European Union. *Regulation (EU) 2023/956 establishing a carbon border adjustment mechanism*. Official Journal of the European Union, L 130, https://eur-lex.europa.eu/eli/reg/2023/956/oj. Definitive period from 1 January 2026; covered goods include ammonia and nitrogen fertilisers. 2023.

[21] B. Fabiano et al. “Safety Concerns for Ammonia as a Green Energy Vector and the Role of Spray Curtains for Its Accidental Release Mitigation”. In: *Energies* 18.13 (2025), p. 3412. DOI: 10.3390/en18133412.

[22] S. Fahr et al. “Dynamic Simulation of a Highly Load-flexible Haber–Bosch Plant”. In: *International Journal of Hydrogen Energy* 102 (2025), pp. 1231–1242. DOI: 10.1016/j.ijhydene.2025.01.039.

[23] R. T. Ferrell and D. M. Himmelblau. “Diffusion coefficients of nitrogen and oxygen in water”. In: *Journal of Chemical and Engineering Data* 12.1 (1967), pp. 111–115. DOI: 10.1021/je60032a036.

[24] G. Flis and G. Wakim. *Solid Oxide Electrolysis: A Technology Status Assessment*. Tech. rep. Clean Air Task Force, Nov. 2023. URL: https://cdn.catf.us/wp-content/uploads/2023/11/15092028/solid-oxide-electrolysis-report.pdf.

[25] X. Fu et al. “Continuous-flow electrosynthesis of ammonia by nitrogen reduction and hydrogen oxidation”. In: *Science* 379.6633 (2023), pp. 707–712. DOI: 10.1126/science.adf4403.

[26] T. Galimova et al. “Feasibility of Green Ammonia Trading via Pipelines and Shipping: Cases of Europe, North Africa, and South America”. In: *Journal of Cleaner Production* 427 (2023), p. 139212. DOI: 10.1016/j.jclepro.2023.139212.

[27] T. Gamer et al. “The Autonomous Industrial Plant: Future of Process Engineering, Operations and Maintenance”. In: *Journal of Process Control* 88 (2020), pp. 101–110. DOI: 10.1016/j.jprocont.2020.01.012.

[28] N. Gayoso et al. “Techno-Economic Analysis of Atmospheric Water Harvesting Across Climates”. In: *ACS ES&T Engineering* 4.7 (2024), pp. 1769–1780. DOI: 10.1021/acsestengg.4c00098.

[29] J. Groot et al. “A Techno-Economical Assessment for Decentralized Autonomous Green Methanol Production”. In: *Proceedings of the 2025 14th International Conference on Renewable Energy Research and Applications (ICRERA)*. IEEE, 2025, pp. 820–823. DOI: 10.1109/ICRERA66237.2025.11283763.

[30] M. T. de Groot, J. Kraakman, and R. L. Garcia Barros. “Optimal Operating Parameters for Advanced Alkaline Water Electrolysis”. In: *International Journal of Hydrogen Energy* 47.82 (2022), pp. 34773–34783. DOI: 10.1016/j.ijhydene.2022.08.075.

[31] C. Hank et al. *Site-specific, Comparative Analysis for Suitable Power-to-X Pathways and Products in Developing and Emerging Countries*. Study commissioned by the H2Global Foundation in cooperation with GIZ. Freiburg, Germany: Fraunhofer Institute for Solar Energy Systems ISE, 2023. URL: https://www.ise.fraunhofer.de/en/publications/studies/power-to-x-country-analyses.html.

[32] T. L. Hardenburger and M. Ennis. “Nitrogen”. In: *Kirk-Othmer Encyclopedia of Chemical Technology*. John Wiley & Sons, 2005, pp. 1–23. DOI: 10.1002/0471238961.1409201808011804.a01.pub2.

[33] A. Hauch et al. “Recent Advances in Solid Oxide Cell Technology for Electrolysis”. In: *Science* 370.6513 (2020), eaba6118. DOI: 10.1126/science.aba6118.

[34] D. Henkensmeier et al. “Separators and Membranes for Advanced Alkaline Water Electrolysis”. In: *Chemical Reviews* 124.10 (2024), pp. 6393–6443. DOI: 10.1021/acs.chemrev.3c00694.

[35] L. Hu et al. “Identification of Active Sites for Ammonia Electrosynthesis on Ruthenium”. In: *ACS Energy Letters* 7.12 (2022), pp. 4290–4298. DOI: 10.1021/acsenergylett.2c02175. URL: https://doi.org/10.1021/acsenergylett.2c02175.

[36] International Energy Agency. *Ammonia Technology Roadmap: Towards More Sustainable Nitrogen Fertiliser Production*. International Energy Agency, 2021. URL: https://www.iea.org/reports/ammonia-technology-roadmap.

[37] International Energy Agency. *Net Zero Roadmap: A Global Pathway to Keep the 1.5 °C Goal in Reach*. International Energy Agency, 2023. URL: https://www.iea.org/reports/net-zero-roadmap-a-global-pathway-to-keep-the-15-0c-goal-in-reach (visited on 06/10/2026).

[38] International Energy Agency. *Global Hydrogen Review 2024*. Paris: International Energy Agency, Oct. 2024. URL: https://www.iea.org/reports/global-hydrogen-review-2024 (visited on 07/27/2026).

[39] International Energy Agency. *Breakthrough Agenda Report 2025*. Paris: International Energy Agency, 2025. URL: https://www.iea.org/reports/breakthrough-agenda-report-2025.

[40] International Energy Agency. *H2Global – First auction for ammonia*. https://www.iea.org/policies/27846-h2global-first-auction-for-ammonia. Policies database, last updated 5 September 2025. 2025.

[41] International Renewable Energy Agency. *Renewable Power Generation Costs in 2025*. Tech. rep. Abu Dhabi: International Renewable Energy Agency (IRENA), 2026.

[42] International Renewable Energy Agency and Ammonia Energy Association. *Innovation Outlook: Renewable Ammonia*. Abu Dhabi: International Renewable Energy Agency, 2022. URL: https://www.irena.org/publications/2022/May/Innovation-Outlook-Renewable-Ammonia.

[43] B. Izelaar et al. “Techno-economic Assessment of Different Small-scale Electrochemical NH_3 Production Plants”. In: *Energy & Environmental Science* 17.21 (2024), pp. 7983–7998. DOI: 10.1039/D4EE03299C.

[44] B. Izelaar et al. “The Effect of Applied Potential on the Li-Mediated Nitrogen Reduction Reaction Performance”. In: *Nature Communications* 16 (2025), p. 10635. DOI: 10.1038/s41467-025-65627-w.

[45] J. Jäschke, Y. Cao, and V. Kariwala. “Self-Optimizing Control: A Survey”. In: *Annual Reviews in Control* 43 (2017), pp. 199–223. DOI: 10.1016/j.arcontrol.2017.03.001.

[46] Y. Kim et al. “Cathodic Protection System against a Reverse-Current after Shut-Down in Zero-Gap Alkaline Water Electrolysis”. In: *JACS Au* 2.11 (2022), pp. 2491–2500. DOI: 10.1021/jacsau.2c00314. URL: https://doi.org/10.1021/jacsau.2c00314.

[47] B. Kong, Q. Zhang, and P. Daoutidis. “Nonlinear Model Predictive Control of Flexible Ammonia Production”. In: *Control Engineering Practice* 148 (2024), p. 105946. DOI: 10.1016/j.conengprac.2024.105946.

[48] C. Kost et al. *Stromgestehungskosten Erneuerbare Energien*. Tech. rep. Freiburg: Fraunhofer-Institut für Solare Energiesysteme ISE, July 2024. URL: https://www.ise.fraunhofer.de/content/dam/ise/de/documents/publications/studies/DE2024_ISE_Studie_Stromgestehungskosten_Erneuerbare_Energien.pdf.

[49] N. Lazouski et al. “Understanding Continuous Lithium-Mediated Electrochemical Nitrogen Reduction”. In: *Joule* 3.4 (2019), pp. 1127–1139. DOI: 10.1016/j.joule.2019.02.003.

[50] N. Lazouski et al. “Non-aqueous gas diffusion electrodes for rapid ammonia synthesis from nitrogen and water-splitting-derived hydrogen”. In: *Nature Catalysis* 3 (2020), pp. 463–469. DOI: 10.1038/s41929-020-0455-8.

[51] L. Liao. *What Is the Current Average Cost of Energy Storage Systems in 2025*. Updated August 2026; accessed September 2026. BSLBATT, July 2025.

[52] B. Lin, T. Wiesner, and M. Malmali. “Performance of a Small-Scale Haber Process: A Techno-Economic Analysis”. In: *ACS Sustainable Chemistry & Engineering* 8.41 (2020), pp. 15517–15531. DOI: 10.1021/acssuschemeng.0c04313.

[53] P. J. Linstrom and W. G. Mallard, eds. *NIST Chemistry WebBook, NIST Standard Reference Database Number 69*. Gaithersburg, MD. DOI: 10.18434/T4D303. URL: https://webbook.nist.gov/chemistry/ (visited on 11/10/2026).

[54] S. Liu et al. “Abnormal Situation Management in Chemical Processes: Recent Research Progress and Future Prospects”. In: *Processes* 11.6 (2023), p. 1608. DOI: 10.3390/pr11061608.

[55] S. Maheshwari, G. Rostamikia, and M. J. Janik. “Elementary kinetics of nitrogen electroreduction on Fe surfaces”. In: *The Journal of Chemical Physics* 150.4 (2019), p. 041708. DOI: 10.1063/1.5048036.

[56] V. A. Martinez Lopez et al. “Dynamic operation of water electrolyzers: A review for applications in photovoltaic systems integration”. In: *Renewable and Sustainable Energy Reviews* 182 (2023), p. 113407. ISSN: 1364-0321. DOI: 10.1016/j.rser.2023.113407.

[57] G. Masson et al. *Trends in Photovoltaic Applications 2025*. IEA PVPS Report T1-48:2025. International Energy Agency Photovoltaic Power Systems Programme, 2025. URL: https://iea-pvps.org/wp-content/uploads/2025/10/IEA-PVPS_Trends_2025-.pdf (visited on 07/23/2026).

[58] J. H. Montoya et al. “The Challenge of Electrochemical Ammonia Synthesis: A New Perspective on the Role of Nitrogen Scaling Relations”. In: *ChemSusChem* 8.13 (2015), pp. 2180–2186. DOI: 10.1002/cssc.201500322.

[59] S. Mucci, A. Mitsos, and D. Bongartz. “Cost-Optimal Power-to-Methanol: Flexible Operation or Intermediate Storage?” In: *arXiv preprint* (2023). DOI: 10.48550/arXiv.2305.18338. arXiv: 2305.18338 [math.OC].

[60] R. Nayak-Luke, R. Bañares-Alcántara, and I. Wilkinson. ““Green” Ammonia: Impact of Renewable Energy Intermittency on Plant Sizing and Levelized Cost of Ammonia”. In: *Industrial & Engineering Chemistry Research* 57.43 (2018), pp. 14607–14616. DOI: 10.1021/acs.iecr.8b02447.

[61] R. M. Nayak-Luke and R. Bañares-Alcántara. “Techno-economic Viability of Islanded Green Ammonia as a Carbon-free Energy Vector and as a Substitute for Conventional Production”. In: *Energy & Environmental Science* 13.9 (2020), pp. 2957–2966. DOI: 10.1039/D0EE01707H.

[62] S. Nduva and C. Migwe. *Fertilizer Logistics in East Africa*. 2022. URL: https://ifdc.org/2022/08/05/fertilizer_logistics_in_east_africa/.

[63] C. O. Ofori-Bah and V. Amanor-Boadu. “Directing the Wind: Techno-Economic Feasibility of Green Ammonia for Farmers and Community Economic Viability”. In: *Frontiers in Environmental Science* 10 (2023), p. 1070212. DOI: 10.3389/fenvs.2022.1070212. URL: https://doi.org/10.3389/fenvs.2022.1070212.

[64] M. J. Palys, A. Allman, and P. Daoutidis. “Exploring the Benefits of Modular Renewable-Powered Ammonia Production: A Supply Chain Optimization Study”. In: *Industrial & Engineering Chemistry Research* 58.15 (2019), pp. 5898–5908. DOI: 10.1021/acs.iecr.8b04189.

[65] M. J. Palys et al. “Modeling and Optimal Design of Absorbent Enhanced Ammonia Synthesis”. In: *Processes* 6.7 (2018), p. 91. DOI: 10.3390/pr6070091.

[66] J. B. Rawlings, D. Q. Mayne, and M. M. Diehl. *Model Predictive Control: Theory, Computation, and Design*. 2nd ed. Madison, Wisconsin: Nob Hill Publishing, 2017.

[67] Z. Ren et al. “Experimental Studies and Modeling of a 250-kW Alkaline Water Electrolyzer for Hydrogen Production”. In: *Journal of Power Sources* 544 (2022), p. 231886. DOI: 10.1016/j.jpowsour.2022.231886. URL: https://doi.org/10.1016/j.jpowsour.2022.231886.

[68] J. W. Rosbo et al. “Optimisation and robust control of a load-flexible Haber–Bosch ammonia synthesis loop”. In: *Computers & Chemical Engineering* 210 (2026), p. 109614. DOI: 10.1016/j.compchemeng.2026.109614.

[69] K. Rouwenhorst. *Status of renewable ammonia projects and technology licensors*. Accessed: 2026-09-29. Nov. 2025. URL: https://ammoniaenergy.org/articles/status-of-renewable-ammonia-projects-and-technology-licensors/.

[70] K. H. R. Rouwenhorst and L. Lefferts. “Feasibility Study of Plasma-catalytic Ammonia Synthesis for Energy Storage Applications”. In: *Catalysts* 10.9 (2020), p. 999. DOI: 10.3390/catal10090999.

[71] M. F. Ruth, A. T. Mayyas, and M. K. Mann. *Manufacturing Competitiveness Analysis for PEM and Alkaline Water Electrolysis Systems*. Tech. rep. NREL/PR-6A20-70380. National Renewable Energy Laboratory, 2019. URL: https://www.osti.gov/biblio/1550788.

[72] S&P Global. *European Ammonia Import Price Reaches Three-Year High as Production Costs Soar*. Mar. 2026. URL: https://www.spglobal.com/energy/en/news-research/latest-news/agriculture/030626-european-ammonia-import-price-reaches-three-year-high-as-production-costs-soar.

[73] N. Salmon and R. Bañares-Alcántara. “Impact of grid connectivity on cost and location of green ammonia production: Australia as a case study”. In: *Energy & Environmental Science* 14.12 (2021), pp. 6655–6671. DOI: 10.1039/D1EE02582A.

[74] N. Salmon and R. Bañares-Alcántara. “Impact of Process Flexibility and Imperfect Forecasting on the Operation and Design of Haber–Bosch Green Ammonia”. In: *RSC Sustainability* 1 (2023), pp. 923–937. DOI: 10.1039/D3SU00067B.

[75] R. Sander. “Compilation of Henry’s law constants (version 4.0) for water as solvent”. In: *Atmospheric Chemistry and Physics* 15 (2015), pp. 4399–4981. DOI: 10.5194/acp-15-4399-2015.

[76] Science Education Resource Center at Carleton College. *Global Population Density Image, World Map*. Image credit: United Nations Environment Programme, Center for International Earth Science Information Network, Columbia University, and Centro Internacional de Agricultura Tropical. Accessed 15 June 2026. 2016. URL: https://serc.carleton.edu/details/images/131700.html.

[77] A. R. Singh et al. “Electrochemical Ammonia Synthesis—The Selectivity Challenge”. In: *ACS Catalysis* 7.1 (2017), pp. 706–709. DOI: 10.1021/acscatal.6b03035.

[78] E. Skúlason et al. “A theoretical evaluation of possible transition metal electro-catalysts for N2 reduction”. In: *Physical Chemistry Chemical Physics* 14.3 (2012), pp. 1235–1245. DOI: 10.1039/C1CP22271F.

[79] V. Smil. *Enriching the Earth: Fritz Haber, Carl Bosch, and the Transformation of World Food Production*. Cambridge, MA: MIT Press, 2001. ISBN: 978-0-262-19449-5.

[80] C. Smith, A. K. Hill, and L. Torrente-Murciano. “Current and future role of Haber–Bosch ammonia in a carbon-free energy landscape”. In: *Energy & Environmental Science* 13.2 (2020), pp. 331–344. DOI: 10.1039/C9EE02873K.

[81] Solar Energy Corporation of India. *National Green Hydrogen Mission: Green Ammonia Tender and Auction Results*. https://seci.co.in/nghm. Official auction results and SIGHT production incentives. 2025.

[82] Solargis. *Photovoltaic Electricity Potential: World Map*. Solar resource map © 2021 Solargis, licensed under CC BY-SA 4.0. Accessed 15 June 2026. 2021. URL: https://solargis.com/resources/free-maps-and-gis-data.

[83] M. van der Spek et al. “Uncertainty analysis in the techno-economic assessment of CO2 capture and storage technologies: Critical review and guidelines for use”. In: *International Journal of Greenhouse Gas Control* 100 (2020), p. 103113. DOI: 10.1016/j.ijggc.2020.103113.

[84] Stamicarbon. *Ammonia Technologies*. Stamicarbon. 2026. URL: https://www.stamicarbon.com/our-business/nx-stami-ammonia (visited on 07/27/2026).

[85] J. Szargut, D. R. Morris, and F. R. Steward. *Exergy Analysis of Thermal, Chemical, and Metallurgical Processes*. New York: Hemisphere, 1988.

[86] R. Tort et al. “Nonaqueous Li-Mediated Nitrogen Reduction: Taking Control of Potentials”. In: *ACS Energy Letters* 8.2 (2023), pp. 1003–1009. DOI: 10.1021/acsenergylett.2c02697.

[87] Transparency Market Research. *Ammonia Market Size, Share, Growth & Forecast 2035*. Accessed: 2026-05-26. 2025. URL: https://www.transparencymarketresearch.com/ammonia-market.html.

[88] E. Triantaphyllou. *Multi-Criteria Decision Making Methods: A Comparative Study*. Vol. 44. Applied Optimization. Boston, MA: Springer, 2000. DOI: 10.1007/978-1-4757-3157-6.

[89] Y. Tu et al. “Progress and Expectation of Atmospheric Water Harvesting”. In: *Joule* 2.8 (2018), pp. 1452–1475. DOI: 10.1016/j.joule.2018.07.015.

[90] A. Valera-Medina et al. “Ammonia for power”. In: *Progress in Energy and Combustion Science* 69 (2018), pp. 63–102. DOI: 10.1016/j.pecs.2018.07.001.

[91] K. Verleysen, A. Parente, and F. Contino. “How Sensitive Is a Dynamic Ammonia Synthesis Process? Global Sensitivity Analysis of a Dynamic Haber–Bosch Process for Flexible Seasonal Energy Storage”. In: *Energy* 232 (2021), p. 121016. DOI: 10.1016/j.energy.2021.121016.

[92] D. Vose. *Risk Analysis: A Quantitative Guide*. 3rd ed. John Wiley & Sons, 2008. ISBN: 9780470512845.

[93] N. Voutchkov. “Energy use for membrane seawater desalination – current status and trends”. In: *Desalination* 431 (2018), pp. 2–14. DOI: 10.1016/j.desal.2017.10.033.

[94] C. Wang et al. “Optimising renewable generation configurations of off-grid green ammonia production systems considering Haber–Bosch flexibility”. In: *Energy Conversion and Management* 280 (2023), p. 116790. DOI: 10.1016/j.enconman.2023.116790.

[95] O. Westhead et al. “The Origin of Overpotential in Lithium-Mediated Nitrogen Reduction”. In: *Faraday Discussions* 243 (2023), pp. 321–338. DOI: 10.1039/D2FD00156J.

[96] Yara International. *Annual Report 2025*. Yara International ASA, 2026. URL: https://www.yara.com/investor-relations/latest-annual-report/.

[97] B. Ye et al. “Continuous Ammonia Electrosynthesis from Nitrogen and Water in a Monolithic Pd Membrane-Based Flow Cell”. In: *ACS Energy Letters* 11.2 (2026), pp. 1907–1915. DOI: 10.1021/acsenergylett.5c03617.

A

Extended results

This appendix provides supporting tables and figures for the methodology and results presented in the main chapters.

A.1. Mass Balance

Table A.1: Design-point equations and inputs for the energy and exergy balance.

Subsystem	Calculation	Input parameters
Feedstock preparation and electrolysis		
Water harvesting	$P_{\mathrm{AWH}} = \dot{m}_{\mathrm{H_2O}} e_{\mathrm{AWH}}$	$e_{\mathrm{AWH}} = 0.25$ kWh/kg H_2O [28]
Alkaline electrolysis	$P_{\mathrm{el}} = 2F\dot{n}_{\mathrm{H_2}} U_{\mathrm{cell}}$ $P_{\mathrm{rev}} = \dot{n}_{\mathrm{H_2}} \Delta G^{\circ}$	$U_{\mathrm{cell}} = 2.05$ V $\Delta G^{\circ} = 237.13$ kJ/mol H_2 outlet: 30 bar
N_2 separation (PSA)	$P_{\mathrm{PSA}} = \dfrac{\dot{n}_{\mathrm{N_2}} e_{\mathrm{PSA}}}{v_m}$ $P_{\mathrm{rev}} = \dot{n}_{\mathrm{N_2}} R T_0 \ln\left(\dfrac{1}{y_{\mathrm{N_2}}}\right)$	$e_{\mathrm{PSA}} = 0.2$ kWh/Nm^3 [80] $v_m = 44.6$ mol/Nm^3 $y_{\mathrm{N_2}} = 0.7808$
PSA air feed	$\dot{m}_{\mathrm{air}} = \dfrac{\dot{m}_{\mathrm{N_2}}}{w_{\mathrm{N_2}} R_{\mathrm{PSA}}}$	$R_{\mathrm{PSA}} = 0.60$ N_2 purity: 99.99% N_2 outlet: 5 bar
Gas compression		
General compressor	$P_{\mathrm{comp}} = \dfrac{N\dot{n} c_p T_{\mathrm{in}}}{\eta_{\mathrm{is}}} \left(r^{\frac{\gamma-1}{\gamma}} - 1\right)$ $r = \left(\dfrac{P_{\mathrm{out}}}{P_{\mathrm{in}}}\right)^{1/N}$	N: compression stages $\eta_{\mathrm{is}} = 0.70$ Intercooling to 313 K Mixture c_p, γ: mole-fraction weighted
Nitrogen	General compressor equation	$N = 2$; 5→30 bar $c_p = 29.12$ J/(mol K) $\gamma = 1.40$
Synthesis gas	General compressor equation	$N = 3$; 30→300 bar H_2:N_2 = 3:1 $c_{p,\mathrm{H_2}} = 28.84$ J/(mol K) $\gamma_{\mathrm{H_2}} = 1.41$

Table A.1 continued

Subsystem	Calculation	Input parameters
Recycle gas	General compressor equation	$N = 1$; 0.85× fresh feed $\Delta P_{\mathrm{bed}} = 20$ bar $P_{\mathrm{in}} = P_{\mathrm{loop}} - \Delta P_{\mathrm{bed}}$
Haber–Bosch synthesis and heat recovery		
Reaction heat	$\dot{Q}_{\mathrm{R}} = -\Delta H_r^{\circ} \dot{n}_{\mathrm{N_2}}$	$\Delta H_r^{\circ} = -91.8$ kJ/mol N_2 Reactor: 723 K, 300 bar [4]
Feed preheating	$\dot{Q}_{\mathrm{pre}} = \dot{n}_{\mathrm{syn}} c_p (T_{\mathrm{R}} - T_{\mathrm{out}})$ $\dot{Q}_{\mathrm{pre}} \leq \dot{Q}_{\mathrm{R}}$	Preheating supplied by recovered reaction heat
Heat exergy	$\dot{E}x_Q = \dot{Q}\left(1 - \frac{T_0}{T}\right)$	Reference temperature $T_0 = 298.15$ K
Plant-level efficiency and exergy		
Energy efficiency	$\eta_{\mathrm{HHV}} = \frac{\dot{m}_{\mathrm{NH_3}} HHV}{\sum_k P_k}$	$HHV_{\mathrm{NH_3}} = 22.5$ MJ/kg [90]
Exergy efficiency	$\eta_{\mathrm{ex}} = \frac{\dot{E}x_{\mathrm{NH_3}}}{\sum_k P_k}$ $ex = ex_{\mathrm{ch}} + RT_0 \ln\left(\frac{P}{P_0}\right)$	Chemical exergy (kJ/mol): H_2: 236.09 NH_3: 337.9 O_2: 3.97

Notes: Reference conditions are $T_0 = 298.15$ K and $P_0 = 1$ bar. Reversible compression assumes $\eta_{\mathrm{is}} = 1$, while design compression uses $\eta_{\mathrm{is}} = 0.70$. Power calculations require consistent SI units, with conversion to kW where applicable. Thermochemical data are taken from NIST [53], and chemical exergies from Szargut et al. [85].

A.2. FESM benchmark

FESM sizes each plant to produce exactly 300 t/year, so the levelised cost is per contracted tonne. The following tables summarise the three sites.

A.2.1. Configuration

Table A.2: FESM plant configurations, capacity factors and annual production by site (2019).

Component	Geraldton	Neom	Lüderitz	Unit
PV peak capacity	1.15	1.29	1.22	MW
Wind capacity	0.25	0.09	0.16	MW
Battery storage	2.56	3.74	3.44	MWh
Electrolyser capacity	0.34	0.32	0.33	MW
Hydrogen buffer	48	20	25	kg H_2
Haber–Bosch loop	35.3	35.5	35.4	kg NH_3/h
Nitrogen unit	0.70	0.70	0.70	t N_2/d
Power transmission	0.35	0.34	0.34	MW
PV capacity factor	0.26	0.33	0.34	–
Wind capacity factor	0.53	0.68	0.64	–
Electrolyser capacity factor	0.917	0.948	0.934	–
Ammonia produced	300.0	300.0	300.0	tonne/yr
Hydrogen produced	53.4	53.4	53.4	tonne/yr
Capital cost	3.06	3.01	3.05	MUSD
Annualised cost	0.312	0.307	0.310	MUSD/yr

A.2.2. Energy balance

Table A.3: Annual energy balance for the FESM configurations by site.

Quantity	Geraldton	Neom	Lüderitz	Unit
Electricity generated	4207	4261	4531	MWh/yr
of which wind	1184	565	888	MWh/yr
Curtailed	1261	1258	1549	MWh/yr
Battery losses	72	128	108	MWh/yr
Transmission losses	86	86	86	MWh/yr
Electricity consumed	2788	2788	2788	MWh/yr
electrolyser	2697	2697	2697	MWh/yr
Haber–Bosch loop	37	37	37	MWh/yr
nitrogen unit	55	55	55	MWh/yr
Curtailed, share of generation	30.0	29.5	34.2	%
Not converted to ammonia	33.7	34.6	38.5	%
Electrolyser efficiency (LHV)	0.660	0.660	0.660	–
Overall efficiency (LHV)	0.372	0.368	0.346	–
Specific energy consumption	9.29	9.29	9.29	kWh/kg NH_3

A.2.3. Cost

Table A.4: FESM electricity and ammonia costs by site, including the effect of transmission.

Quantity	Geraldton	Neom	Lüderitz	Unit
Generation annualised cost	0.178	0.188	0.188	MUSD/yr
LCOE, per MWh generated	42.3	44.1	41.5	$/MWh
LCOE, per MWh consumed	63.9	67.3	67.5	$/MWh
LCOE incl. transmission, generated	49.0	50.4	47.6	$/MWh
LCOE incl. transmission, consumed	73.9	77.0	77.3	$/MWh
Generation share of LCOA	594	626	627	$/tonne
LCOA	1042	1022	1035	$/tonne

Table A.5: FESM levelised cost of ammonia by component and site.

Component	Geraldton	Neom	Lüderitz	Unit
Solar PV	184	207	196	$/tonne
Onshore wind	166	62	104	$/tonne
Battery storage	244	356	328	$/tonne
Transmission	93	90	91	$/tonne
Electrolyser	235	228	231	$/tonne
Hydrogen buffer	73	30	37	$/tonne
Haber–Bosch loop	40	41	41	$/tonne
Nitrogen unit	7	7	7	$/tonne
Total	1042	1022	1035	$/tonne

A.3. Configuration optimisation

This section supports Section 3.5. It opens with the cost parameters that define the objective, then reports the search itself, the resulting cost and operating statistics, and finally the same optimisation repeated at the two alternative sites.

A.3.1. Cost assumptions

Table A.6: Component cost assumptions in the plant model and FESM.

Component	FESM			This model				
	Capex	Opex [%/yr]	Annual charge	Capex	Opex [%/yr]	Life [yr]	Annual charge	Source
Solar PV [$/kW]	478	1.48	48.1	573	1.50	25	62.3	[41]
Onshore wind [$/kW]	1913	0.77	196.5	1445	2.00	25	164.3	[41]
Battery, LFP [$/kWh]	287	1.08	28.6	200	1.10	10	32.0	[51]
Alkaline electrolyser [$/kW]	1961	1.37	210	1000	1.37	13	140.2	[38]
Hydrogen buffer [$/kg H_2]	4268	1.25	452	2434	1.25	25	258.5	[59]
Haber–Bosch loop [k$/(t/d)]	125.5	2.03	14.3	262.8	2.03	25	30.0	[84]
Nitrogen unit [k$/(t/d)]	26.8	2.03	3.05	38.4	2.00	20	4.68	[52]
Ammonia tank [$/t capacity]	not modelled			1000	2.00	25	113.7	[63]
Power transmission [$/kW]	864	0.15	80.6	not modelled				

A.3.2. Search statistics

Table A.7: Optimisation search statistics for each site's source year, without ammonia storage.

Location	Scenario	Pass	Configurations	Evaluated	Best objective
Geraldton	A	Exact walk	316 008	22 577	936
Geraldton	B	Coarse	4096	4096	815
Geraldton	B	Fine	16 200	16 200	795
Neom	A	Exact walk	316 008	25 477	949
Neom	B	Coarse	4096	4096	706
Neom	B	Fine	11 250	11 250	682
Lüderitz	A	Exact walk	316 008	77 896	1109
Lüderitz	B	Coarse	4096	4096	777
Lüderitz	B	Fine	13 500	13 500	755

Scenario A: $LCOA_{25}$ over the contracted 300 t/yr; Scenario B: LCOA over all production ($/tonne). "Evaluated": designs simulated before the walk could stop; all others are provably more expensive.

A.3.3. Levelised and capital cost by component

Table A.8: Geraldton levelised cost per tonne produced and cost shares by component in the source year.

	Base case		Scenario A		Scenario B		Robust optimum	
Component	$/t	%	$/t	%	$/t	%	$/t	%
Solar PV	402	20.2	122	15.0	146	18.4	131	16.2
Onshore wind	0	0.0	286	35.1	257	32.3	256	31.7
Battery (LFP)	919	46.1	46	5.7	9	1.2	50	6.2
Alkaline electrolyser	168	8.4	224	27.5	236	29.6	219	27.0
Haber–Bosch loop	172	8.6	104	12.8	110	13.9	112	13.9
Hydrogen buffer	309	15.5	19	2.3	22	2.8	20	2.5
PSA nitrogen unit	22	1.1	13	1.6	14	1.8	14	1.8
Ammonia tank	0	0.0	0	0.0	0	0.0	6	0.8
Total	1993	100.0	815	100.0	795	100.0	809	100.0

Table A.9: Capital cost by component for each Geraldton design (M$).

Component	Base case	Scenario A	Scenario B	Robust optimum
Solar PV	1.5457	0.3864	2.3186	0.3864
Onshore wind	0.0000	0.8667	3.9002	0.7222
Battery (LFP)	2.4000	0.1000	0.1000	0.1000
Alkaline electrolyser	0.5000	0.5500	2.9000	0.5000
Haber–Bosch loop	0.6306	0.3153	1.6712	0.3153
Hydrogen buffer	1.2171	0.0609	0.3651	0.0609
PSA nitrogen unit	0.0759	0.0379	0.2011	0.0379
Ammonia tank	0.0000	0.0000	0.0000	0.0180
Total	6.3693	2.3173	11.4562	2.1408

A.3.4. Location results in detail

Table A.10: Comparison of the 15-year optima with ammonia storage by site. Capacity factors cover 2001–2025, and operating values are design-year means.

Quantity	Geraldton	Neom	Lüderitz	Unit
Wind capacity factor	0.53	0.61	0.63	–
Solar capacity factor	0.26	0.33	0.34	–
Wind seasonal amplitude	1.25	2.02	2.00	max/min month
Wind–solar correlation	-0.32	-0.09	$+0.05$	–
PV area	3000	2000	2500	m^2
Wind capacity	0.50	0.50	0.50	MW
Battery storage	0.5	0.8	0.5	MWh
Electrolyser capacity	0.50	0.50	0.50	MW
Hydrogen buffer	25	25	25	kg H_2
Haber–Bosch loop	50	50	50	kg NH_3/h
Ammonia tank	18	18	22	tonne
Capital cost	2.14	2.07	2.08	M$
Ammonia produced	310.6	308.1	315.1	tonne/yr
Curtailed	12.9	15.5	21.5	%
Design years met	14 of 15	14 of 15	14 of 15	–
Validation years met	8 of 10	7 of 10	10 of 10	–
$LCOA_{25}$, no tank	1129	1111	1199	$/tonne
$LCOA_{25}$, with tank	864	850	842	$/tonne
Value of the tank	264	262	357	$/tonne

Table A.11: Scenario A optima for each site's source year without ammonia storage.

Quantity	Geraldton	Neom	Lüderitz	Unit
Wind capacity factor	0.53	0.68	0.64	–
Solar capacity factor	0.26	0.33	0.34	–
PV area	3000	3000	3500	m^2
Wind capacity	0.60	0.60	0.70	MW
Battery storage	0.5	0.5	0.5	MWh
Electrolyser capacity	0.55	0.55	0.65	MW
Hydrogen buffer	25	25	50	kg H_2
Haber–Bosch loop	50	55	60	kg NH_3/h
Capital cost	2.32	2.35	2.76	M$
Ammonia produced	344.6	396.6	409.1	tonne/yr
Weakest month	25.0	25.3	25.0	tonne
Monthly spread	33	57	68	%
Wind share of generation	64.7	65.0	62.5	%
Curtailment	14.3	23.1	29.6	%
Cost of electricity	42.4	37.1	40.9	$/MWh
LCOA, all production	815	718	813	$/tonne
$LCOA_{25}$, contracted	936	949	1109	$/tonne

Table A.12: Scenario B optima by site. Wind capacity reaches the upper search limit at all three sites.

Quantity	Geraldton	Neom	Lüderitz	Unit
PV area	18 000	10 000	7500	m^2
PV peak capacity	4.05	2.25	1.69	MW
Wind capacity	2.70	2.70	2.70	MW
Battery storage	0.5	0.5	0.5	MWh
Electrolyser capacity	2.90	2.90	2.90	MW
Hydrogen buffer	150	75	75	kg H_2
Haber–Bosch loop	265	265	265	kg NH_3/h
Capital cost	11.46	10.24	9.92	M$
Ammonia produced	1726.1	1820.0	1597.0	tonne/yr
Weakest month	120.5	109.1	88.2	tonne
Monthly spread	40	76	104	%
Wind share of generation	57.9	71.5	75.0	%
Curtailment	14.8	13.8	14.5	%
Cost of electricity	38.4	30.9	32.8	$/MWh
LCOA, all production	795	682	755	$/tonne
$LCOA_{25}$, capped	4572	4135	4018	$/tonne

Table A.13: Component costs ($/tonne produced) for the single-year optima at Neom and Lüderitz.

Component	Neom		Lüderitz	
	Scenario A	Scenario B	Scenario A	Scenario B
Solar PV	106	77	120	66
Onshore wind	248	244	281	278
Battery (LFP)	40	9	39	10
Alkaline electrolyser	194	223	223	255
Haber–Bosch loop	100	105	105	119
Hydrogen buffer	16	11	32	12
PSA nitrogen generator	13	13	14	15
Total	718	682	813	755

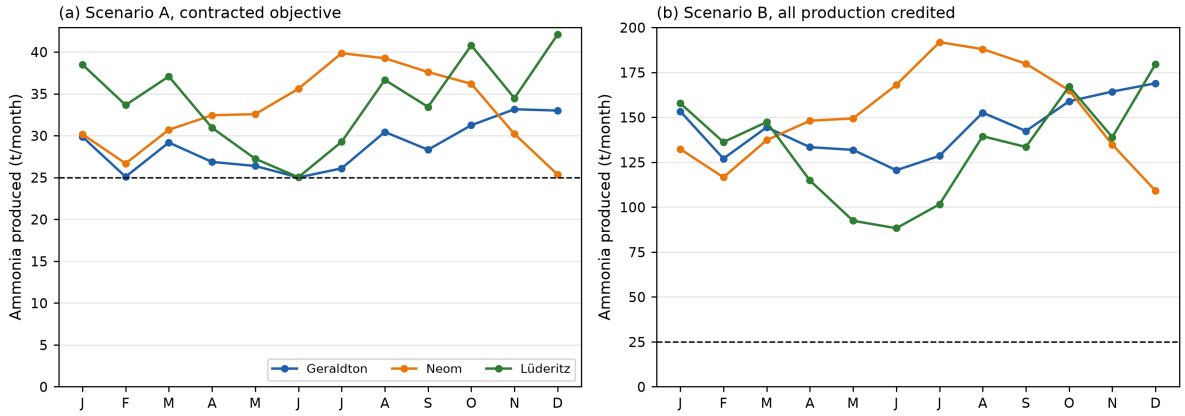

Figure A.1: Monthly ammonia output at each site's single-year optimum, against the 25 t contract floor. Note the different vertical scales: the Scenario B designs clear the floor by a factor of three or more, so only the Scenario A panel is constrained by it.

A.3.5. Weather-robust optimisation

Table A.14: Annual production and contract outcomes for two Geraldton designs across 25 weather years (D = design, V = validation).

	Scenario A, no tank			Robust optimum, 18 t tank		
Year	Produced t/yr	Weakest month, t	Outcome	Produced t/yr	Weakest month, t	Outcome
2001 D	343.8	19.45	miss	317.4	17.81	met
2002 D	334.4	23.91	miss	309.1	22.02	met
2003 D	336.1	23.12	miss	309.9	21.36	met
2004 D	336.3	23.35	miss	308.5	20.85	met
2005 D	331.8	21.10	miss	306.4	18.83	met
2006 D	339.2	22.52	miss	314.1	20.42	met
2007 D	345.3	24.27	miss	319.3	21.90	met
2008 D	339.5	22.54	miss	313.7	20.21	met
2009 D	344.4	25.48	met	319.2	23.33	met
2010 D	344.5	25.66	met	318.4	23.14	met
2011 D	330.4	24.54	miss	304.1	22.34	met
2012 D	336.4	21.41	miss	308.5	19.55	met
2013 D	320.1	20.17	miss	295.7	18.39	miss
2014 D	331.6	22.25	miss	304.0	20.13	met
2015 D	339.1	23.75	miss	310.6	21.45	met
2016 V	328.9	19.98	miss	305.4	18.45	miss
2017 V	344.4	22.79	miss	317.4	20.74	met
2018 V	345.9	20.59	miss	320.1	18.72	met
2019 V	343.6	22.95	miss	318.4	20.69	met
2020 V	320.9	18.18	miss	297.5	16.83	miss
2021 V	344.0	25.16	met	317.1	23.05	met
2022 V	345.5	22.48	miss	318.7	20.48	met
2023 V	333.0	22.62	miss	306.0	20.54	met
2024 V	339.6	22.53	miss	315.1	20.61	met
2025 V	350.0	23.31	miss	324.0	21.12	met
Design years, met		2 of 15			14 of 15	
Validation years, met		1 of 10			8 of 10	
All years, met		3 of 25			22 of 25	
Mean production		337.9 t			311.9 t	
Mean weakest month		22.57 t			20.52 t	
Worst annual shortfall		15.56 t			4.99 t	
Mean annual shortfall		4.04 t			0.41 t	

A.4. Final design

The tables below give the full figures behind the final design. Each is cited in Section 3.5, in the order of that section.

Table A.15: Energy flows and operating indicators for the final design in 2001.

Flow	MWh/yr	Share of generation, %	kWh/kg NH_3
Solar PV generation	1514	38.7	4.77
Wind generation	2398	61.3	7.56
Total generation	3912	100.0	12.33
Delivered to the plant	3389	86.6	10.68
Curtailed	495	12.6	1.56
Battery losses	28	0.7	0.09
Battery throughput	169	–	–
Haber–Bosch start-up, h/yr	180	–	–
Months below 25 t	4 of 12	–	–
Weakest month, tonne	17.8	–	–

Table A.16: Comparison of the base case, solar-only optimum and final design. Operating values are means for 2001–2015.

Quantity	Base case	Solar-only optimum	Final design	Unit
PV area	12 000	8500	3000	m^2
Wind capacity	0.00	0.00	0.50	MW
Battery storage	12.0	6.0	0.5	MWh
Electrolyser capacity	0.50	0.40	0.50	MW
Hydrogen buffer	500	25	25	kg H_2
Haber–Bosch loop	100	40	50	kg NH_3/h
Ammonia tank	0	16	18	tonne
Generation	6050	4286	3843	MWh/yr
Delivered to the plant	72.6	76.0	86.4	%
Battery losses	7.3	7.7	0.7	%
Curtailed	19.9	16.2	12.9	%
Generation per kg NH_3	14.62	14.01	12.37	kWh/kg
Battery throughput	2655	1987	169	MWh/yr
Haber–Bosch start-up time	228	496	181	h/yr
Ammonia produced	413.8	305.9	310.6	tonne/yr
Weakest month, mean	29.0	19.4	20.8	tonne
Design years met	15 of 15	14 of 15	14 of 15	–
Validation years met	10 of 10	10 of 10	8 of 10	–
Capital cost	6.37	3.05	2.14	M$
Battery share of cost	46.1	47.1	6.2	%
$LCOA_{25}$, contracted	2775	1359	864	$/tonne

Table A.17: Comparison of 15-year optima with and without ammonia storage. Operating values are design-year means.

Quantity	No tank	With tank	Change	Unit
PV area	4000	3000	-25%	m^2
Wind capacity	0.80	0.50	-38%	MW
Battery storage	0.5	0.5	0%	MWh
Electrolyser capacity	0.60	0.50	-17%	MW
Hydrogen buffer	25	25	0%	kg H_2
Haber–Bosch loop	55	50	-9%	kg NH_3/h
Ammonia tank	0	18	–	tonne
Capital cost	2.82	2.14	-24.1%	M$
$LCOA_{25}$, contracted	1129	864	-23.4%	$/tonne
Generation	5.75	3.84	-33.1%	GWh/yr
Curtailed	27.2	12.9	-14.3 pp	%
Ammonia produced	389.9	310.6	-20.3%	tonne/yr
Ammonia delivered	300.0	299.7	–	tonne/yr
Share of production delivered	76.9	96.5	$+19.6$ pp	%
Weakest month, mean	27.5	20.8	–	tonne
Design years meeting contract	14 of 15	14 of 15	–	–
Validation years meeting contract	8 of 10	8 of 10	–	–

Table A.18: Design-year mean electricity costs for the Geraldton base case and final design.

Quantity	Base case	Final design	Unit
Generation annualised cost	552.1	140.1	k$/yr
Electricity generated	6050	3843	MWh/yr
Electricity consumed	4393	3320	MWh/yr
Generation not delivered to plant	27.4	13.6	%
LCOE, per MWh generated	91.2	36.5	$/MWh
LCOE, per MWh consumed	125.7	42.2	$/MWh
Specific energy consumption	10.62	10.69	kWh/kg
Generation share of $LCOA_{25}$	1840	467	$/tonne

A.5. Sensitivity analysis

Each configuration above is a point design produced by a deterministic search on one cost basis, at one site, over one meteorological year. The three subsections below relax those choices in turn: the price list, the design variables themselves, and the weather.

A.5.1. Cost assumptions

Table A.19: Cost assumptions for the reference model, Wang 2030 and FESM. The Wang case varies capital costs only.

	This model	Wang 2030	FESM	Unit
Solar PV	573	525	478	$/kW
Onshore wind	1445	1220	1913	$/kW
Battery, LFP	200	100	287	$/kWh
Alkaline electrolyser	1000	320	1961	$/kW
Hydrogen buffer	2434	396	4268	$/kg H_2
Haber–Bosch loop	262.8	243.0	125.5	k$/(t/d)
Nitrogen unit	38.4	38.4	26.8	k$/(t/d)
Ammonia tank	1000	1000	1000	$/tonne
Operating cost	1.1–2.0	1.1–2.0	0.8–2.0	%/yr
Component life	10–25	10–25	25	yr
Discount rate	8	8	7	%

Table A.20: Costs of the four Geraldton designs under each price list at fixed capacities.

Design	Metric	This model	Wang 2030	FESM
Base case	Capex [M$]	6.37	3.63	8.21
	LCOA [$/t]	1993	1114	2625
	$LCOA_{25}$ [$/t]	2775	1551	3656
Scenario A	Capex [M$]	2.32	1.65	2.98
	LCOA [$/t]	815	561	1078
	$LCOA_{25}$ [$/t]	936	644	1238
Scenario B	Capex [M$]	11.46	8.20	14.51
	LCOA [$/t]	795	551	1039
	$LCOA_{25}$ [$/t]	4572	3169	5981
Robust	Capex [M$]	2.14	1.53	2.71
	LCOA [$/t]	809	560	1056
	$LCOA_{25}$ [$/t]	864	598	1127

Table A.21: Capacities and costs of the weather-robust optima under each price list.

Price list	PV [m^2]	Wind [MW]	Bat. [MWh]	Elec. [MW]	Buf. [kg]	HB [kg/h]	Tank [t]	Capex [M$]	$LCOA_{25}$ [$/t]
This model	3000	0.50	0.50	0.50	25	50	18	2.141	864
Wang 2030	2500	0.50	0.50	0.55	50	50	20	1.501	588
FESM	3000	0.50	0.50	0.50	25	50	18	2.706	1127

Table A.22: Cost by component after re-optimisation under each price list ($/contracted tonne).

Component	This model	Wang 2030	FESM
Solar PV	140	107	117
Onshore wind	274	231	363
Battery	53	27	77
Alkaline electrolyser	234	82	458
Haber–Bosch loop	120	111	57
Hydrogen buffer	22	7	38
Nitrogen unit	15	15	11
Ammonia tank	7	8	7
Total	864	588	1127

A.5.2. Monte Carlo input ranges

Table A.23: Input ranges for the probabilistic LCOA analysis. P10 and P90 are beta-PERT percentiles ($\lambda = 4$).

Input	Unit	Min	Mode	Max	P10	P90	Source
Capital cost, all cases							
Solar PV	$/kW	478	573	873	520	705	FESM; Fraunhofer ISE (2024), ground-mounted > 1 MW, EUR 700–900/kW
Onshore wind	$/kW	1041	1444	1845	1240	1648	IRENA (2024) global weighted average; Fraunhofer ISE (2024), EUR 1900/kW
Battery, LFP	$/kWh	125	200	405	159	292	Ember (2025), $75 equipment plus $50 installation; NREL 2-h system $427/kWh; Fraunhofer ISE (2024), EUR 400–600/kWh
Alkaline electrolyser	$/kW	600	1000	1440	795	1221	Chinese turnkey systems, $300–600/kW; 70% of European Hydrogen Observatory EUR 2075/kW
Haber–Bosch loop	k$/(t/d)	125.5	262.8	766.4	187.1	482.1	FESM; large-scale ISPT estimate (≈$141k/(t/d)); Palys et al. (2018), $2.3M at 2.4 t/d (2015 USD)
Hydrogen buffer	$/kg H_2	460	2434	3414	1514	2965	Nayak-Luke et al. (2021), above-ground pressure vessels $460–1400/kg; FESM
Nitrogen unit	k$/(t N_2/d)	32.6	38.4	77.8	35.4	54.6	FESM; vendor curve $2000/(Nm^3/h) at 100 Nm^3/h, exponent 0.59, scaled to ≈40 Nm^3/h
Ammonia tank	$/t	560	1000	2400	757	1619	Large refrigerated tanks, $561–1062/t; small pressurised tanks ≈$3/kg installed
Other inputs, all-inputs case only							
Discount rate	%	6	8	10	7.0	9.0	Assumed range
O&M multiplier	–	0.75	1.00	1.25	0.87	1.13	Assumed range, applied to all $f_{\mathrm{opex},i}$
Battery lifetime	yr	8	10	12	9.0	11.0	Assumed range
Electrolyser lifetime	yr	10	13	16	11.5	14.5	Assumed range

Table A.24: Contracted LCOA ($/tonne) from 10 000 draws per case. Det. pct. is the share at or below $864/tonne. The contract range is $750–900/tonne.

Case	P10	P50	P90	Mean	Delivered P50	Det. pct.	In range	Below
PERT, independent	818	906	1007	909	907	28%	46%	0.6%
Triangular, independent	847	950	1069	955	951	15%	27%	0.2%
PERT, $\rho = 0.5$	756	904	1078	912	906	38%	39%	9.1%
PERT, $\rho = 1$	709	901	1130	913	902	41%	33%	16.4%
PERT, all inputs	802	908	1025	911	912	31%	44%	2.4%

A.5.3. Design variables about the optimum

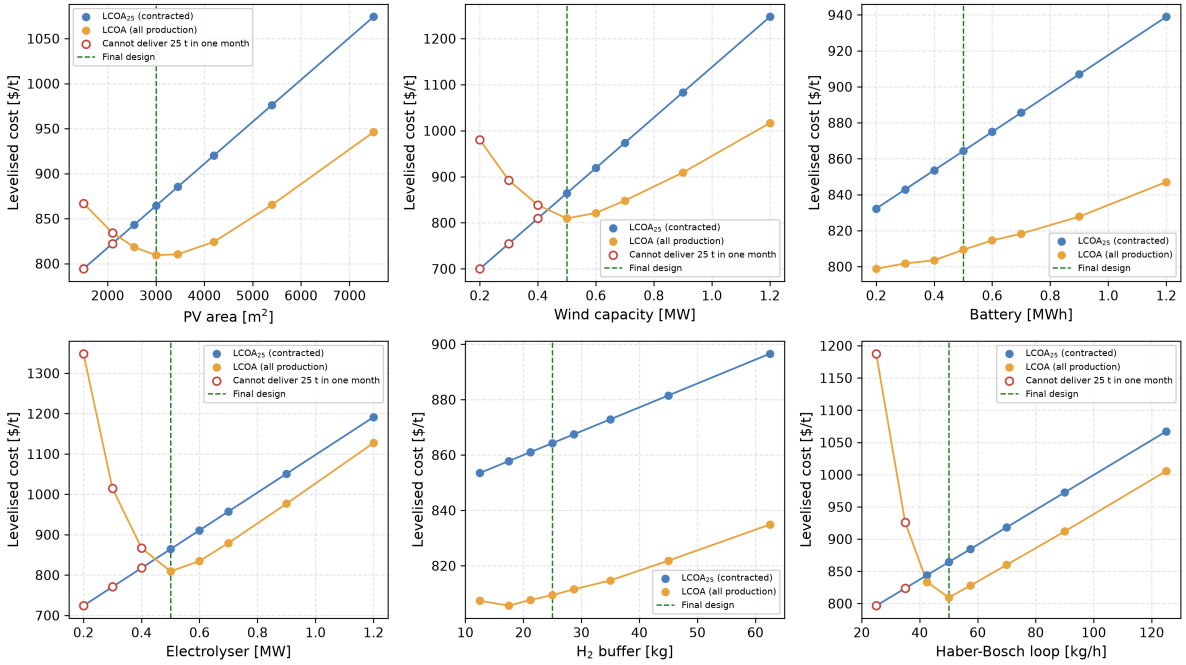

Figure A.2: One-at-a-time sensitivity about the weather-robust optimum at Geraldton on the source year only: each design variable is varied with the other five held fixed. Filled markers are feasible designs; open red markers fall below 25 t in at least one month. The dashed line marks the optimum. The same sweep tested against all fifteen design years is shown in Figure 3.20.

Table A.25: Ammonia output and costs when plant capacities and contracted output are scaled in proportion, assuming linear capital costs.

Scale factor	Ammonia [t/yr]	Annualised cost [$/yr]	LCOA [$/t]	$LCOA_{25}$ [$/t]
0.20	64.1	51 857	809	864
0.40	128.1	103 715	809	864
0.60	192.2	155 572	809	864
0.80	256.3	207 429	809	864
1.00	320.3	259 287	809	864
1.25	400.4	324 108	809	864
1.50	480.5	388 930	809	864
2.00	640.7	518 573	809	864
3.00	961.0	777 860	809	864
4.00	1281.4	1 037 146	809	864

A.6. Ammonia shipping cost

Galimova et al. [26] report ammonia shipping costs of $9.2\,\mathrm{EUR\,h/MW}$ to $12.7\,\mathrm{EUR\,h/MW}$ over $d_{\mathrm{ref}} \approx 13\,000$ km. Shipping cost is affine rather than proportional in distance, since terminal, storage, loading and port-time costs are distance-independent:

$$C(d) = C_{\mathrm{ref}} \left[\varphi + (1-\varphi) \frac{d}{d_{\mathrm{ref}}} \right], \qquad \varphi = \frac{a}{a + b\, d_{\mathrm{ref}}} \tag{A.1}$$

with φ the fixed cost share. Taking $\varphi = 0.5$ and $d/d_{\mathrm{ref}} = 8000/13\,000 = 0.615$:

$$C_{\mathrm{ship}} = 9.2\,\mathrm{EUR\,h/MW} \text{ to } 12.7\,\mathrm{EUR\,h/MW} \times 0.808 = 7.4\,\mathrm{EUR\,h/MW} \text{ to } 10.3\,\mathrm{EUR\,h/MW} \tag{A.2}$$

Using $\mathrm{LHV}_{\mathrm{NH_3}} = 5.17\,\mathrm{MW\,h/t}$ and $1.08\,\$/\mathrm{EUR}$:

$$C_{\mathrm{ship,NH_3}} = 7.4\,\mathrm{EUR\,h/MW} \text{ to } 10.3\,\mathrm{EUR\,h/MW} \times 5.17\,\mathrm{MW\,h/t} \times 1.08\,\$/\mathrm{EUR} = 41\,\$/\mathrm{t} \text{ to } 57\,\$/\mathrm{t} \tag{A.3}$$

Table A.26: Effect of the fixed cost share φ on ammonia shipping costs over 8000 km.

φ	Scaling factor	$\mathrm{EUR\,h/MW}$	\$/t NH_3
0.3 (proportional-leaning)	0.731	6.7–9.3	38–52
0.5 (baseline)	0.808	7.4–10.3	41–57
0.7 (terminal-dominated)	0.885	8.1–11.2	45–63
0 (naive linear scaling)	0.615	5.7–7.8	32–44

Cross-check: at d_{ref} the unscaled figure gives $51\,\$/\mathrm{t}$ to $71\,\$/\mathrm{t}$, consistent with the IEA ($50\,\$/\mathrm{t}$ to $70\,\$/\mathrm{t}$ for terminals plus shipping over $\sim 12\,000$ km) and with the $46\,\$/\mathrm{t}$ to $63\,\$/\mathrm{t}$ reported for the 13 500 km Patagonia–Netherlands route. Naive proportional scaling ($\varphi = 0$) falls below the IEA value for a *longer* route and is therefore rejected.

The same model gives the shipping cost from each site to its most likely market, South Korea for Geraldton and Rotterdam for Neom and Lüderitz (Table A.27).

Table A.27: Shipping and delivered ammonia costs to each site's likely market ($\varphi = 0.5$). The Neom estimate excludes Suez Canal fees.

Site	Market	Distance [km]	Factor [–]	Shipping [\$/t]	$LCOA_{25}$ [\$/t]	Delivered [\$/t]
Geraldton	South Korea	8000	0.808	41–57	864	913
Neom	Rotterdam	7000	0.769	40–55	850	897
Lüderitz	Rotterdam	11 000	0.923	47–65	842	898

B

Supporting visual material

This appendix collects figures that support the main text but are too large to sit within it.

B.1. Extended system balance

Hydrogen @ 30 bar (ex PEM)
P 30.00 bar
ΔH° 0.00 kJ/mol
ΔS° 102.40 J/mol·K
Exe 244.52 kJ/mol
Flow 3.00 mol/s
Total 733.56 kW
Compressor Nitrogen (5→30 bar)
Stages (intercooled) 2.00
Work* (isentropic) 5.07 kW
Work (η = 70%) 7.24 kW
Intercooler heat 7.24 kW
Nitrogen @ 30 bar
ΔH°f 0.00 kJ/mol
ΔS°f 163.33 J/mol·K
Exergy 9.04 kJ/mol
Flow 1.00 mol/s
Total stream exergy 9.04 kW
Syngas: $3H_2 + 1N_2$ @ 30 bar
Composition $3H_2 + 1N_2$
Total flow 4.00 mol/s
P 30.00 bar
T 298.15 K
Cp (weighted) 28.91 J/mol·K
γ (weighted) 1.41
Mass flow 34.06 g/s
Total stream exergy 742.61 kW
Step 2: Compression 30→300 bar (3 stages)
Pressure ratio per stage 2.15
T_out per stage (η=70%) 404.14 K
Intercool back to 313.15 K
Work* (isentropic) 25.74 kW
Work (η = 70%) 36.77 kW
Intercooler heat (2 stages) 21.04 kW
Exergy of intercooler heat 5.52 kW
Step 3: Feed preheat
T_in
T_out
P
Heat in / electricity in

Figure B.1: Extended system balance showing renewable generation, hydrogen production, nitrogen supply and synthesis-loop feed preparation.

C

Model pseudocode

This appendix describes step by step what the five Python models of this thesis do and in which order. Reporting and plotting steps are left out.

C.1. Base-case plant simulation --- Pseudo-code

```
PSEUDO-CODE: Hourly simulation of the autonomous ammonia plant

1. Input Data
   - Hourly capacity factors for one year (8760 h):
     base case    -> VORTEX source year of the site, solar only;
     optimisation -> solar and wind of one historical year (optimiser, step 1).
   - Hourly renewable power:
     P_gen = CF_solar * 1000 W/m2 * 0.225 * A_PV + CF_wind * P_wind
     (P_wind = 0 in the base case).

2. System Setup
   - Base case (fixed, solar only): 12,000 m2 PV, 12 MWh battery, 0.5 MW electrolyser,
     500 kg H2 buffer, 100 kg NH3/h HB loop; no wind and no NH3 tank.
   - Optimised designs: capacities from the optimiser, including wind;
     the NH3 tank is evaluated afterwards on the monthly production.
   - Specific energy per kg NH3: electrolyser + water harvesting 9.688 + 0.397 kWh,
     HB loop + PSA nitrogen unit 0.366 + 0.132 kWh.
   - Battery charge and discharge efficiency 0.92 each.
   - Start with an empty battery and H2 buffer; electrolyser and HB loop are OFF.

3. Simulation Loop
   - For each hour:
     a. HB loop (dispatch priority), with available power = renewables + battery:
        - OFF:       if power >= 30% of full load -> RAMP-UP.
        - RAMP-UP:   6 h at 30% load, no NH3; then PRODUCING if the buffer holds the
                     minimum feed (1 h at 30% of capacity), otherwise HOT STANDBY.
        - STANDBY:   15% load, no NH3; PRODUCING once the buffer holds the minimum feed.
        - PRODUCING: H2 feed = min(loop capacity, buffer content, power-limited feed);
                     NH3 = H2 feed * 34/6; if H2 feed < 30% of capacity -> STANDBY.
        - RAMP-DOWN: 3 h at 10% load -> OFF; back to RAMP-UP if power >= full load.
        - If STANDBY or RAMP-UP cannot be powered -> RAMP-DOWN.
     b. Supply the HB loop and PSA from renewables first, then from the battery;
        the loop only uses H2 that was in the buffer at the start of the hour.
     c. Electrolyser, with the remaining power (battery support up to its rating):
        - OFF:       if power >= 15% of rating -> RAMP-UP.
        - RAMP-UP:   4 h at 15% load, no H2 credited; then STANDBY
                     (RAMP-DOWN if power drops below 15% first).
        - STANDBY:   7% load; PRODUCING if power >= 15%, RAMP-DOWN if power < 7%.
        - PRODUCING: P_el = min(rating, available power, power that fits the buffer);
                     H2 = P_el / 10.085 kWh/kg * 6/34;
                     if power < 15% or buffer full -> STANDBY.
        - RAMP-DOWN: 3 h at 7% load -> OFF; back to RAMP-UP if power >= 7%.
        - Ramp progress is kept when the direction changes.
```

```
     d. Add the produced H2 to the buffer.
     e. Charge the battery with surplus power; curtail what does not fit.
     f. Record production, power flows, storage levels and operating states.

4. Results
   - Monthly NH3 = sum of hourly production.
   - Base case: feasible if every month >= 25 t.
     Optimised designs: the monthly NH3 is passed to the optimiser.
   - Battery losses from the charged and discharged energy.

5. Cost and LCOA
   - Per component: CAPEX = unit cost * capacity (water harvester: energy only, no CAPEX).
   - Annual cost = sum( CAPEX * (CRF + O&M fraction) ),  CRF = r(1+r)^n / ((1+r)^n - 1),
     with r = 8% and n = component lifetime.
   - LCOA (all production) = annual cost / NH3 produced.
   - Contracted LCOA25 = annual cost / 300 t (12 x 25 t); output above 300 t is not credited.
```

C.2. Robust configuration optimiser --- Pseudo-code

```
PSEUDO-CODE: Cheapest-first search for the least-cost reliable plant

1. Input Data (25 historical weather years)
   - Hourly data 2001-2025 per site; 29 February removed (8760 h per year).
   - Design years: 2001-2015 (15). Validation years: 2016-2025 (10), not used in the search.

2. Search Setup
   - Decision variables: PV area, wind, battery, electrolyser, H2 buffer, HB loop
     and NH3 tank (0, 2, 4, ..., 60 t).
   - Objective (contracted): LCOA25 = (annual plant cost + annual tank cost) / 300 t.
     The denominator is fixed, so the cost of a design is known without simulation.
   - Reliability criterion over the 15 design years, on the NH3 delivered from the tank:
     - 25 t delivered in every month in >= 90% of the years (at most 1 of 15 may miss),
     - mean shortfall over the failing tail (worst 10% of years, here the worst year)
       <= 2% of the annual contract (6 t).

3. Sort the Candidates
   - Build the grid of all capacity combinations.
   - Calculate the annual plant cost of every design with the cost model.
   - Sort the designs from cheapest to most expensive.

4. Cheapest-first Walk
   - For each design, starting with the cheapest:
     a. If its plant cost >= total cost of the best design so far: stop,
        because a tank never costs less than nothing.
     b. Keep only the tank sizes that could still make this design the cheapest.
     c. For each design year, starting with the weakest (lowest mean wind + solar CF):
        - Simulate the plant hour by hour (base-case model) -> monthly NH3 production.
        - For each tank size: run the tank model (step 5) and record the shortfall.
        - Drop a tank size once it misses the contract in more than one year.
        - If no tank size is left: reject the design and move to the next one.
     d. If a tank size meets the criterion: take the smallest one, and keep the design
        if plant + tank cost is lower than the best so far.

5. Ammonia Tank Model (one year)
   - Each month: deliver min(production, 25 t) from production, draw the rest from the
     tank and store surplus production up to the tank size; the excess is spilled.
   - Shortfall = 25 t - delivered from production - drawn from the tank.
   - Cyclic year: start at the highest level that the same year restores by December
     (closing level = opening level), so no stock is carried in from another year.

6. Search Sequence (contracted objective)
   - Coarse grid (4800 designs): one walk without a tank, then one with all tank sizes.
   - Refined grid around the coarse optimum: the same two walks, from that optimum.
   - Full grid (316,008 designs): one walk with all tank sizes, starting from the
     refined optimum as upper bound -> exact optimum of the full grid.
   - Check on the objective (all-production LCOA = annual cost / mean production of the
     design years): the denominator needs a simulation, so every design on the coarse
     and refined grids is simulated, with the same criterion and the smallest passing tank.
```

```
50
51 7. Validation
52    - Simulate the optimum in the 10 validation years with the same tank model.
53    - Count the years in which it meets the contract.
```

C.3. Aqueous NRR model --- Pseudo-code

```
1  PSEUDO-CODE: Reduced-order aqueous NRR cell model
2
3  1. Input Data
4     - Hu et al. (Ru/C catalyst, 0.1 M LiClO4): NH3 rate and FE at six cathode potentials
5       (+0.05 to -0.20 V vs RHE).
6     - Convert mass activity to area rate: rate = mass activity * Ru loading / electrode area.
7     - Assumed: b_HER = 0.120 V/dec, b_OER = 0.08 V/dec, j0_OER = 1e-7 A/cm2,
8       ASR = 0.5 ohm cm2 (engineered zero-gap cell), boundary layer 50 um.
9
10 2. Thermodynamics
11    - E0_NRR = -dG_rxn / 6F = +0.057 V vs RHE;  E0_HER = 0 V vs RHE.
12
13 3. Calibration
14    - E_ref = potential with the highest measured rate (-0.10 V).
15    - j_NRR,ref = 3F * rate_ref;  j_tot,ref = j_NRR,ref / FE_ref;
16      j_HER,ref = (1 - FE_ref) * j_tot,ref.
17    - N2 transport limit: j_lim = 6F * D_N2 * C_N2 / boundary-layer thickness.
18    - Fit b_NRR and the H-coverage term to the measured rates (least squares on log10 j),
19      with zero slope at E_ref; j_kin,ref is back-calculated so that E_ref is reproduced.
20
21 4. Potential Sweep
22    - For each cathode potential E from +0.05 to -0.30 V:
23      a. HER current:   j_HER = j_HER,ref * 10^((E_ref - E) / b_HER)
24      b. NRR current:   j_surf = j_kin,ref * 10^((E_ref - E) / b_NRR) * f_cov(E),
25                        f_cov = fraction of sites not blocked by hydrogen
26      c. N2 transport:  j_NRR = j_surf * j_lim / (j_surf + j_lim)
27      d. Selectivity:   FE = j_NRR / (j_NRR + j_HER)
28      e. Cell voltage:  V_cell = 1.229 + b_OER * log10(1 + j_tot/j0_OER) - E + j_tot * ASR
29      f. Energy:        SEC = 4.72 * V_cell / FE   [kWh/kg NH3]
30    - Potentials outside the measured window are flagged as extrapolation.
31
32 5. Output
33    - Operating point: highest FE within the measured window (+0.05 V), which is also
34      the lowest SEC; report FE, V_cell, j_NH3 = j_NRR and SEC.
```

C.4. Li-mediated NRR model --- Pseudo-code

```
1  PSEUDO-CODE: Reduced-order Li-mediated NRR cell model
2
3  1. Input Data
4     - Lazouski et al.: FE peak of 8.6% at 15 mA/cm2, exponent n = 1/2 (reaction orders),
5       measured range 0.3-25 mA/cm2.
6     - Westhead et al. (iR-corrected): Li plating onset -3.40 V vs RHE, -3.59 V at 2 mA/cm2.
7     - Anode: hydrogen oxidation (HOR), eta_a,ref = 0.50 V at 2 mA/cm2 (Westhead's HOR
8       estimate) and Tafel slope b_a = 0.120 V/dec (assumed).
9
10 2. Faradaic Efficiency Curve
11    - FE(j) = A * j^0.5 / (1 + B * j^1.5)   (Lazouski's Eq. 12, j in mA/cm2)
12    - A and B follow from the peak: FE = 8.6% and dFE/dj = 0 at 15 mA/cm2.
13    - No extrapolation outside the measured range.
14
15 3. Voltage Parameters
16    - Cathode at the plating potential: E_c = E_plate = -3.40 V vs RHE.
17    - Lumped resistance: ASR_eff = (-3.40 - (-3.59)) V / 2 mA/cm2 = 95 ohm cm2.
18
19 4. Current-density Sweep
20    - For each applied current density j in the measured range:
21      a. Selectivity:   FE from the curve of step 2
22      b. Anode:         eta_a = 0.40 + 0.120 * log10(j / 2 mA/cm2)
```

```
     c. Cell voltage:  V_cell = eta_a - E_plate + j * ASR_eff
     d. NH3 current:   j_NH3 = FE * j
     e. Energy:        SEC = 4.72 * V_cell / FE   [kWh/kg NH3]
   - SEC covers the cell only: the energy to supply the proton donor
     (ethanol or H2) is not included.

5. Output
   - Operating point with the lowest SEC (9.44 mA/cm2).
```

C.5. Water-fed membrane NRR model --- Pseudo-code

```
PSEUDO-CODE: Reduced-order water-fed membrane Li-mediated NRR model

1. Input Data
   - Ye et al., one measured point at 6 mA/cm2, pulsed (1 min on / 1 min off):
     FE = 48% (NRR stage), charge 162 C (NRR) and 54 C (prehydridation),
     plating 3.8 V and anode 1.8 V (vs LFP), membrane 0.5 V, iR drop 1.0 V (~7 V total).

2. Calibration
   - Convert both electrode potentials from the LFP reference to RHE (offset 0.41 V):
     plating 3.39 V, anode 2.21 V; V_cell is unchanged.
   - Two Faradaic efficiencies:
     FE_op    = 48% (NRR stage only)            -> NH3 production rate
     FE_cycle = 48% * 162 / (162 + 54) = 36%    -> energy (SEC)
   - Resistances: ASR = measured loss / 6 mA/cm2 (membrane 83, cell 167 ohm cm2).
   - Anode: OER relation of the aqueous model (j0 = 1e-7 A/cm2), with the Tafel slope
     fitted so that E_anode = 2.21 V at 6 mA/cm2.

3. Current-density Sweep
   - For each current density j from 1 to 15 mA/cm2:
     a. Cell voltage:  V_cell = 3.39 + ASR_mem * j + E_anode(j) + ASR_cell * j
     b. NH3 current:   j_NH3 = FE_op * j during a pulse; 0.5 * FE_op * j on average
     c. Energy:        SEC = 4.72 * V_cell / FE_cycle   [kWh/kg NH3]
   - FE is kept constant (no current sweep reported); FE_op is varied from 43 to 53%.

4. Output
   - Operating point at the measured 6 mA/cm2.
```